2014

A search for a heavy resonance decaying to a top quark and a bottom quark with the CMS experiment

BOSTON UNIVERSITY

GRADUATE SCHOOL OF ARTS AND SCIENCES

Dissertation

A SEARCH FOR A HEAVY RESONANCE DECAYING TO A TOP QUARK AND BOTTOM QUARK WITH THE CMS EXPERIMENT

by

DAVID M. SPERKA

B.S., University of Wisconsin-Madison, 2009

Submitted in partial fulfillment of the

requirements for the degree of

Doctor of Philosophy

2014

Approved by

First Reader ____

Tulika Bose, Ph.D.
Assistant Professor of Physics

Second Reader ____

John Butler, Ph.D.
Professor of Physics

For Andrea, my sister.

Acknowledgments

There are several people I would like to thank without whom this thesis would not have been possible. First I would like to thank my advisor Tulika Bose for providing me with the vision needed to have a successful career as a graduate student. I would also like to thank the rest of my dissertation committee: Jim Rohlf, Ken Lane, Shyam Erramilli, and especially John Butler for his careful reading and input on this thesis. Also many thanks to all the professors at Boston University who have taught me physics. I would also like to thank my undergraduate advisor, Matt Herndon, who first gave me the opportunity to do research in particle physics. Also many thanks to my colleagues at Boston University on the CMS experiment who always were willing to give me advice: Larry Sulak, Edgar Carrera, and Aram Avetisyan and Cory Fantasia in particular.

I would also like to thank all my collaborators on the CMS experiment for ensuring successful data taking which allowed for the completion of this thesis, in particular those who I worked with on the High Level Trigger and especially those who helped mentor me including Wesley Smith, Roberto Carlin, Andrea Bocci, and Bryan Dahmes. I would also like to to thank those who helped guide me with my physics analysis, especially Meenakshi Narain, Sal Rappoccio, and Freya Blekman.

Also my thanks goes to all the other students at Boston University who shared in the ups and downs of life as a graduate student. I would also like to thank Zeynep for all of her love and support over the last year and especially during the writing of this thesis. Finally, I would like to thank my parents for making me the person I am today and for all of their support in letting me follow my dreams, even when they led me far away.

A SEARCH FOR A HEAVY RESONANCE DECAYING TO A TOP QUARK AND A BOTTOM QUARK WITH THE CMS EXPERIMENT

(Order No.)

DAVID M. SPERKA

Boston University Graduate School of Arts and Sciences, 2014

Major Professor: Tulika Bose, Assistant Professor of Physics

ABSTRACT

The standard model of particle physics can explain most measurements of elementary particle properties and interactions performed to date. However, it does not naturally explain the relatively light Higgs boson mass or the existence of small neutrino masses, and has no explanation for the dark matter observed in the universe. Many extensions to the standard model have been proposed to attempt to address these questions, and several predict the existence of heavy charged gauge bosons, usually referred to as W′ bosons. The Large Hadron Collider at CERN is the largest and most powerful particle accelerator in the world and offers the opportunity to search for W′ bosons using the CMS experiment, a large multi-purpose particle detector.

Results are presented from a search for a W′ boson produced in proton-proton collisions at a center of mass energy $\sqrt{s} = 8$ TeV and decaying into a top and a bottom quark, using a dataset collected by the CMS experiment corresponding to an integrated luminosity of 19.5 fb^{-1}. Various models of W′ boson production are studied by allowing for an arbitrary combination of left- and right-handed fermionic couplings. The analysis is based on the detection of events with an electron or muon, jets and missing transverse energy in the final state. No evidence for W′ boson production is found and 95% confidence level upper limits are obtained on the production cross section for several mass hypotheses and compared to theoretical predictions. For W′ bosons with purely right-handed couplings, and for those

with left-handed couplings when ignoring interference effects, the observed 95% confidence level limit on the W$'$ boson mass is M(W$'$) $>$ 2.05 TeV. These are the most stringent limits obtained to date in this channel.

Contents

List of Tables

List of Figures

Chapter 1

Introduction

Particle physics is the study of the properties and interactions of matter at the smallest possible scale. It can be said that particle physics began in the fifth century B.C. with the invention of atomism by the Greek philosophers Leucippus and Democritus [1]. The atomists argued that if it were possible to continuously divide matter into smaller pieces without end, then it would be possible to reduce it to nothing. Therefore, according to the atomists, there must exist an indivisible unit of matter which they called an atom. To explain the seemingly infinite forms of matter such as water, rock, and sand, the atomists believed that there were an infinite variety of atoms with varying shapes and sizes. While this theory is in many ways at odds with our current understanding of the atom, it nevertheless was revolutionary in posing the questions of what makes up the matter in universe, and what accounts for its incredible variety. A critical drawback to the atomic theory of the ancient Greeks was that it was purely philosophy, and was not (or could not) be tested at the time by scientific experiments. The atomic theory of nature developed slowly over the next two millenia, with varying theories of atoms being proposed by philosophers from all of the world's historical cultures. The pursuit of this most basic endeavor has since left the realm of philosophy and is subject to the rigors of the scientific method. The discoveries brought about by this pursuit have had a profound impact on human history and the search for a complete understanding continues to this day.

1.1 A Brief History of Modern Particle Physics

The modern era of particle physics began in the 19th century. In 1815, the English chemist William Prout noticed that the atomic masses of many chemical elements were multiples of the mass of hydrogen, the lightest known element. Prout therefore hypothesized that all matter was built up from hydrogen [2], thereby offering hydrogen as the atom hypothesized by the ancient Greeks. Upon further study of other elements, the relationship was found to be only approximate for other elements, but the idea still in a general sense is true. It also leads to the notion of subatomic particles being any unit of matter which is smaller than the hydrogen atom.

The first subatomic particle was discovered through a series of experiments on cathode rays in the latter half of the 19th century. These experiments culminated in 1897 when the English physicist J.J. Thomson, who knew of the hypothesis of Prout, measured the charge to mass ratio of cathode rays [3]. The experiments showed that the particles in the ray had a mass 1,000 times less than the mass of the hydrogen atom. The particles later became known as electrons, and to the present day the electron is still regarded as a "fundamental" particle with no further substructure.

Another important discovery that would play a key role in the development of particle physics was made around the same time as the experiments by Thomson. The French scientist Henri Becquerel suspected that the glow created in cathode ray tubes could explain the phenomena of phosphorescence, where certain substances continue to glow in the dark after being exposed to light. Becquerel began test his hypothesis using phosphorescent uranium salts, but soon realized that these crystals emit a form of radiation even when not exposed to light. Becquerel had discovered radioactivity [4]. Various types of radiation were identified, including α radiation (later found to be part of a helium atom) and β radiation (later found to be the electron).

The next fundamental particle to have been "discovered" was the photon. Although the wave properties of light had been known for hundreds of years, the German physicist Max

Planck proposed heuristically in 1900 that if electromagnetic radiation were only emitted in quantized units it could explain the energy spectrum of black body radiation [5]. Albert Einstein was the first to formally propose the existence of light particles in 1905 in order to explain the photoelectric effect [6].

In the first decade of the 20th century, many competing theories of the atom were put forth. The most popular was due to Thomson himself who supposed the atom consisted of electrons floating in a sea of positive charge, the so-called “plum-pudding” model of the atom. This model was eventually disproved in 1909 by experiments carried out by Ernest Rutherford and his students Hans Geiger and Ernest Marsden [7]. The experiment consisted of directing a beam of α particles from a radioactive element at a thin foil of gold. The surprising result of observing the α particles scattered backwards led Rutherford to develop a new model of the atom [8].

In the Rutherford model, the atom consists of a central “nucleus” with a positive charge, whose size is much smaller than the size of the atom. The nucleus is then orbited by the electrons, similar to planets rotating around the sun. The Rutherford model was given further credence when it was modified by Niels Bohr, who interpreted it in a quantum framework to explain the absorption spectrum of hydrogen and helium [9]. The nucleus of the hydrogen, being the lightest element, was given a special name: the proton.

While the quantum theory of nature was being developed further, it was predicted in 1931 by Paul Dirac that electrons can have either positive or negative charge [10]. This hypothesis was confirmed in cloud chamber experiments which were studying the properties of radiation produced in the atmosphere, known as cosmic rays. In 1932, Carl Anderson identified a particle with the same charge to mass ratio as the electron, but with opposite charge [11]. This was the first discovery of anti-matter. Around this time, Wolfgang Pauli postulated the existence of a new kind of neutral particle to prevent violation of energy conservation in radioactive decays. Enrico Fermi then developed a full theory of radioactivity [12] in 1934 including this new particle and named it the neutrino. It took over 20 years for its existence to be confirmed by direct observation.

Another important discover was made by Anderson in his cosmic ray experiments. In 1936, Anderson discovered a particle produced in the atmosphere with a mass greater than the mass of the electron but less than the mass of the proton [13]. The discovery was so unexpected that the physicist I. I. Rabi famously asked "Who ordered that?". At first it was thought that this particle might be responsible for mediating the nuclear forces, but it was eventually shown ten years later that this particle did not interact very strongly with the nucleus [14]. It was realized that this particle was a heavier copy of the electron, and it was named the muon. The electron and muon together were categorized into a group of particles called the "leptons". A photograph of a cloud chamber event which led to the discovery of the muon can be seen in Fig. 1.1.

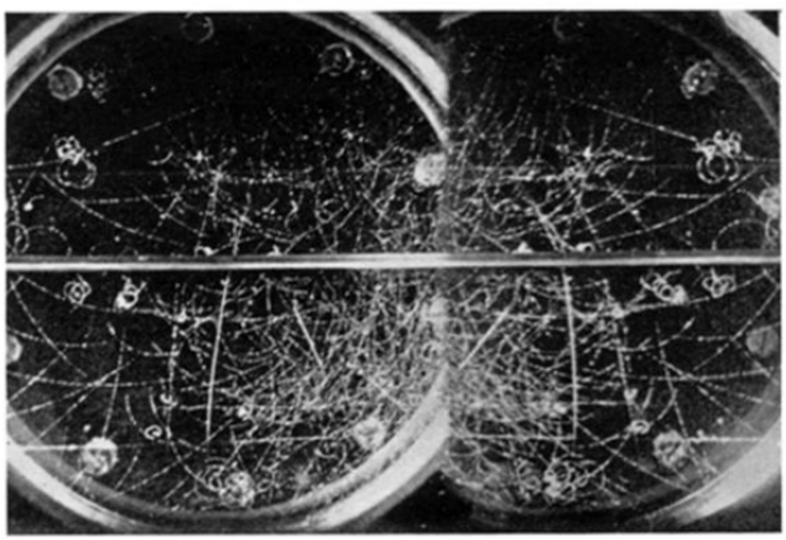

Figure 1.1: A photograph of a cloud chamber event which led to the discovery of the muon. From Ref. [13].

The second world war signaled a temporary halt to the progress in particle physics between 1939 and 1945. When the war was finished, the rapid pace picked up right where it left off. Continuing in the same vein as before the war, a group led by Cecil Powell studied cosmic radiation and identified in 1947 a new particle and measured its mass to be about 240 times the mass of the electron [15]. The particle was called the π meson, or pion, where the term meson referred to particles with masses between those of the electron and proton. Powell showed this particle was unstable and decayed to the previously discovered muon. Additional cosmic radiation experiments in the same year identified the existence of another type of meson, called the K meson [16]. In 1950, another new type of particle was discovered in cosmic ray experiments called the Λ baryon [17]. The Λ was different from the mesons because it could decay to a proton, whereas the mesons were only seen to decay to muons or other mesons. The war effort also led to the development of nuclear reactors, which finally allowed for the direct detection of neutrinos in 1956 [18].

Around the same time as the the cosmic ray experiments were being performed, experiments using beams of particles accelerated by magnets and directed onto targets were reaching energies high enough to produce baryons and mesons in a laboratory setting. The Cosmotron at Brookhaven National Laboratory (BNL) began operating in 1953 and accelerated protons to 3.3×10^9 electron volts (3.3 GeV).[1] and the Berkeley Bevatron began operating in 1954 and was capable of producing a 6.2 GeV proton beam. These laboratory experiments produced the mesons and baryons previously observed in cosmic ray experiments as well as many others [19].

The seemingly endless proliferation of new particles was finally systematized by Murray Gell-Mann in 1962 when he first introduced the quark model to explain the pattern of baryons and mesons [20]. Gell-Mann used symmetry arguments to explain the relationship between the observed mesons and baryons and also predicted a new one, the Ω^- which was discovered at the Brookhaven Alternating Gradient Synchrotron (AGS), a 33 GeV proton accelerator, in 1964 [21]. A photograph showing the discovery of the Ω^- can be seen in Fig. 1.2. Gell-Mann proposed that there were three entities called the “up” quark, the “down” quark, and the “strange” quark. He suggested these quarks were combined into triplets build the baryons (including the proton) and into doublets to create the mesons. The idea was further confirmed when experiments at Stanford Linear Accelerator Center (SLAC) provided evidence of the existence of internal structure of the baryons and mesons

[1] Throughout this thesis, natural units where $\hbar = c = 1$ are used unless otherwise specified.

by using a 20 GeV electron beam directed at fixed target [22]. The versatility of the AGS was further displayed by its ability to find evidence for a second type of neutrino, related to the muon, in 1962 [23].

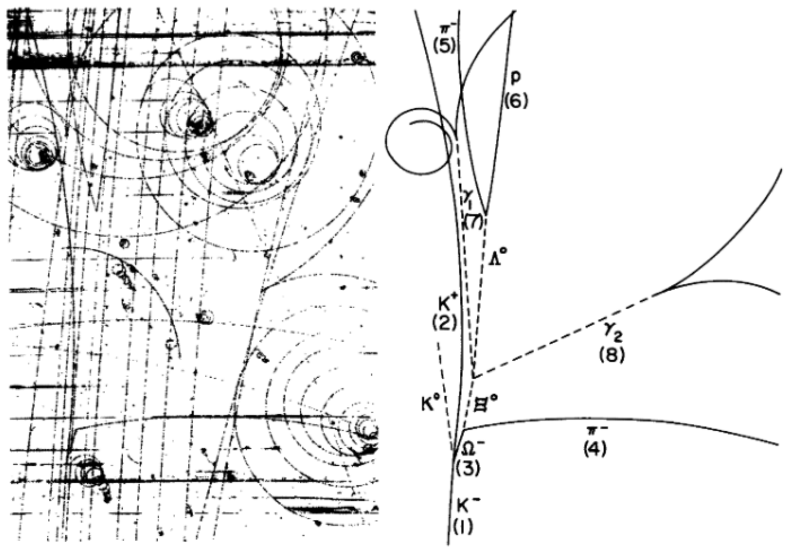

Figure 1.2: A photograph showing the first observation of the Ω^- baryon. From Ref. [21].

The next major development in particle physics, known as the "November Revolution", occurred in 1974. Two independent experiments, led by Burton Richter at SLAC and Samuel Ting at BNL, observed a new type of meson decaying much heavier than any previously known [24, 25]. This meson, known as the J/Ψ, was interpreted as evidence for the existence of a fourth quark, "charm", which had been suggested to exist a few years earlier [26]. A third type of lepton was discovered in 1975, also at SLAC, and named the τ lepton [27]. The discovery of the τ lepton also required for consistency the existence of a third type of neutrino, which was eventually confirmed much later [28]. A meson even heavier than the J/Ψ was discovered just a few years later in 1977 at the Fermi National Accelerator Laboratory (FNAL) [29]. This meson, known as the Υ, was interpreted as evidence for a fifth type of quark dubbed the "bottom". The measurements showing the discovery of the J/Ψ at BNL and the Υ are shown in Fig 1.3.

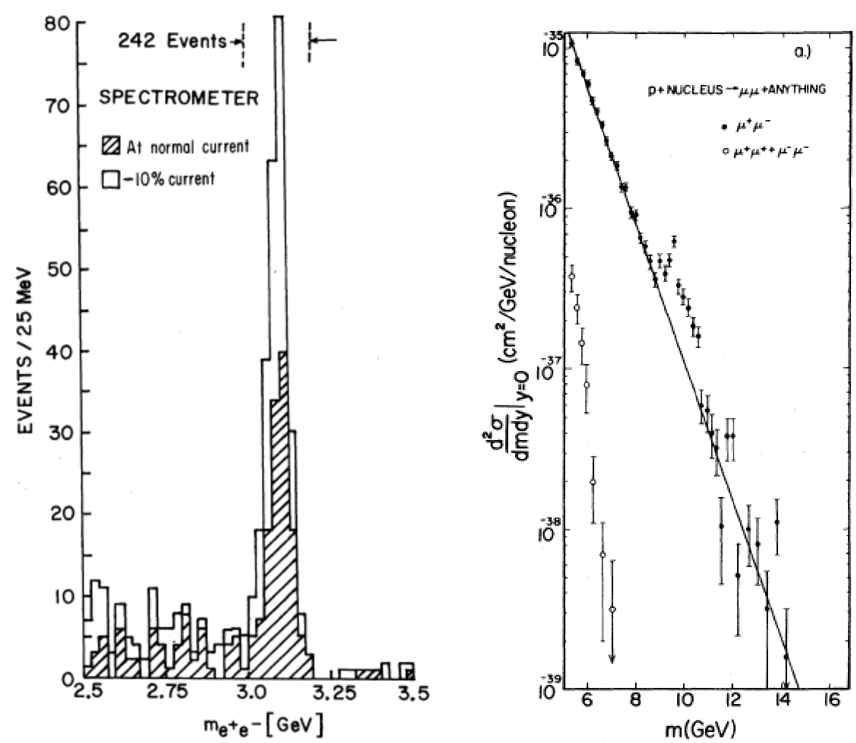

Figure 1.3: Data demonstrating the discovery of the J/Ψ at BNL (left, from Ref. [24]) and the Υ at FNAL (right, from Ref. [29]).

By the late 1970's, the theory which described the known particles and their interactions was well advanced. The theory predicted that there should be force carrying particles referred to as bosons, like the photon of electromagnetism, that carry the nuclear force. It was understood that there were two different nuclear forces: the "strong" nuclear force which holds the quarks together in the proton, and the "weak" nuclear force which is responsible for radioactive decay. Many properties of these forces were also known from their effects on the production and decay of the various mesons and baryons. The gluon, which carries the strong force, was indirectly observed at the Deutsches Elektronen-Synchrotron (DESY) in 1979 as decay products of the newly discovered Υ [30]. The W and Z bosons which carry the the weak force were discovered in 1983 at European Organization for Nuclear Research (CERN) in 540 GeV proton-antiproton collisions [31, 32]. A figure showing the measurement which led to the discovery of the Z boson can be seen in Fig. 1.4.

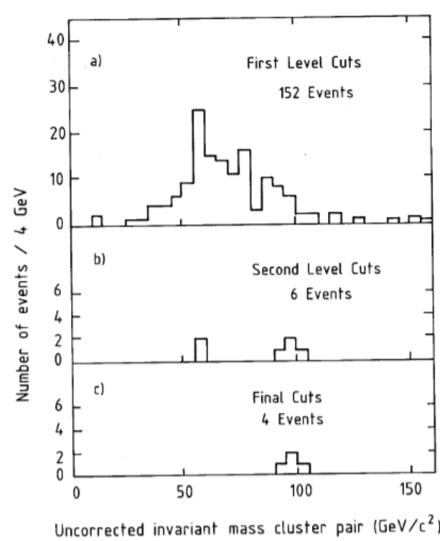

Figure 1.4: The measurement showing the discovery of the Z particle at CERN. From Ref. [32].

It was predicted even before the experimental discovery of the bottom quark that the bottom quark should come along with a partner, making for a total of 6 quarks. It was also predicted by theory that this new quark should be the most massive, and was therefore given the name of "top" quark. The top quark was finally discovered at FNAL Tevatron in 1995 by two independent collaborations examining 1.8 TeV proton-antiproton collisions [33, 34]. A figure showing the measurement which led to the discovery of the top quark can be seen in Fig. 1.5.

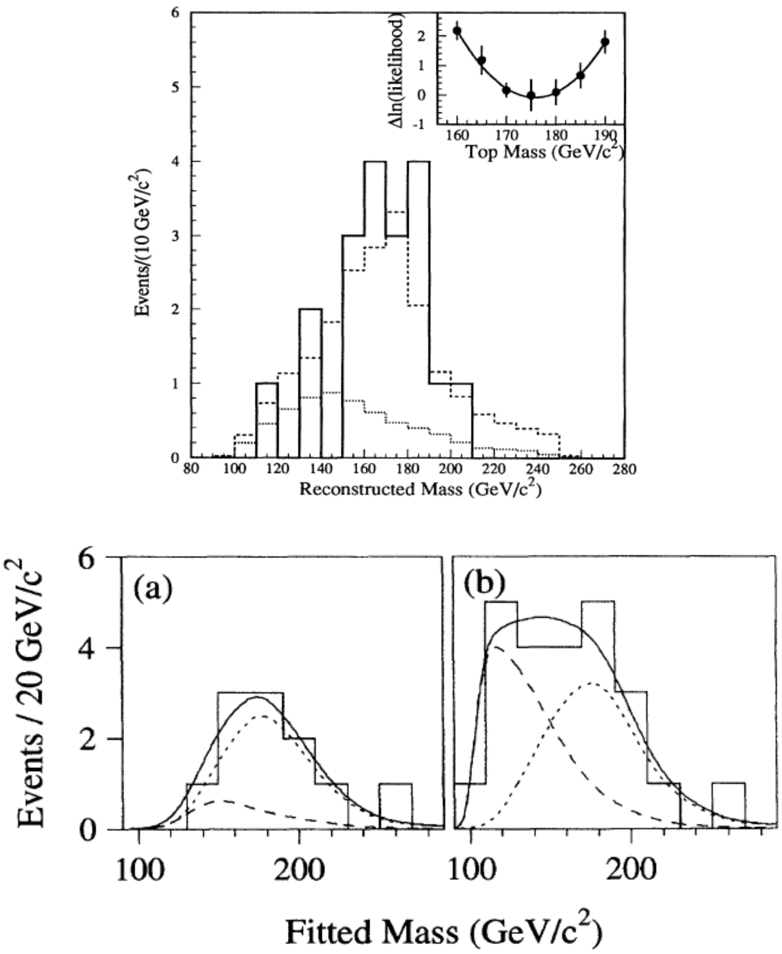

Figure 1.5: The measurement showing the discovery of the top quark by the CDF (top, from Ref. [33]) and D0 (bottom, from Ref. [34]) at the FNAL Tevatron.

The final fundamental particle to have been discovered is the Higgs particle, which was discovered in 2012 by two independent experiments using 7 and 8 TeV proton-proton collisions at the Large Hadron Collider (LHC) [35, 36]. The Higgs boson was famous for its elusiveness over the course of the development of particle physics, and its discovery completed the development of the theory known as the standard model which describes all of the known particles. The properties of the Higgs boson and the experiments used to detect it, as well as the standard model theory, will be discussed in subsequent chapters of this dissertation. Figures showing the discovery of the Higgs boson can be seen in Fig. 1.6.

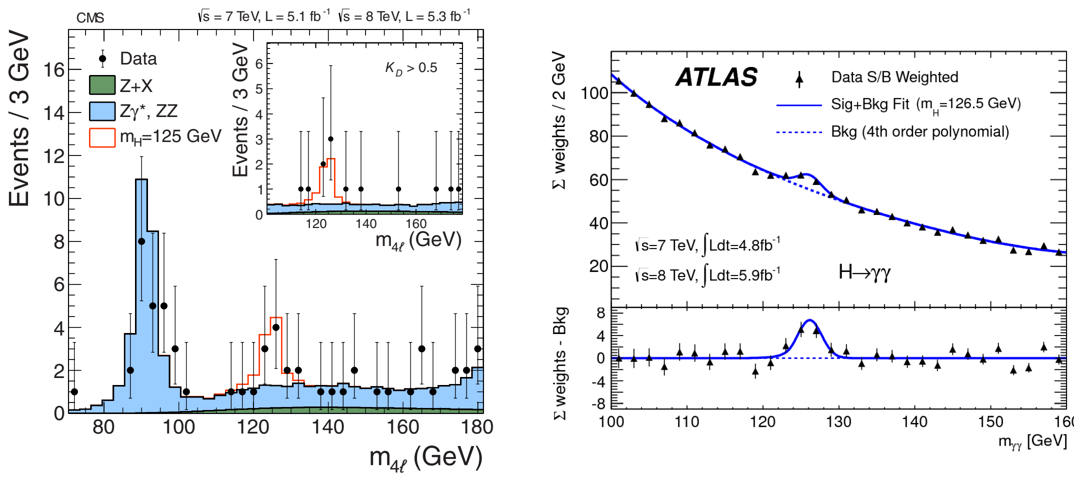

Figure 1.6: The discovery at the LHC of the Higgs boson decaying to a pair of Z bosons in the CMS experiment (left, from Ref. [35]) and decaying to two photons in the ATLAS experiment (right, from Ref. [36]).

In summary, over the span of approximately 120 years the fundamental particles seen in Fig. 1.7 [37] have been discovered in near continuous succession. The particles can be grouped into three generations of quarks and leptons which make up matter, along with several force carrying particles and the Higgs particle. Although not exactly what the ancient Greek philosophers imagined in the fifth century B.C., the particles while not infinite in number (as far as we can tell) do come in many “shapes” and “sizes”. The search for new fundamental particles continues today, because as will be shown in the next section there is strong evidence the picture is still incomplete.

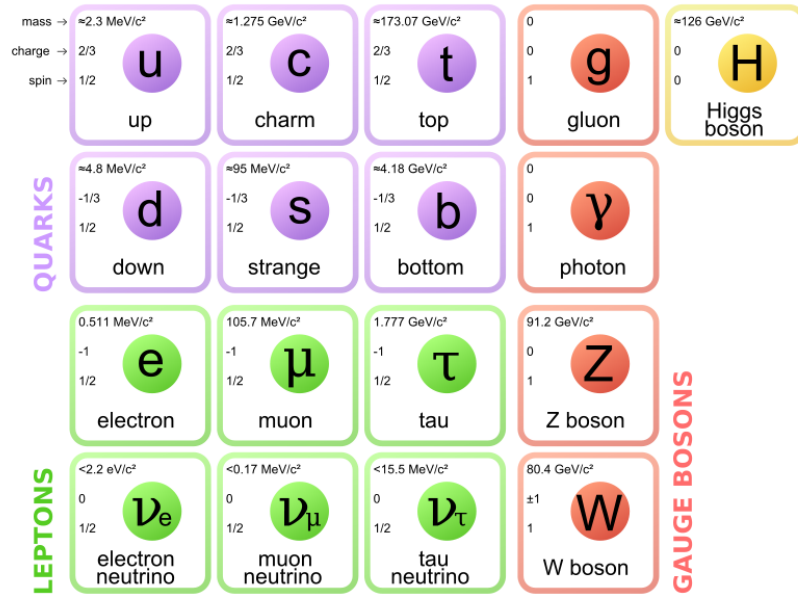

Figure 1.7: The known fundamental particles of nature. From Ref. [37].

1.2 Open Questions in Particle Physics

1.2.1 Dark Matter

There is strong evidence for the existence of at least one new type of particle which has yet to be adequately identified. By measuring the velocity distribution of stars in distant galaxies, astronomers in the 1970's deduced that there was some invisible form of matter which was exerting a gravitational force [38]. A graph of the mean velocities of stars as a function of distance from the galactic center for 21 spiral galaxies can be seen in Fig 1.8, which shows the velocity of starts at large distances from the center of the galaxy being much greater than possible if the only mass in the galaxy is the visible matter. Further evidence for the existence of this "dark matter" was provided by its gravitational effects on light [39]. According to recent results from the Planck Collaboration, the dark matter makes up 26.8% of the mass-energy density of the universe [40]. The standard model of cosmology, which works extremely well in describing the abundance of light elements in the universe, also provides strong theoretical motivation that dark matter is made up elementary particles left over from the earliest moments after the creation of the universe [41].

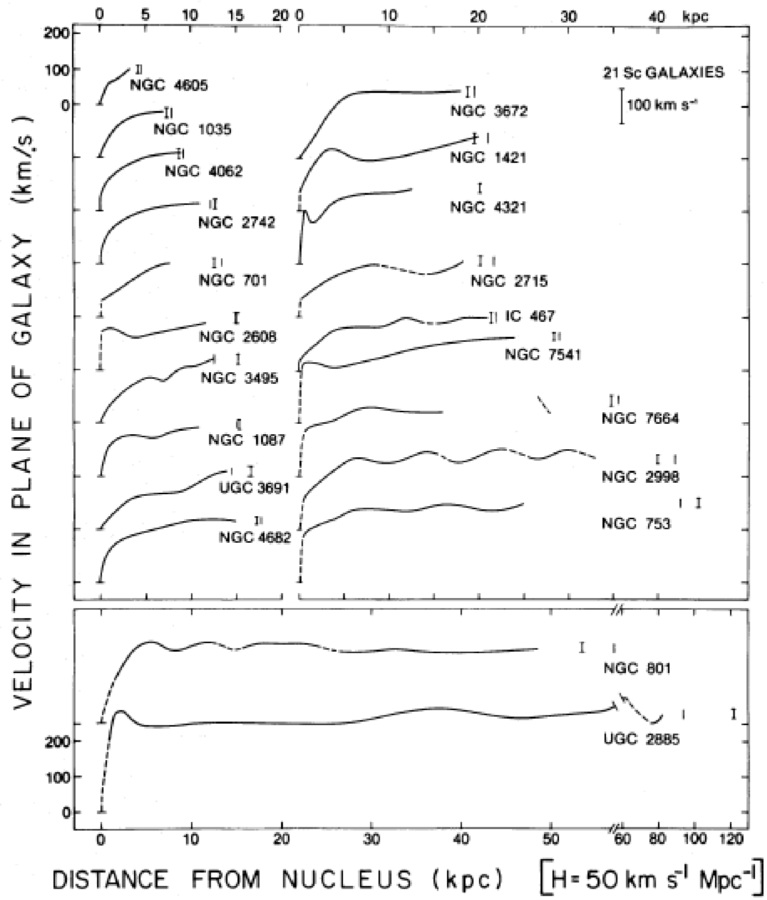

Figure 1.8: Mean velocities of stars as a function of distance from the galactic center for 21 spiral galaxies, indicating the presence of dark matter.

1.2.2 Neutrino Masses

The study of neutrinos has always been a challenge due to the fact that they are electrically neutral and their interaction with matter is extremely weak. It was often speculated that they might have a small mass, but it was so small that the hypothesis could not be directly proven. A long standing problem related to neutrinos, which would eventually help resolve this question, was a series of observations beginning 1968 by Raymond Davis that the flux of neutrinos from the sun was only one third of the theoretical prediction [42].

This was known as the “solar neutrino problem”, and it was resolved in 1998 by the Super-Kamiokande experiment [43] and further clarified in 2001 by the SNO experiment [44]. These experiments provided evidence that neutrinos can change from one flavor (electron, muon or tau neutrino) to into another as they propagate, a phenomena which can only occur if neutrinos have mass. Oscillation experiments can only measure differences of squared neutrino masses $|\Delta m^2|$, but do provide a constraint that one of the neutrino masses must be at least 0.04 eV [45]. Furthermore, by studying the cosmic background radiation an upper limit of 0.23 eV can be found for the sum of all the neutrino masses [46]. Therefore the neutrino mass scale is more than 500,000 times smaller than the mass of the electron. Finally, a key observation of about neutrinos is that they only have left-handed chirality. Without a right-handed neutrino, the neutrino masses can not arise in the same way as the other particles. These considerations provide strong evidence that the current understanding of neutrinos is incomplete, and that a more complete theory exists which might include additional particles.

1.2.3 Baryon Asymmetry

As discussed earlier, for every particle there is also a partner “anti”-particle. For example, the anti-particle to the electron is the positron. When a matter particle and and anti-matter particle meet each other, they annihilate leaving pure energy. The calculation of the abundance of light elements fixes the ratio of baryons to photons in the primordial universe to be approximately 10^{-10} [47]. Therefore there must be some mechanism through which total annihilation of matter and anti-matter is avoided. The necessary conditions for this were first laid out by Andrei Sakharov in 1967 [48]. One of the necessary conditions is a process which violates the total baryon number. Such processes do occur in the standard model theory of particles and forces, but not at a rate large enough to produce the observed baryon density [47]. Therefore, there must be some extension to the current theory which explains why all of the planets, stars and galaxies exist at all.

1.2.4 Unified Theories

Finally, there is a long standing desire by physicists to create a theory of particles and forces which combines the electromagnetic, weak and strong forces, and all of the known particles of nature into a single theory. Such proposed theories are called a Grand Unified Theories (GUTs). As will be shown in the next chapter, the idea has already been successfully applied to the electromagnetic and weak nuclear forces, which are now known to be part of a single "electroweak" force. One of the first GUTs was the Georgi-Glashow model [49], which was able to combine all the particles and forces into a single theoretical structure. In the model there are additional force carrying particles, called X and Y bosons, which can cause the proton to decay [50]. To date no evidence of proton decay has been found, which means the mass of the hypothetical bosons must be very large, at least 10^{16} GeV. Such high masses are beyond the reach of direct production in any foreseen laboratory experiments, and therefore unless proton decay is observed the idea of a GUT remains speculative. However it is an interesting possibility which often leads to new particles, and perhaps they could be discovered in future experiments.

Chapter 2

Theory

2.1 The Standard Model

In this section, the theoretical framework which describes the elementary particles and their interactions will be reviewed in a manner similar to several other reviews [45, 51–56]. The theory through which the elementary particles and forces are understood is referred to as the standard model (SM) of particle physics. The SM combines the ideas of special relativity with quantum mechanics into a quantum field theory. The matter fields (electron, quarks, neutrinos, etc.) are fermions with spin $1/2$, and the force fields (photon, gluon, W, Z) are bosons with spin 1 and mediate interactions amongst the fermions. The experimental observations outlined in the previous chapter suggests that the matter fields are organized into three generations which are identical in every way except for their masses. Finally, the most important pieces of the SM are its symmetries which lead to the interactions and conserved quantities. It should be pointed out that the SM provides a consistent framework for understanding the electromagnetic, strong, and weak nuclear forces, but it does not describe gravity.

2.1.1 Electroweak Interaction

The electromagnetic and weak forces are based on the principle of local gauge symmetry, with the symmetry group $SU(2) \times U(1)$ first identified by Sheldon Glashow in 1961 [57].

The conserved quantum number of the SU(2) symmetry is known as the weak isospin and is denoted as T_3, and for U(1) the conserved quantum number is the weak hypercharge denoted by Y. For each generator of the symmetry group, there is an associated gauge field which is required to preserve the symmetry of the Langrangian under the local gauge transformations. In the case of SU(2) there are three gauge fields $W_\mu^{1,2,3}$ with gauge coupling g, and in the case of U(1) there is one gauge field B_μ with gauge coupling g'. The generators of the SU(2) group are equivalent to one half of the Pauli matrices:

$$T^a = \frac{1}{2}\sigma^a; \quad \sigma^1 = \begin{pmatrix} 0 & 1 \\ 1 & 0 \end{pmatrix}, \quad \sigma^2 = \begin{pmatrix} 0 & -i \\ i & 0 \end{pmatrix}, \quad \sigma^3 = \begin{pmatrix} 1 & 0 \\ 0 & -1 \end{pmatrix} \tag{2.1}$$

The generators of the SU(2) group are 2×2 hermitian matrices (unitary) with determinant $= 1$ (special), hence the name SU(2). The commutation relations of the generators are given by:

$$[T^a, T^b] = i\epsilon^{abc}T_c \quad \text{and} \quad [Y, Y] = 0 \tag{2.2}$$

The field-strength tensors corresponding to these gauge fields are given by:

$$\begin{aligned} W^a_{\mu\nu} &= \partial_\mu W^a_\nu - \partial_\nu W^a_\mu - g\epsilon^{abc}W^b_\mu W^c_\nu \\ B_{\mu\nu} &= \partial_\mu B_\nu - \partial_\nu B_\mu \end{aligned} \tag{2.3}$$

The next step is to identify how the fermion fields transform under the symmetry groups. First, it is important to point out that the left-handed and right-handed chiral components of a fermion field $f_{L,R} = \frac{1}{2}(1 \mp \gamma_5)f$ transform differently under the SM electroweak gauge symmetry. This possibility was first suggested by C. N. Yang and T. D. Lee [58] and verified experimentally by C. S. Wu [59] in 1956. These results showed that the weak interaction only acts on left-handed components of the fermion fields. This observation leads to the correct assignment being to place the left-handed components of the lepton and quark fields into doublets of SU(2):

$$
\begin{gathered}
L_i = \begin{pmatrix} \nu_i \\ \ell_i^- \end{pmatrix}_L ; \qquad Q_i = \begin{pmatrix} u_i \\ d_i \end{pmatrix}_L \\
\nu_1 = \nu_e,\ \nu_2 = \nu_\mu,\ \nu_3 = \nu_\tau;\ \ell_1^- = e^-,\ \ell_2^- = \mu^-,\ \ell_3^- = \tau^- \\
u_1 = u,\ u_2 = c,\ u_3 = t;\ d_1 = d,\ d_2 = s,\ d_3 = b
\end{gathered}
\tag{2.4}
$$

The right-handed components of the lepton and quark fields ($\ell_{i_R}, u_{i_R},$ and d_{i_R}) are singlets under SU(2). Therefore the left-handed fermions have $T_3 = \pm\frac{1}{2}$ and the right handed fermions have $T_3 = 0$. The hypercharge Y is defined through the isospin T_3 and the electric charge Q as $Y = 2(Q - T_3)$, giving:

$$
Y_{L_i} = -1; \quad Y_{\ell_{i_R}} = -2; \quad Y_{Q_i} = \frac{1}{3}; \quad Y_{u_{i_R}} = \frac{4}{3}; \quad Y_{d_{i_R}} = -\frac{2}{3} \tag{2.5}
$$

The electroweak Lagrangian for massless fermions and gauge bosons is then given by:

$$
\begin{aligned}
\mathcal{L}_{EW} = -\frac{1}{4}B_{\mu\nu}B^{\mu\nu} - \frac{1}{4}W^a_{\mu\nu}W_a^{\mu\nu} + \ \overline{L}_i i D_\mu \gamma^\mu L_i \ + \ \overline{\ell}_{i_R} i D_\mu \gamma^\mu \ell_{i_R} \\
+ \ \overline{Q}_i i D_\mu \gamma^\mu Q_i \ + \ \overline{u}_{i_R} i D_\mu \gamma^\mu u_{i_R} \ + \ \overline{d}_{i_R} i D_\mu \gamma^\mu d_{i_R}
\end{aligned}
\tag{2.6}
$$

where we have introduced the gauge covariant derivative, through which the fermions are minimally coupled to the gauge bosons:

$$
D_\mu \equiv \begin{cases} \partial_\mu + ig\frac{\sigma^a}{2}W^a_\mu + ig'\frac{Y}{2}B_\mu & \text{(doublets)} \\ \partial_\mu + ig\frac{Y}{2}B_\mu & \text{(singlets)} \end{cases} \tag{2.7}
$$

The electroweak Lagrangian $\mathcal{L}_{EW}$ is invariant under local SU(2) $\times$ U(1) gauge transformations. For the matter fields the transformation rules are:

$$
\begin{aligned}
\psi_L(x) &\to \psi'_L(x) \equiv e^{i\vec{\alpha}(x)\cdot\frac{\vec{\sigma}}{2} + i\beta(x)Y}\psi_L(x) \\
\psi_R(x) &\to \psi'_R(x) \equiv e^{i\beta(x)Y}\psi_R(x)
\end{aligned}
\tag{2.8}
$$

where $\psi_L(x)$ can be either the lepton SU(2) doublet L or quark SU(2) doublet Q from Eqn. 2.4 and $\psi_R(x)$ can be any of the SU(2) singlets. The gauge invariance requires the gauge fields transform accordingly as:

$$\vec{W}_\mu(x) \to \vec{W}_\mu(x) - \frac{1}{g}\partial_\mu \vec{\alpha}(x) - \vec{\alpha}(x) \times \vec{W}_\mu(x)$$
$$B_\mu(x) \to B_\mu(x) - \frac{1}{g}\partial_\mu \beta(x) \tag{2.9}$$

The Lagrangian in Eqn. 2.6 contains interaction terms between the matter fields and the gauge fields. It is convenient to split the interaction terms into two pieces. The first piece is responsible for the charged current interactions:

$$\mathcal{L}_{EW} \supset \mathcal{L}_{\mathrm{CC}} = -g\overline{L}_i \frac{\sigma^a}{2} W_\mu^a \gamma^\mu L_i - g\overline{Q}_i \frac{\sigma^a}{2} W_\mu^a \gamma^\mu Q_i \tag{2.10}$$

This can be written more explicitly as:

$$\mathcal{L}_{\mathrm{CC}} = -\frac{g}{2\sqrt{2}} W_\mu^- \left[\overline{\nu_i}\gamma^\mu(1-\gamma^5))\ell_i^- + \overline{u}_i \gamma^\mu (1-\gamma^5))d_i\right] + \mathrm{h.c.} \tag{2.11}$$

where $W_\mu^\pm \equiv (W_\mu^1 \pm iW_\mu^2)/\sqrt{2}$. Thus the $W_\mu^\pm$ boson fields give rise to interactions between quarks or leptons of the same SU(2) doublet. The interpretation of neutron decay, for example, is the transformation of a d quark into a u quark through the emission of a W_μ^- which in turn decays into an electron and neutrino. A Feynman diagram depicting this process can be seen in Fig. 2.1.

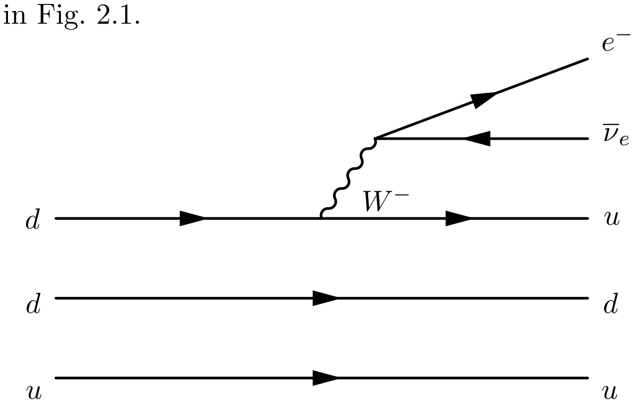

Figure 2.1: A Feynman diagram representing a neutron decaying into a proton.

It should be pointed out that for quarks, the weak eigenstates are not the same as the mass eigenstates. Therefore to be completely correct the SU(2) quark doublets should be written as:

$$Q_i = \begin{pmatrix} u_i \\ d'_i \end{pmatrix}_L \quad , \quad d'_i = \Sigma_j V_{ij} d_j \tag{2.12}$$

where the matrix V_{ij} is known as the Cabibbo-Kobayashi-Maskawa (CKM) matrix [45]. Therefore there are flavor changing charged currents within the SM, but the off diagonal elements of the CKM matrix are much smaller then the diagonal elements. The matrix can be parameterized by three angles and one phase, which gives rise to all of the CP (combined charge and parity symmetry) violation in flavor changing processes within the SM.

The remaining fermion interaction terms involve the neutral gauge boson fields B_μ and W^3_μ. It is natural to try to identify these fields with the physical Z boson and photon, even though at this point all of the fields are massless and the physical Z boson is massive. Therefore the following linear combination can be defined:

$$\begin{pmatrix} Z_\mu \\ A_\mu \end{pmatrix} = \begin{pmatrix} \cos\theta_W & -\sin\theta_W \\ \sin\theta_W & \cos\theta_W \end{pmatrix} \begin{pmatrix} W^3_\mu \\ B_\mu \end{pmatrix} \tag{2.13}$$

In terms of these fields, the electroweak Lagrangian in Eqn. 2.6 also contains neutral current interactions:

$$\begin{aligned} &\mathcal{L}_{EW} \supset \mathcal{L}_{\text{NC}} = \\ &-\overline{\psi}_i \gamma^\mu \left(A_\mu \left[g\frac{\sigma^3}{2}\sin\theta_W + g'\frac{Y}{2}\cos\theta_W \right] + Z_\mu \left[g\frac{\sigma^3}{2}\cos\theta_W - g'\frac{Y}{2}\sin\theta_W \right] \right) \psi_i \end{aligned} \tag{2.14}$$

where ψ can be either an SU(2) doublet or singlet. In order to make the connection with electromagnetism the following relation should be true:

$$g\sin\theta_W = g'\cos\theta_W = e \tag{2.15}$$

Then recalling that $Y = 2(Q - T_3)$, $\mathcal{L}_{\text{NC}}$ can be written as the sum of the photon and Z currents:

$$\begin{aligned} \mathcal{L}_{\mathrm{NC}} &= \mathcal{L}_{\mathrm{NC}}^{\gamma} + \mathcal{L}_{\mathrm{NC}}^{Z} \\ \mathcal{L}_{\mathrm{NC}}^{\gamma} &= -e\overline{\psi}_i \gamma^{\mu} A_{\mu} Q \psi_i \\ \mathcal{L}_{\mathrm{NC}}^{Z} &= -\frac{e}{2\sin\theta_W \cos\theta_W} \overline{\psi}_i \gamma^{\mu} Z_{\mu} \left(\sigma^3 - 2\sin^2\theta_W Q\right) \psi_i \end{aligned} \tag{2.16}$$

In this way the SU(2) algebra generates the $\psi\overline{\psi}\gamma$ and $\psi\overline{\psi}Z$ interactions. it should also be pointed out that there are also gauge boson self-interactions generated by the Lagrangian in Eqn. 2.6 of the form γW^+W^-, ZW^+W^-, $\gamma\gamma W^+W^-$, ZZW^+W^-, and $W^+W^-W^+W^-$.

2.1.2 Strong Interaction

The idea of local gauge symmetry can also be used to understand the strong interaction, which is based on the group of 3×3 herimitian matrices with determinant $= 1$, SU(3). The conserved quantum number of the SU(3) symmetry is known as color, and the quantum theory of the color interaction of quarks and gluons is called Quantum Chromodynamics (QCD). Each species of quark may have $N_C = 3$ different colors (sometimes labeled as red, green, blue):

$$q_i \to A q_i^1 + B q_i^2 + C q_i^3 = A \begin{pmatrix} 1 \\ 0 \\ 0 \end{pmatrix} + B \begin{pmatrix} 0 \\ 1 \\ 0 \end{pmatrix} + C \begin{pmatrix} 0 \\ 0 \\ 1 \end{pmatrix} \tag{2.17}$$

Here the subscripts label the flavor (or generation) and the superscripts denote the color eigenstates. The concept of color was postulated in order to satisfy Fermi-Dirac statistics for all of the observed mesons and baryons. In this way the mesons and baryons can be though of as color singlet combinations of quarks:

$$B = \frac{1}{\sqrt{6}} \epsilon^{\alpha\beta\gamma} \left| q^{\alpha} q^{\beta} q^{\gamma} \right\rangle, \qquad M = \frac{1}{\sqrt{3}} \delta^{\alpha\beta} \left| q^{\alpha} \overline{q}^{\beta} \right\rangle, \tag{2.18}$$

There are 8 generators of SU(3) and the associated gauge fields are $G_{\mu}^{1,\ldots,8}$ with coupling strength g_s. The generators T^a are equivalent to one half of the Gell-Mann matrices λ^a [60]:

$$\lambda^1 = \begin{pmatrix} 0 & 1 & 0 \\ 1 & 0 & 0 \\ 0 & 0 & 0 \end{pmatrix}, \quad \lambda^2 = \begin{pmatrix} 0 & -i & 0 \\ i & 0 & 0 \\ 0 & 0 & 0 \end{pmatrix}, \quad \lambda^3 = \begin{pmatrix} 1 & 0 & 0 \\ 0 & -1 & 0 \\ 0 & 0 & 0 \end{pmatrix},$$
$$\lambda^4 = \begin{pmatrix} 0 & 0 & 1 \\ 0 & 0 & 0 \\ 1 & 0 & 0 \end{pmatrix}, \quad \lambda^5 = \begin{pmatrix} 0 & 0 & -i \\ 0 & 0 & 0 \\ i & 0 & 0 \end{pmatrix}, \quad \lambda^6 = \begin{pmatrix} 0 & 0 & 0 \\ 0 & 0 & 1 \\ 0 & 1 & 0 \end{pmatrix}, \tag{2.19}$$
$$\lambda^7 = \begin{pmatrix} 0 & 0 & 0 \\ 0 & 0 & -i \\ 0 & i & 0 \end{pmatrix}, \quad \lambda^8 = \frac{1}{\sqrt{3}} \begin{pmatrix} 1 & 0 & 0 \\ 0 & 1 & 0 \\ 0 & 0 & -2 \end{pmatrix}$$

The generators of the SU(3) group obey the following commutation relations:

$$[T^a, T^b] = i f^{abc} T_c \tag{2.20}$$

where f^{abc} are the structure constants. The field-strength tensor corresponding to the gauge fields is given by:

$$G^a_{\mu\nu} = \partial_\mu G^a_\nu - \partial_\nu G^a_\mu - g_s f^{abc} G^b_\mu G^c_\nu \tag{2.21}$$

The quarks then transform as color triplets under SU(3) gauge transformations and the leptons transform as color singlets. The SU(3) gauge transformation for the quark color triplets is:

$$q^\alpha_i(x) \rightarrow q^{\alpha\prime}_i(x) \equiv e^{i\vec{\theta}(x)\cdot\frac{\vec{\lambda}}{2}} q^\alpha_i(x) \tag{2.22}$$

and the gauge fields transform accordingly as:

$$G^a_\mu(x) \rightarrow G^a_\mu(x) - \frac{1}{g_s}\partial_\mu \theta^a(x) - f^{abc}\theta^b(x) G^c_\mu(x) \tag{2.23}$$

The SU(3) × SU(2) × U(1) gauge covariant derivative for quarks analogous to the one for SU(2) × U(1) in Eqn. 2.7 is:

$$D_\mu \equiv \begin{cases} \partial_\mu + ig_s \frac{\lambda^a}{2} G^a_\mu + ig\frac{\sigma^a}{2} W^a_\mu + ig'\frac{Y}{2} B_\mu & \text{for SU(2) doublets} \\ \partial_\mu + ig_s \frac{\lambda^a}{2} G^a_\mu + ig'\frac{Y}{2} B_\mu & \text{for SU(2) singlets} \end{cases} \tag{2.24}$$

The full SM Lagrangian invariant under SU(3) $\times$ SU(2) $\times$ U(1) gauge transformations is then:

$$\begin{aligned} \mathcal{L}_{SM} = -\frac{1}{4} B_{\mu\nu} B^{\mu\nu} - \frac{1}{4} W^a_{\mu\nu} W^{\mu\nu}_a - \frac{1}{4} G^a_{\mu\nu} G^{\mu\nu}_a + \; \overline{L}_i i D_\mu \gamma^\mu L_i \; + \; \overline{\ell}_{i_R} i D_\mu \gamma^\mu \ell_{i_R} \\ + \overline{Q}_i i D_\mu \gamma^\mu Q_i \; + \; \overline{u}_{i_R} i D_\mu \gamma^\mu u_{i_R} \; + \; \overline{d}_{i_R} i D_\mu \gamma^\mu d_{i_R} \end{aligned} \tag{2.25}$$

This contains the interaction terms between the quarks and gluons:

$$\mathcal{L}_{SM} \supset -g_s \overline{q}^\alpha_i G^a_\mu \left(\frac{\lambda^a}{2} \right)_{\alpha\beta} q^\beta_i \tag{2.26}$$

The G^a_μ couple to quarks of a single generation in different color states. The complex interactions which bind the constituent quarks of a proton can be imagined to be similar to that shown in Fig. 2.2.

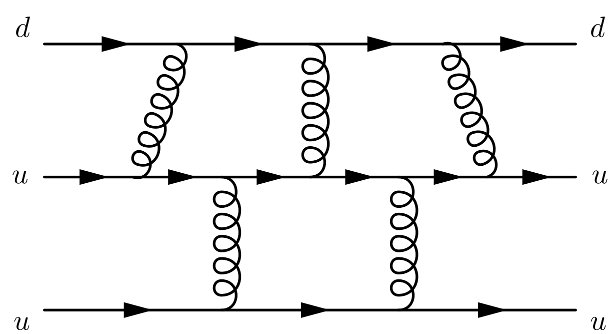

Figure 2.2: A Feynman diagram representing gluon exchange within a proton.

Like in the SU(2) $\times$ U(1) case, the G^a_μ also have cubic and quartic self interactions. In both cases the gauge boson self interaction is due to the non-Abelian nature of SU(2) and SU(3) groups. It is interesting to note that the cubic self interaction is the primary mechanism for producing top-quark pairs in proton-proton collisions, shown in in Fig. 2.3.

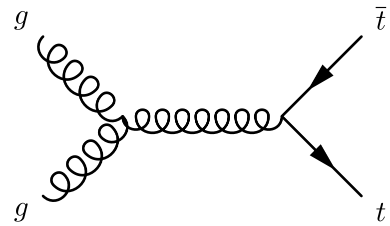

Figure 2.3: A Feynman diagram representing top-quark pair production in proton-proton collisions.

2.1.3 Higgs Mechanism

The Lagrangian of Eqn. 2.25 describes a theory of massless fermions and gauge bosons. However, it is clear that the fermions in the SM indeed have mass. Suppose that a mass term $-m_f\overline{\psi}_f\psi_f$ for each SM fermion f was added to the Lagrangian. This term is invariant under SU(3) transformations, but would violate the SU(2) symmetry. This can be seen by considering the case of the electron:

$$-m_e\bar{e}e = -m_e\bar{e}\left(\bar{e}_R e_L + \bar{e}_L e_R\right) \tag{2.27}$$

which is manifestly non-invariant because the left-handed component is an SU(2) doublet whereas the right-handed component is an SU(2) singlet. More importantly, from a historical perspective, a mass term for the W bosons $\frac{1}{2}M_W^2 W_\mu W^\mu$ would also violate the SU(2) symmetry. It was assumed for a long time that the mediators of the weak force were massive, and that this was responsible for the forces short range nature. As shown in Sec. 1.1 this was eventually proven experimentally. What came to be known as the Higgs mechanism was proposed by several people in 1964 [61–64] as a way to explain how to generate masses for the vector gauge bosons and the fermions without violating SU(2) × U(1) gauge invariance.

In the SM the Higgs mechanism introduces a complex SU(2) doublet of scalar fields:

$$\phi \equiv \begin{pmatrix} \phi^+ \\ \phi^0 \end{pmatrix}, \qquad Y_\phi = +1 \tag{2.28}$$

Next, kinetic and interation terms for this scalar field are added to the SM Lagrangian:

$$\mathcal{L}_\phi = (D_\mu\phi)^\dagger(D^\mu\phi) - V(\phi) \tag{2.29}$$

where the gauge covariant derivative D_μ is the same as in Eqn. 2.7 and the scalar potential $V(\phi)$ contains the interaction terms:

$$V(\phi) = \mu^2\phi^\dagger\phi + \lambda(\phi^\dagger\phi)^2 \tag{2.30}$$

The scalar Lagrangian is invariant under SU(2) $\times$ U(1) gauge transformations for any values of μ^2 and λ. In order for the potential to have a minimum energy, λ must be positive. If the $\mu^2 > 0$, there is a unique minimum of the potential at:

$$\langle\phi\rangle_0 \equiv \langle 0|\phi|0\rangle = \begin{pmatrix} 0 \\ 0 \end{pmatrix} \tag{2.31}$$

and the ground state maintains the symmetry of the Lagrangian. If $\mu^2 < 0$, however, the ground state has an expectation value in the vacuum:

$$\langle\phi\rangle_0 \equiv \langle 0|\phi|0\rangle = \begin{pmatrix} 0 \\ \frac{v}{\sqrt{2}} \end{pmatrix}, \qquad v \equiv \sqrt{\frac{-\mu^2}{\lambda}} \tag{2.32}$$

In order for the symmetries of the Lagrangian to be respected by the ground state, the action of the group generators $\mathcal{G}$ on the ground state should return the ground state. That is to say $e^{i\alpha\mathcal{G}}\langle\phi\rangle_0 = \langle\phi\rangle_0$, or $\mathcal{G}\langle\phi\rangle_0 = 0$. This can be checked for the U(1) generator and one of the SU(2) generators:

$$\begin{aligned} Y\langle\phi\rangle_0 = Y_\phi\langle\phi\rangle_0 = +1\langle\phi\rangle_0 &= \begin{pmatrix} 0 \\ \frac{v}{\sqrt{2}} \end{pmatrix} \neq 0 \\ \sigma^1\langle\phi\rangle_0 = \begin{pmatrix} 0 & 1 \\ 1 & 0 \end{pmatrix}\begin{pmatrix} 0 \\ \frac{v}{\sqrt{2}} \end{pmatrix} &= \begin{pmatrix} \frac{v}{\sqrt{2}} \\ 0 \end{pmatrix} \neq 0 \end{aligned} \tag{2.33}$$

Therefore SU(2) $\times$ U(1) invariance has been broken. The ground state is however invariant under the action of the electric charge generator Q:

$$Q\left\langle\phi\right\rangle_0=\frac{1}{2}(T_3+Y)\left\langle\phi\right\rangle_0=\frac{1}{2}\left(\begin{array}{cc}Y_\phi+1 & 0\\ 0 & Y_\phi-1\end{array}\right)\left(\begin{array}{c}0\\ \frac{v}{\sqrt{2}}\end{array}\right)=\left(\begin{array}{c}0\\ 0\end{array}\right)=0 \tag{2.34}$$

Thus there is still a remaining U(1) symmetry which is identified with electromagnetism.

In order to see how the gauge bosons acquire mass by the Higgs mechanism, the scalar doublet is first written in a general form as a first order expansion around the minimum of the potential:

$$\phi(x)=\left(\begin{array}{c}\theta_2(x)+i\theta_1(x)\\ \frac{1}{\sqrt{2}}\left[v+H(x)\right]-i\theta_3(x)\end{array}\right)=e^{i\frac{\sigma^a}{2}\theta_a(x)}\frac{1}{\sqrt{2}}\left(\begin{array}{c}0\\ v+H(x)\end{array}\right) \tag{2.35}$$

The SU(2) invariance of the Lagrangian allows the choice of $\theta^a(x)=0$, which is called the unitary gauge. In this gauge the kinetic term of the Lagrangian in Eqn. 2.29 takes the following form:

$$(D_\mu\phi)^\dagger(D^\mu\phi)\rightarrow\frac{1}{2}\partial_\mu H\partial^\mu H+(v+H)^2\left\{\frac{g^2}{4}W_\mu^\dagger W^\mu+\frac{g^2}{8\cos^2\theta_W}Z_\mu Z^\mu\right\} \tag{2.36}$$

There are therefore now, after breaking the SU(2) $\times$ U(1) symmetry, mass terms for the W and Z gauge bosons. In addition there are terms giving HW^+W^-, HHW^+W^-, HZZ, $HHZZ$ interactions. The mass terms give at first order:

$$m_W^2=\frac{v^2g^2}{4},\qquad \frac{1}{2}m_Z^2=\frac{v^2g^2}{8\cos^2\theta_W} \tag{2.37}$$

The same scalar doublet can be be used to generate mass terms for the fermions. An SU(2) $\times$ U(1) invariant Yukawa interaction term can be added to the scalar Lagrangian:

$$\mathcal{L}_F=-\lambda_{\ell_i}\overline{L}_i\phi\ell_{R_i}-\lambda_{d_i}\overline{Q}_i\phi d_{R_i}-\lambda_{u_i}\overline{Q}_i\tilde{\phi}u_{R_i}+\text{h.c.} \tag{2.38}$$

where $\tilde{\phi}=i\sigma^2\phi^*$. The constants λ_{f_i} are free parameters which are not related to λ in the scalar potential in Eqn. 2.30. The same steps as for the gauge bosons can be repeated for the fermions, which after symmetry breaking leads to:

$$
\begin{aligned}
\mathcal{L}_F = & -\frac{1}{\sqrt{2}}\lambda_{\ell_i}(\overline{\nu}_i, \overline{\ell}_{L_i}) \begin{pmatrix} 0 \\ v+H \end{pmatrix} \ell_{R_i} \\
& -\frac{1}{\sqrt{2}}\lambda_{d_i}(\overline{u}_{L_i}, \overline{d}_{L_i}) \begin{pmatrix} 0 \\ v+H \end{pmatrix} d_{R_i} \\
& -\frac{1}{\sqrt{2}}\lambda_{u_i}(\overline{u}_{L_i}, \overline{d}_{L_i}) \begin{pmatrix} 0 & 1 \\ -1 & 0 \end{pmatrix} \begin{pmatrix} 0 \\ v+H \end{pmatrix} u_{R_i} \\
& = -\frac{1}{\sqrt{2}}\lambda_{\ell_i}\overline{\ell}_{L_i}(v+H)\ell_{R_i} - -\frac{1}{\sqrt{2}}\lambda_{q_i} q_{L_i}(v+H) q_{R_i}
\end{aligned}
\tag{2.39}
$$

which give the mass terms to the fermions $m_f = \lambda_f v/\sqrt{2}$. Note that there are no mass terms for the neutrinos. There are also terms giving $H\overline{f}_L f_R$ couplings.

Finally, the physical Higgs boson itself has mass and self-interaction terms coming from the scalar potential in Eqn. 2.30. After symmetry breaking, the potential terms in the Lagrangian can be written as:

$$
\mathcal{L}_V = -\frac{1}{2}\lambda v^2 (v+H)^2 + \frac{1}{4}\lambda(v+H)^4 \tag{2.40}
$$

which gives the mass of the Higgs boson at first order to be $M_H^2 = 2\lambda v^2$. There are also the terms giving rise to the HHH and $HHHH$ self-interactions.

2.1.4 Experimental Tests

The theory outlined in the previous sections is full of phenomenology, of which only a small subset will be discussed here. Many experimental observations such as the particle content of nature, the family structure of the fermions, and parity violation in the weak interactions are already built into the theory. Furthermore, one can consider additional predictions of the theory. The most obvious prediction is the existence of the neutral Z boson which can couple to the neutrinos. This was the first prediction of the SU(2) $\times$ U(1) electroweak theory to be verified by experiment. The neutral current process $\nu_\mu/\overline{\nu}_\mu + \mathrm{N} \rightarrow \nu_\mu/\overline{\nu}_\mu + \mathrm{hadrons}$ was observed by the Gargamelle experiment at CERN in 1973 [65]. The discovery of neutral currents is what prompted the construction of the CERN SPS proton anti-proton collider, where as discussed in Sec. 1.1 the W and Z bosons were directly observed [31, 32].

The SM has been more precisely tested starting at the LEP collider at CERN [66, 67]. The LEP collider studied the process $e^+e^- \to f\overline{f}$. The cross section for $e^+e^- \to$ hadrons as measured by the LEP experiments can be seen in Fig. 2.4. The LEP experiments also measured many other observables which are beyond the scope of this thesis, but as shown in Fig. 2.5, every measurement was in agreement within the measured uncertainties with the SM predictions.

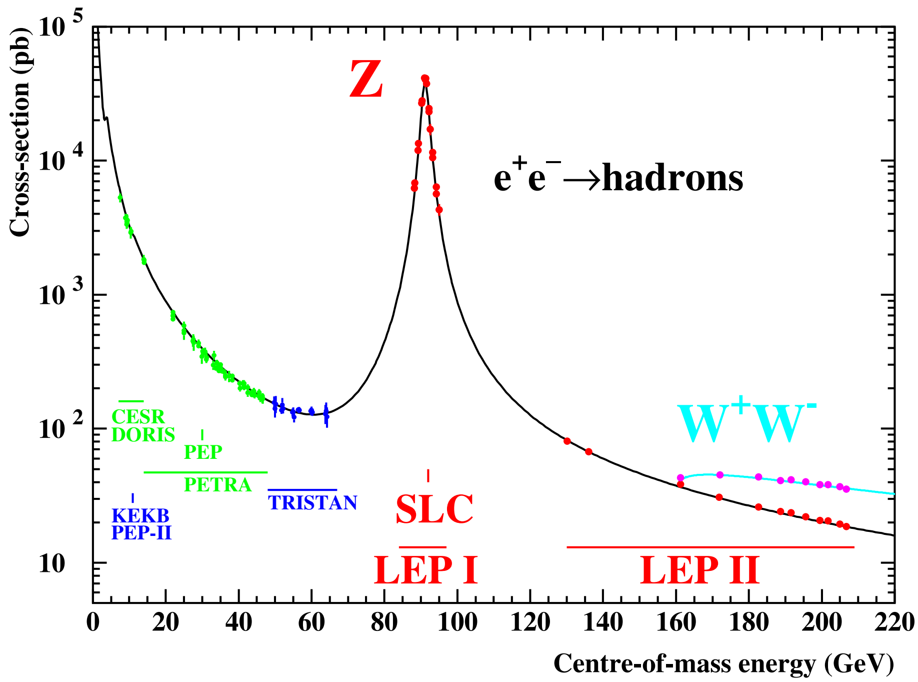

Figure 2.4: The cross section for $e^+e^- \to$ hadrons as measured by the LEP experiments. The solid line is the SM prediction and the points are the experimental measurements. From Ref. [66]

The discovery of the Higgs boson at the LHC was the latest success of the SM. The measured Higgs boson cross section in different decay channels can be seen in Fig. 2.6. So far there are no significant discrepancies with respect the SM predictions, although the measurements have large uncertainties. A major goal of the LHC will be to test precisely

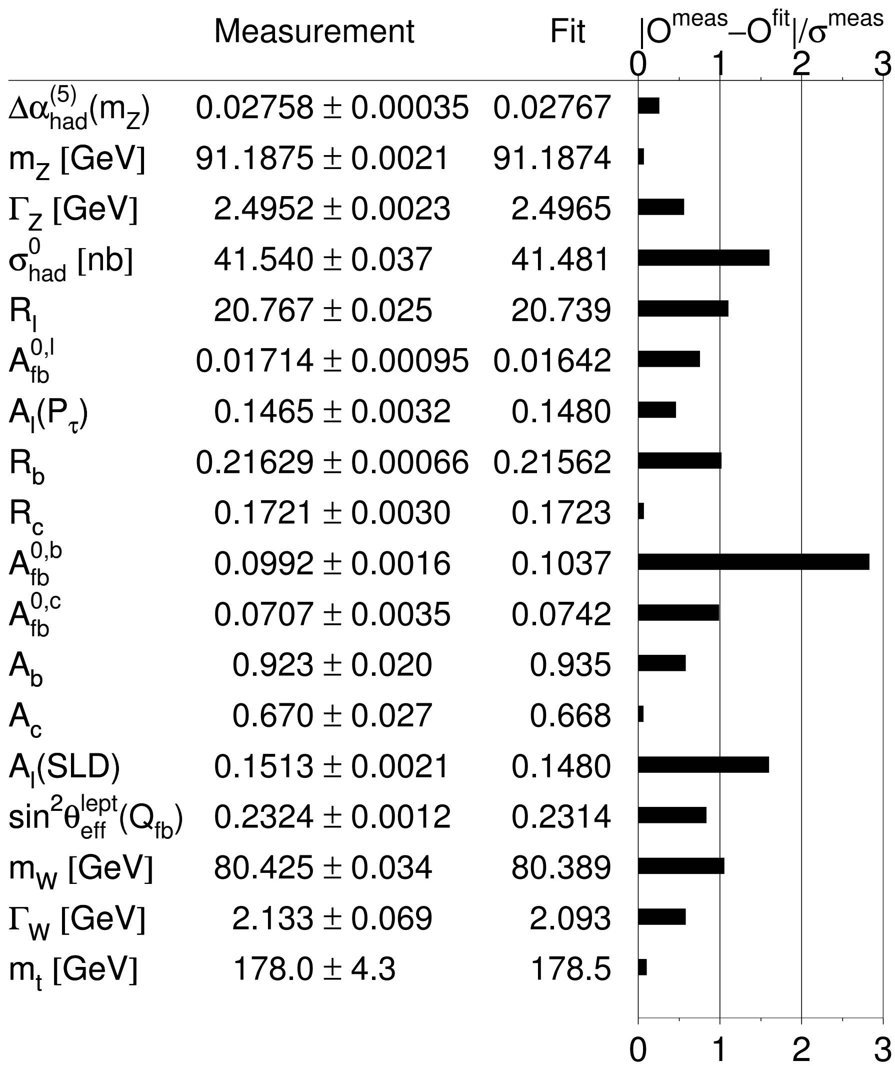

Figure 2.5: Measurement of several SM observables by the LEP experiments and comparison to the theoretical predictions. The number of standard deviations from the SM prediction is shown for each measurement. From Ref. [66]

the predictions of the SM for the Higgs boson properties.

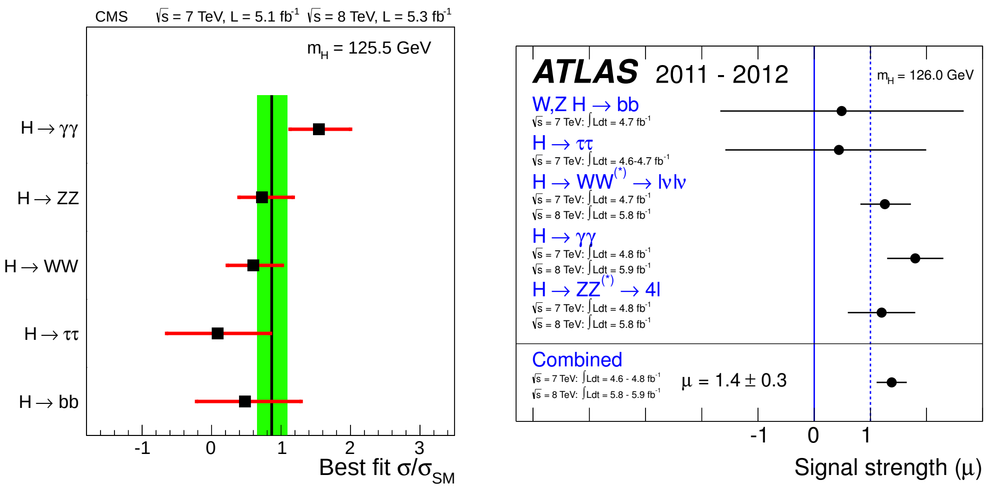

Figure 2.6: Higgs boson cross section in different decay modes as measured by the CMS collaboration (left, from Ref. [35]) and the ATLAS collaboration (right, from Ref. [36]).

2.2 Beyond the Standard Model

The SM does a very good job of describing the results most measurements performed so far. However as was described in Sec. 1.1, there are several reasons to believe that the SM is only an effective theory which breaks down at high enough energy with an instability scale between 10^{16} and 10^{19} GeV. However, besides the reasons already outlined, there is the glaring omission in the SM of anything to do with gravity. The mass or energy scale at which the effects of quantum mechanics, relativity, and gravity might be treated simultaneously can be derived through dimensional analysis of the fundamental constants $\hbar$, c, and G. This leads to a mass scale known as the Planck mass (or Planck scale) and is given by $M_p = \sqrt{\hbar c/G} \approx 10^{18}$ GeV, which is slightly higher than the GUT scale of 10^{16} GeV from Sec. 1.2.4 and well beyond the reach of any current technology. A question which can be asked is why the electroweak scale ($M_W \simeq 80.4$ GeV) is 16 orders of magnitude smaller than the Planck scale. What sets this enormous hierarchy of scales between the forces? This is known as the hierarchy problem. Also, one can ask whether the SM is consistent up to this energy scale, or might new physics beyond the SM be expected at some energy less than the Planck scale?

2.2.1 Higgs Naturalness Problem

The SM with the currently measured values of the Higgs boson mass turns out to be completely consistent up to the Planck scale, if the extremely large hierarchies between the electroweak and GUT or Planck scales are ignored [68]. As shown in Fig. 2.7, according to calculations of the SM the vacuum is on the edge of a stable and meta-stable state.

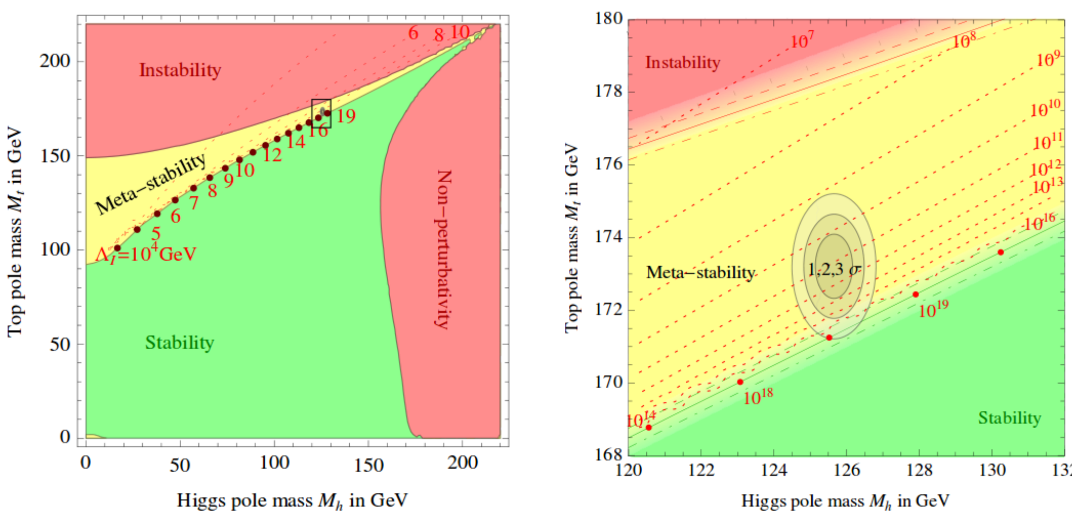

Figure 2.7: A phase diagram of the SM as a functgion of the top quark and Higgs boson masses. The diagram is divided into regions of stabililty, meta-stability, and instability. The circular regions show the best measurements of the top quark and Higgs boson masses. From Ref. [68]

Therefore new physics is not necessarily required at any energy reachable by current technology, but the question of whether or not new physics might be expected is different. This question can be answered in terms of a concept called "naturalness" which demands that the dimensionless parameters of a theory should not have to be extremely fine tuned in order to describe the results of experiments. To see how this applies to the Higgs boson mass, consider the 1-loop Feynman diagrams in Fig. 2.8 which give corrections to the physical

Higgs boson mass. Since the particles propagating in the loops are virtual particles (i.e. they are not observed), they can take on all values of momentum up to infinity. Therefore a cutoff scale Λ must be defined to represent a momentum scale at which the theory no longer makes sense. These diagrams give contributions to the mass of the Higgs boson which are quadratic in the cutoff scale, i.e. $\Delta M^2 \sim \Lambda^2$.

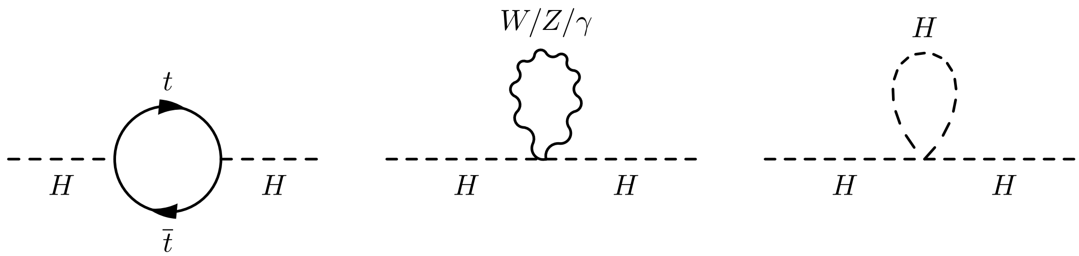

Figure 2.8: Feynman diagrams representing quadratically divergent loop corrections to the Higgs boson mass.

The calculation of the Higgs mass corrections from these diagrams is given in Ref. [69]:

$$\Delta M_t^2 = -\frac{3}{8\pi^2}\lambda_t^2\Lambda^2, \quad \Delta M_{\text{gauge}}^2 = \frac{9}{64\pi^2}g^2\Lambda^2, \quad \Delta M_H^2 = \frac{1}{16\pi^2}\lambda^2\Lambda^2 \tag{2.41}$$

Therefore if the cutoff scale Λ is of the order of the GUT scale of 10^{16} GeV, then the SM parameters must be fine tuned to approximately one part in 10^{16} to recover the observed Higgs boson mass. If the amount of fine tuning is restricted to be at most 10%, the cut off scales should satisfy:

$$\Lambda_{\text{top}} \lesssim 2 \text{ TeV}, \qquad \Lambda_{\text{gauge}} \lesssim 5 \text{ TeV}, \qquad \Lambda_{\text{Higgs}} \lesssim 10 \text{ TeV} \tag{2.42}$$

This naturalness argument is the reason why new physics is expected to manifest at energies $\gtrsim 1$ TeV. Several examples of physics beyond the SM are presented in the next sections.

2.2.2 Supersymmetry

Supersymmetry [70] is a proposed new symmetry between bosons and fermions as an extension to the SM. For every SM particle there is an additional superpartner particle, with spin differing by 1/2. Since fermions and bosons contribute to the radiative corrections to the Higgs mass with opposite sign, such an extension allows for a cancellation of quadratic divergences. Supersymmetry further provides a mechanism to unify the electromagnetic, strong, and weak coupling constants at high scale which implies a unified theory.

The Minimal Supersymmetric Standard Model (MSSM) [71] is the simplest model of Supersymmetry that can produce the SM at the electroweak scale. The MSSM theory is invariant under a new parity-like symmetry called R-parity which is defined as $R = (-1)^{(BL)+2s}$ where L and B are the lepton and baryon number and s is the spin of the particle. This symmetry forbids lepton and baryon number violating terms appearing in the Lagrangian as it is strongly constrained by limits on the proton lifetime. This further implies that the lightest supersymmetric particle (LSP) must be stable, and if it is neutral and weakly interacting then it becomes a good candidate for dark matter.

The MSSM is a very attractive extension to the SM. However direct searches by the CMS experiment for example, which are summarized in Fig. 2.9, have placed severe constraints on the masses of Supersymmetric particles [72], implying that the MSSM is itself somewhat unnatural. It is therefore important to consider alternative solutions to the naturalness problem which do not require Supersymmetry.

2.2.3 Extra Dimensions

Another solution to the naturalness problem can be obtained by introducing additional spatial dimensions beyond the observed three. One such scenario, named the ADD model after its authors [73], assumes δ additional compactified spatial dimensions. In this model, the weakness of gravity arises because it propagates in the extra dimensions while the fermions and gauge bosons are confined to the usual 3 spatial dimensions. This modifies the gravitational potential depending on whether the distance r between two masses is less than or greater than the radius R of the extra dimensions:

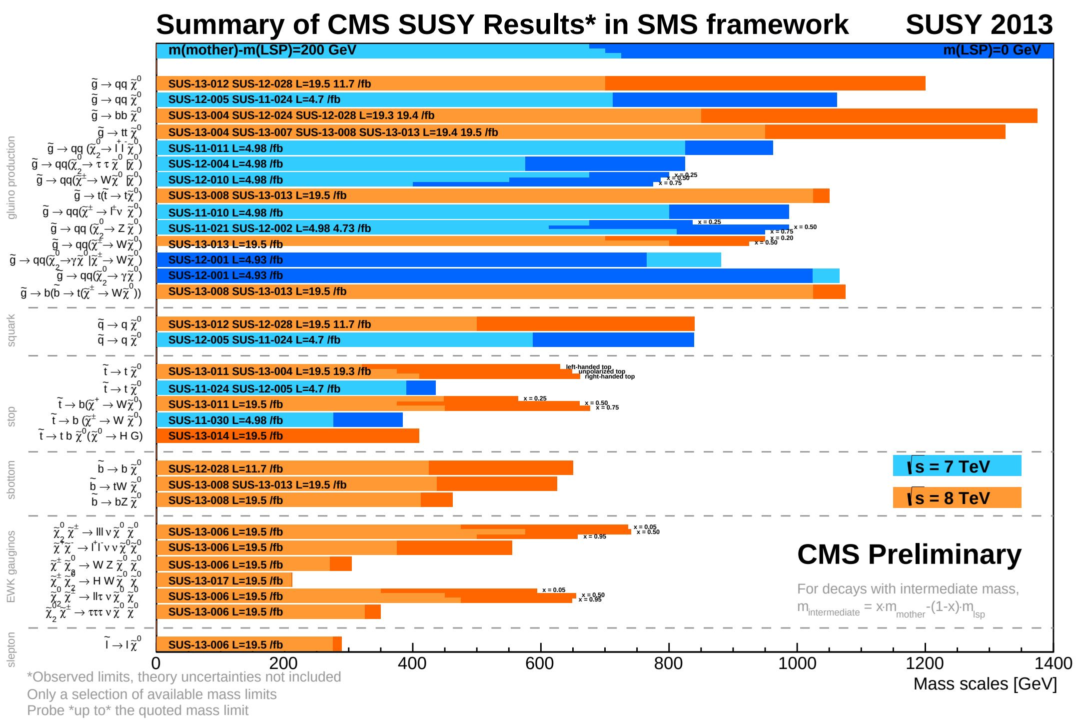

Figure 2.9: Summary of exclusion limits of CMS SUSY searches after the first LHC data taking run. Depending on the details of the SUSY model, the exclusion limits extend to approximately 1.35 TeV for gluino production, 850 GeV for first and second generation squark production, 650 GeV for stop and sbottom production, and 300 GeV for slepton production. From Ref. [72].

$$
\begin{aligned}
V(r) &= \frac{m_1 m_2}{M_{p(4+\delta)}^{\delta+2}} \frac{1}{r^{1+\delta}}, \qquad (r \ll R) \\
V(r) &= \frac{m_1 m_2}{M_{p(4+\delta)}^{\delta+2} R^{\delta}} \frac{1}{r}, \qquad (r \gg R)
\end{aligned}
\tag{2.43}
$$

where $M_{p(4+\delta)}$ is the true Planck scale of the $4+\delta$ dimensional theory and $M_{p(4+\delta)}^{\delta+2} R^{\delta}$ is to be identified with the effective Planck scale observed in 4 dimensions. In order to resolve the naturalness problem, the true Planck scale should be $\sim$ TeV. By requiring the the size of the extra dimensions reproduce the effective Planck mass for $\delta = 2$ should be $\sim$ 0.1–1mm. A conceptual problem arises with the original ADD model since there is no mechanism to set the size of the extra dimensions, leading to a different naturalness problem.

An alternate extra-dimensional scenario is the Randall-Sundrum model [74]. The model assumes a single extra spacetime dimension with the following metric:

$$
ds^2 = e^{-2kR\phi} \eta_{\mu\nu} dx^{\mu} dx^{\nu} + R^2 d\phi^2 \tag{2.44}
$$

where the k is a scale of the order of the Planck scale, x^{μ} are the 4-dimensional spacetime coordinates, while $0 \leq \phi \leq \pi$ is the coordinate of the compactified fifth dimension with size set by R. The new physics scale of a TeV is identified with $M_p e^{-kR\pi}$. In this case the hierarchy between the Planck scale and the compactification scale $1/R$ is only of the order of 10, instead of $(M_p/\text{TeV})^{2/\delta}$ as in the ADD model. An additional phenomenological feature of the RS model is that the gauge bosons can propagate in the fifth dimension, which leads to additional excitation modes of the W and Z bosons with mass of the first excitation $M_1 \sim M_p e^{-kR\pi} \sim$ TeV [75].

2.2.4 Little Higgs

Another possibility to resolve the naturalness problem is a class of theories referred to as "Little Higgs" models. These models were first proposed as models where the Higgs is a pseudo-Goldstone boson, similar to the pion, of an approximate global symmetry group which is broken at the TeV scale [76]. In Little Higgs models the symmetry is broken collectively, i.e. no single interaction breaks all of the symmetry. This precludes a mass term for the SM Higgs doublet and guarantees the cancellation of the quadratically divergences at one-loop the level [77]. The divergences arise at instead at the two-loop level, so that a Higgs mass at the 100 GeV scale is natural, and the cutoff scale Λ is pushed to ~ 10 TeV, above which additional new physics is required. This idea is attractive since many models which predict new physics at the TeV scale are already being severely constrained by precision measurements [78] and direct searches at the Tevatron and LHC.

Example models of Little Higgs theories are the "Littlest Higgs" [79] with a gauge symmetry $[\mathrm{SU}(2) \times \mathrm{U}(1)]^2$ and the "Simplest Little Higgs" [80] with a gauge symmetry $\mathrm{SU}(3) \times \mathrm{U}(1)_\mathrm{X}$. A general feature of Little Higgs models is the prediction of heavy top quark partners, as well as new heavy gauge bosons associated with the additional broken symmetries. These particles are predicted to be around the TeV scale.

2.2.5 Left-Right Symmetry

A final class of theories to be mentioned are so called "left-right" symmetric models [81–83]. These models are motivated not by the Higgs naturalness problem, but by the seemingly odd phenomena of parity violation in the weak interactions. The fact that parity is not violated by any of the other forces suggests that parity violation might arise from a broken symmetry [84] and that full parity symmetry between left and right handed fermions could be restored at a higher energy. The minimal left-right symmetric model is based on the gauge symmetry group $\mathrm{SU}(2)_L \times \mathrm{SU}(2)_R \times \mathrm{U}(1)_{B-L}$, where $\mathrm{SU}(2)_L$ is identified with the usual SM SU(2) symmetry and $\mathrm{SU}(2)_R$ is the right handed version which is a broken symmetry at low energies. In addition to the prediction of right-handed neutrinos, the broken SU(2) implies heavy gauge bosons which are right handed copies of the SM W and Z bosons.

One of the nicest features of left-right right symmetric models is that they provide an explanation for the extremely small left-handed neutrino masses [85]. The mass of the left-handed neutrino is related approximately to the mass of the electron and the mass of the heavy right-handed W boson in the following way:

$$M_{\nu_e} \simeq m_e^2/gM_{W_R} \tag{2.45}$$

Therefore if the mass of the right-handed W boson is $\sim$ 5 TeV, then the mass of the left-handed neutrino is $\sim$ 0.1 eV, which is well below the current bounds discussed in Sec. 1.2.2.

2.3 Heavy Gauge Bosons

As can be seen from the previous discussion, the existence of a new heavy gauge boson is a generic prediction of many extensions to the SM which attempt to answer some of its shortcomings. Additional heavy gauge bosons with spin=1 and charge=$\pm$1 are generically referred to as W$'$ bosons. Similar to the case of the SM, the W$'$ bosons arise from a spontaneously broken gauge symmetry. In contrast to the SM W boson, which only has left-handed fermionic couplings, the W$'$ bosons may have any combination of left-handed and right-handed couplings. Several constraints on the properties of W$'$ bosons can be derived from both indirect measurements and direct searches.

2.3.1 Indirect Constraints

Indirect constraints on the mass of W$'$ bosons can be derived from low energy observables which would be affected by their presence. These constraints depend strongly on the particular W$'$ model. In the case of the minimal left-right symmetric model, strong constraints can be derived from the neutral K-meson mass difference, $\Delta M_K = (M_{K_L} - M_{K_S})$. This constraint can be expressed in a numerical form, and by normalizing to the experimental value [86]:

$$\frac{\Delta M_K^{LR}}{\Delta M_K^{exp.}} = -\cos(\theta_d - \theta_s)\frac{|(V_R)_{cd}(V_R)^*_{cs}|}{|(V_L)_{cd}(V_L)^*_{cs}|}\left(\frac{2.4\text{TeV}}{M_{W_R}}\right)^2\left[1 - 0.07\ln\frac{2.4\text{TeV}}{M_{W_R}}\right] \tag{2.46}$$

where the phase $\theta_d - \theta_s \simeq 0, \pi$ and V_L, V_R are the left-handed (SM) and right-handed CKM matrices, respectively. By restricting the ratio of the the mass difference predicted the theoretical model and the experimental value to be ~ 1, the indirected limit M(W′)>2.4 TeV for W′ bosons with right handed couplings follows directly.

This constraints, however, can be slightly modified when taking into account effects of an additional heavy Higgs boson that also exists in the minimal left-right symmetric model. The constraints in the M_{W_R} vs M_H plane taking into account these effects is shown in Fig. 2.10.

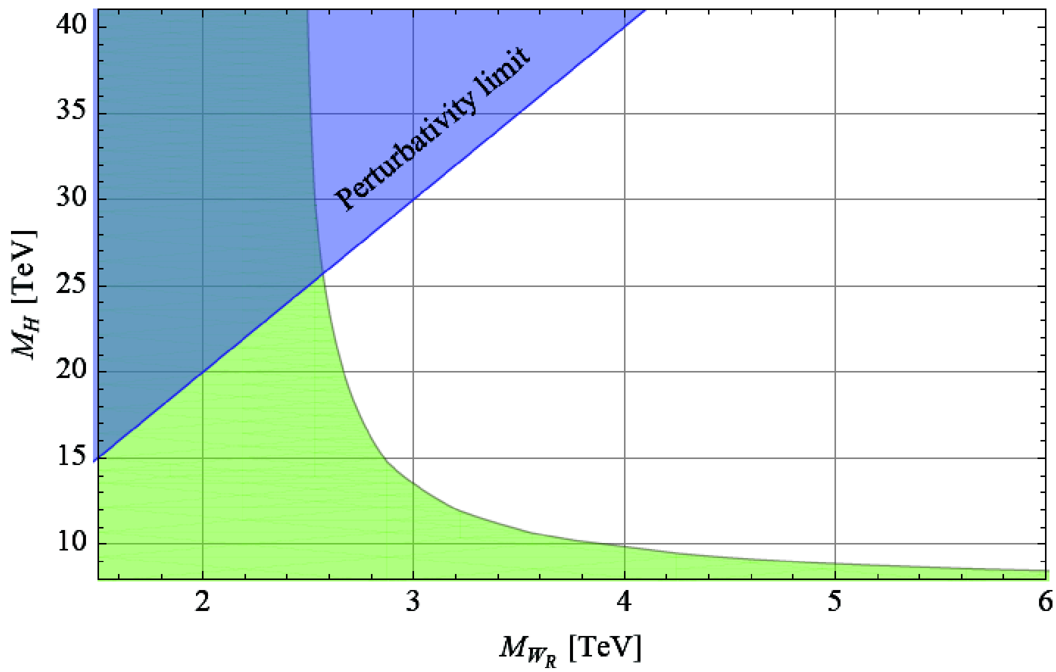

Figure 2.10: Limit on the heavy Higgs and W_R masses from ΔM_K, which excludes the shaded green zone. The perturbativity limit on the Higgs mass is also shown in blue. From Ref. [86].

In the case of Little Higgs models, the indirect constraints depend even more strongly on the model. In the case of the Littlest Higgs model [79], the heavy gauge bosons can contribute to SM observables such as the W-boson mass and the Z-boson decay width among many others [87]. These experimental values of these observables can then be used to set constraints, and in the Littlest Higgs model they require that the symmetry breaking scale be greater than 4-16 TeV, depending on other model parameters. This correlates very roughly to the mass of the heavy gauge bosons.

2.3.2 Direct Constraints

Since indirect constraints on the W′-boson masses vary strongly between each new particular physics model, direct searches at particle colliders, which have not yet produced any evidence for W′ production, tend to set constraints using a generic benchmark model. In this benchmark model, sometimes referred to as the sequential standard model (SSM), the W′ has the same couplings to fermions as the SM W boson. In the case of W′ bosons with right-handed couplings, the gauge coupling of the new $SU(2)_R$ symmetry is taken to be equal to the $SU(2)_L$ gauge couping, and the right-handed CKM matrix is taken to be equal to the left-handed CKM matrix. Limits on the production cross section in this model can be obtained by experiment and then reinterpreted in more realistic theoretical models.

The strongest direct constraints on W′-boson masses come from searches at the LHC, due to its high center of mass energy. The searches are performed using different decay modes of the W′ boson. In the benchmark SSM model the strongest constraints come from the $\mathrm{W}' \to \ell\nu$ decay mode, due to its low background rate. Exclusions in this channel from the CMS and ATLAS Collaborations can be seen in Fig. 2.11 [88, 89]. The results of these searches (and most other similar searches) are presented by showing the 95% confidence level limit on the W′-boson production cross section along with the predicted theoretical cross section, both as a function of the W′-boson mass. For W′-boson masses below the intersection of the theoretical cross section and the exclusion limit, the model can be excluded at 95% confidence level and the corresponding W′-boson mass value is quoted as the mass limit. Also shown are the nominal and $\pm 1\sigma$ expected exclusions obtained by performing pseudo-experiments with the signal and background estimations varied within their respective uncertainties. The CMS search in this particular channel is currently the most stringent, leading to the constraint $\mathrm{M(W')} > 2.90$ TeV for an SSM W′ boson.

Limits on W′-boson production can also be obtained using the $\mathrm{W}' \to \mathrm{q\bar{q}}$ decay mode where q is a light quark (udsc). The results of the searches by the CMS and ATLAS

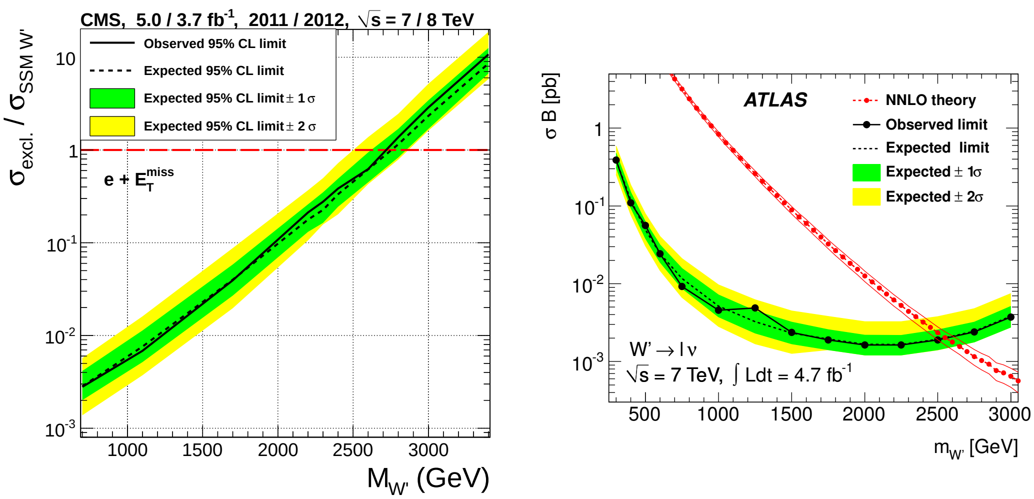

Figure 2.11: Constraints on W′ boson production using the W′ → $\ell\nu$ decay mode by the LHC experiments. Left: The CMS search from Ref. [88]. Plotted is the ratio $\sigma_{\mathrm{excl}}/\sigma_{\mathrm{SSMW}'}$ as a function of the W′ mass, where σ_{excl} is the cross section excluded at a 95% confidence level and $\sigma_{\mathrm{SSMW}'}$ is the cross section predicted by the SSM. Right: The ATLAS search from Ref. [89]. Plotted is the excluded cross section and theoretical cross section both as a function of the W′ mass.

Collaborations can be seen in Fig. 2.12 [90, 91]. The CMS search leads to the strongest mass limit in this channel for an SSM W′ boson: M(W′) > 1.73 TeV. The case where the W′ boson decays to third generation quarks (tb) will be discussed in detail in Chapter 6.

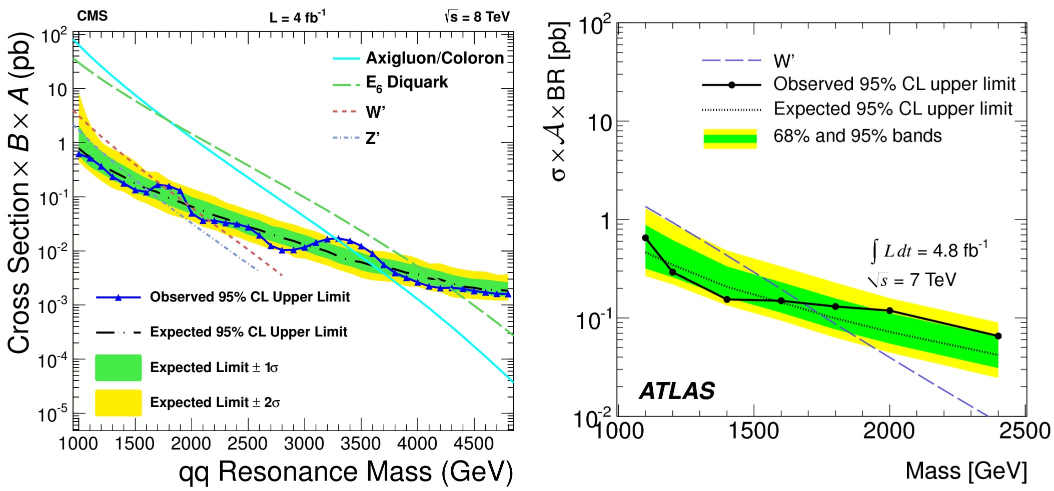

Figure 2.12: Constraints on W′ boson production using the W′ → q$\bar{\text{q}}$ decay mode by the LHC experiments. Left: The CMS search from Ref. [90]. Right: The ATLAS search from Ref. [91].

A final class of direct searches are for W′ bosons with purely right-handed couplings which decay to a right-handed lepton and heavy right-handed neutrino, a decay mode predicted within the left-right symmetric model. The heavy right-handed neutrino is unstable and subsequently decays to a right-handed lepton and virtual right-handed W′ boson, which then decays to two light quarks. This results in the decay chain $\text{W}' \to \ell_1\nu_\text{R} \to \ell_1\ell_2\text{W}'^* \to \ell_1\ell_2\text{qq}$, where N is the heavy right-handed neutrino. This decay is only allowed if $\text{M}(\nu_\text{R}) < \text{M}(\text{W}')$. Searches for this final state have been performed by the CMS and ATLAS Collaborations leading to a constraint $\text{M}(\text{W}') \gtrsim 2.5$ TeV, depending on $\text{M}(\nu_\text{R})$ [92, 93]. The constraints in the parameter space $\text{M}(\nu_\text{R})$ vs. $\text{M}(\text{W}')$ can be seen in Fig. 2.13.

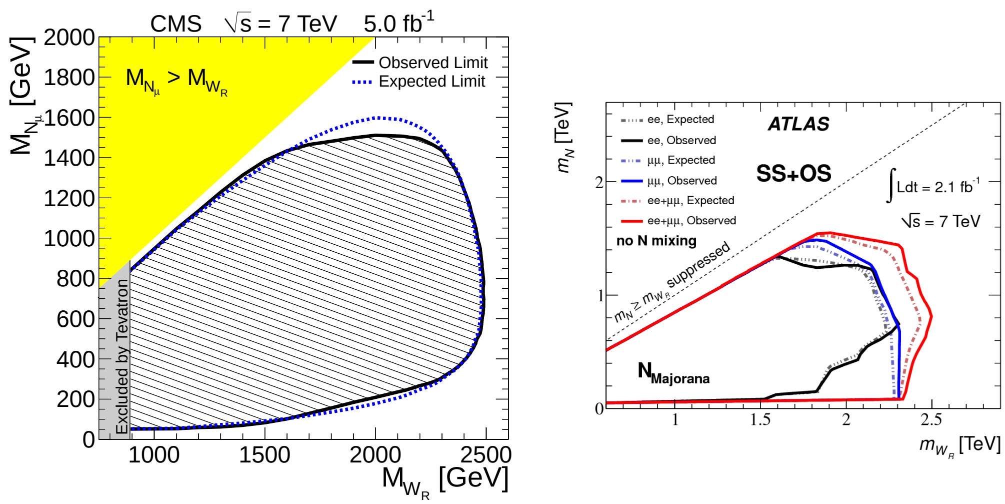

Figure 2.13: Constraints on right-handed W′ boson heavy right-handed neutrino masses using the $\mathrm{W}' \to \ell_1 N \to \ell_1 \ell_2 \mathrm{W}'^{*} \to \ell_1 \ell_2 \mathrm{qq}$ decay mode by the LHC experiments. Left: The CMS search from Ref. [92]. Right: The ATLAS search from Ref. [93].

Chapter 3

The Large Hadron Collider

The Large Hadron Collider (LHC) [94] is a two-ring-superconducting accelerator designed to accelerate protons to an energy of 7 TeV. The LHC then causes the proton beams to collide at several interaction points with a total center-of-mass energy of $\sqrt{s} = 14$ TeV and instantaneous luminosity of $10^{34}\text{cm}^{-2}\text{s}^{-1}$. The LHC is also designed to accelerate the nuclei of heavy elements such as lead to an energy of 2.76 TeV/nucleon. The LHC is housed within the 26.7 km underground tunnel constructed between 1984 and 1989 and previously used for the Large Electron-Positron (LEP) Collider [95]. Positioned around the ring at the four interaction points are five experiments with varying physics goals. The CMS and ATLAS experiments are general-purpose detectors designed to operate at high instantaneous luminosity. The LHCb experiment is designed to operate at lower luminosities and optimized to measure the properties of b-hadrons. The TOTEM experiment operates at the same interaction point as the CMS experiment and is designed to study the physics of elastic scattering at small angles. Finally, the ALICE experiment is optimized to explore the properties of heavy-ion collisions.

3.1 Machine Parameters and Design

A scattering process at the LHC is referred to as an event, and the number of events created per second for any scattering process is given by:

$$N_{\text{event}}/\text{sec.} = \sigma_{\text{event}} L \tag{3.1}$$

The production cross section (σ_{event}) for a certain type of event depends on the initial state particles and the center of mass energy of the collision; the instantaneous luminosity (L) depends entirely on the beam parameters. The total number of events produced is given by the time integral of Eqn. (3.1):

$$N_{\text{event}} = \sigma_{\text{event}} \int L dt \tag{3.2}$$

The second term on the right-hand side of Eqn. (3.2) is referred to as the integrated luminosity. The technologies used in the LHC are optimized to maximize the sensitivity to the cross sections of rare processes to be studied (usually without knowing key parameters such as the mass of a hypothetical particle), and also to minimize the overall cost of construction and operation.

3.1.1 Luminosity Constraints

For a Gaussian beam distribution, the instantaneous luminosity L of the machine can be written as:

$$L = \frac{N_b^2 n_b f_{rev} \gamma_r}{4\pi\epsilon_n\beta^*} F \tag{3.3}$$

where N_b is the number of particles (i.e. protons) per bunch, n_b is the number of bunches per beam, f_{rev} is the revolution frequency, γ_r is the relativistic gamma factor ($\gamma_r = E_p/m_p c^2$), ϵ_n is the normalized transverse beam emittance, and β^* is the beta function at the collision point. The geometrical factor F accounts for the reduction due to the small crossing angle at the interaction point. The term $\frac{4\pi\epsilon_n\beta^*}{F}$ can be thought of as the effective area of the beams.

The constraints on the beam parameters come from several sources. An important constraint comes from the non-linear beam-beam interactions experienced by particles within each bunch when the beams collide. The level of this interaction is measured by the linear tune shift ξ, which is expressed as:

$$\xi = \frac{N_b r_p}{4\pi\epsilon_n} \tag{3.4}$$

where $r_p = e^2/(4\pi\epsilon_0 m_p c^2)$ is the classical proton radius. The maximum value of ξ for safe operation has been learned through experience at previous hadron colliders, and should not exceed 0.015 when summed over all three high-luminosity interaction points. The maximum acceptable transverse emittance is determined from the geometrical aperture of the LHC beam screen, and the peak β-function in the LHC arcs, which imply $\epsilon_n = 3.75\mu$m. Furthermore, the beam intensity is limited by the amount of energy emitted by synchrotron radiation which must be absorbed by the cryogenic system. These considerations together imply a maximum bunch intensity of $N_b = 1.15 \times 10^{11}$. The beams consist of 3564 proton bunches with a minimum bunch-to-bunch distance of 25 ns, of which 2808 are filled with protons. The empty bunches are necessary to allow for the injection as well as the eventual beam dump. The 25 ns spacing determines the 40 MHz sampling frequency of the experiments.

3.1.2 Energy Constraints

The center-of-mass energy is constrained by the size of the tunnel and magnet technology. In order to keep the proton beams on path within the LHC beam pipe, the LHC uses magnets formed by coils of superconducting NbTi wire cooled to 1.9 K using superfluid helium. The magnets are used to create dipole (bending) and quadrupole (focusing) fields. Furthermore the total energy stored in the beam and the magnet system is greater than 1 GJ, which must be safely aborted in case of an emergency or a system malfunction. These considerations lead to a maximum beam energy of 7 TeV per beam. A cross section of the LHC cryodipole is shown in Fig. 3.1.

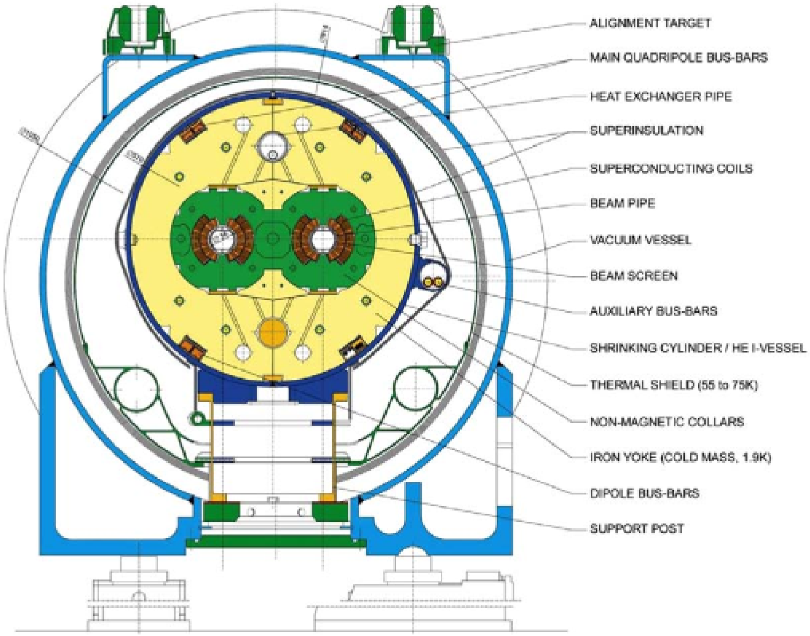

Figure 3.1: A cross section of the LHC cryodipole. From Ref. [94].

3.1.3 Injector Chain

Before reaching the final design energy of 7 TeV per beam within the LHC, the proton bunches must be accelerated through a series of increasingly energetic linear accelerators and storage rings known as the LHC injector chain [96], which consists of the Linac2, the Proton Synchrotron Booster (PSB), the Proton Synchrotron (PS) and the Super Proton Synchrotron (SPS). The protons are produced from hydrogen gas by stripping the electrons with a large electric field. The total hydrogen consumption is about 4 ml/min. The Linac2 creates the bunches and accelerates them to 50 MeV. The bunches are then injected to the PSB where they are accelerated to 1.4 GeV and then injected into the PS. In the PS the bunches are accelerated to 25 GeV before being injected into the SPS. The SPS is the final injection step before the LHC and accelerates the bunches to 450 GeV. A schematic of the CERN accelerator complex can be seen in Fig. 3.2 [97].

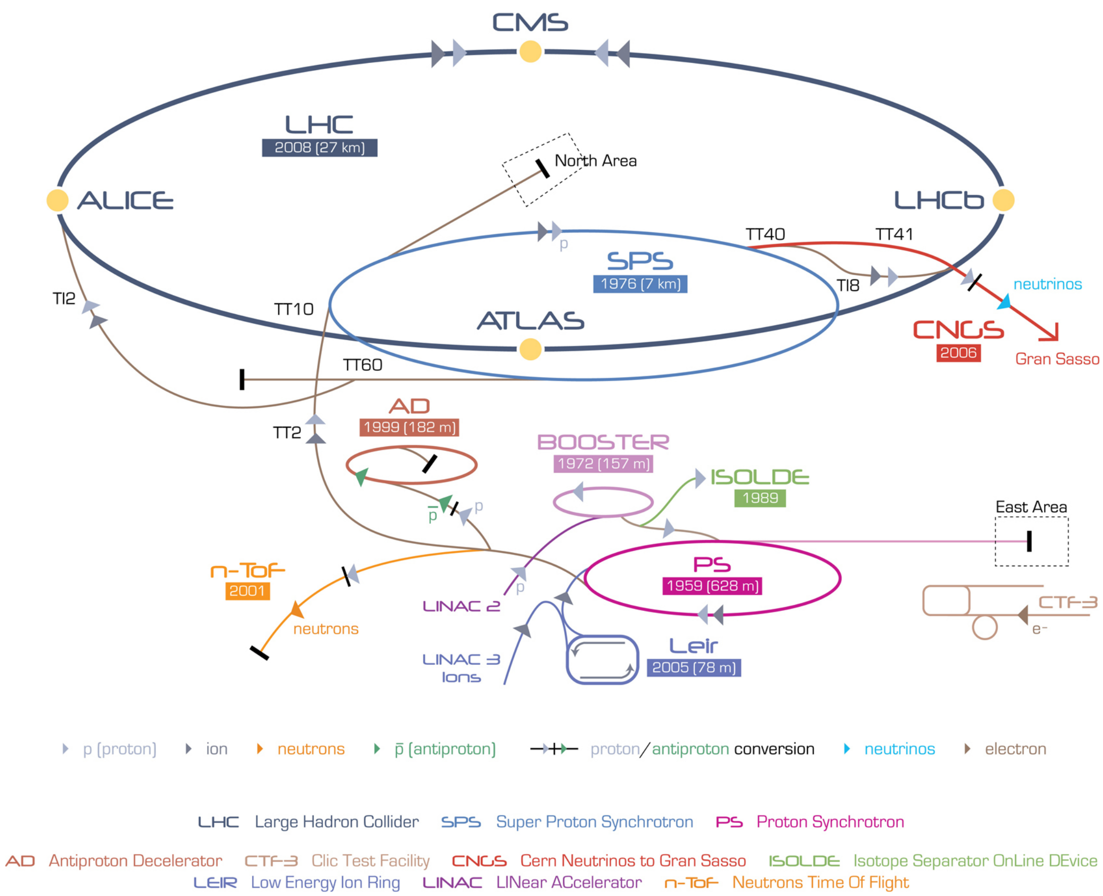

Figure 3.2: A schematic drawing of the CERN accelerator complex. From Ref. [97].

3.2 Performance

Due to mechanical damage resulting from an electrical fault during commissioning in September 2008 [98], the LHC has delivered pp collisions at a reduced center of mass energy of $\sqrt{s}$ = 7 TeV during 2010 and 2011, and of $\sqrt{s}$ = 8 TeV during 2012. Even while operating at these reduced energies, the LHC is still the highest-energy particle accelerator in the world. Furthermore, the bunch spacing was increased to 50 ns due to the effects of secondary electron emission from the from the beam chamber wall [99]. Consequently, the maximum number of bunches per beam, n_b, was reduced to 1374. As seen in Figs. 3.3 and 3.4, the peak instantaneous luminosity achieved was 7.67 $\times 10^{33}$cm^{-2}s^{-1} [100]. This luminosity, greater than half the design luminosity, was achieved with half the number of design bunches by operating at larger bunch intensity (N_b = 1.7 $\times 10^{11}$) and lower normalized emittance (ϵ_n = 2.5 μm) than the original design [101]. Subsequently the mean number of interactions per bunch crossing (pileup) for the experiments was also greater than foreseen, making for an incredibly challenging experimental program. A plot showing the average pileup seen during the 2012 data taking run can be seen in Fig. 3.5. In total the LHC delivered 6.13 fb^{-1} of pp collisions to the CMS experiment at $\sqrt{s}$ = 7 TeV during 2011, and 23.30 fb^{-1} at $\sqrt{s}$ = 8 TeV during 2012. The final integrated luminosity used for analysis after more sophisticated calibration of the luminosity measurement, as well as accounting for the data taking efficiency and removing data of insufficient quality, was 5.0 fb^{-1} at $\sqrt{s}$ = 7 TeV and 19.5 fb^{-1} at $\sqrt{s}$ = 8 TeV.

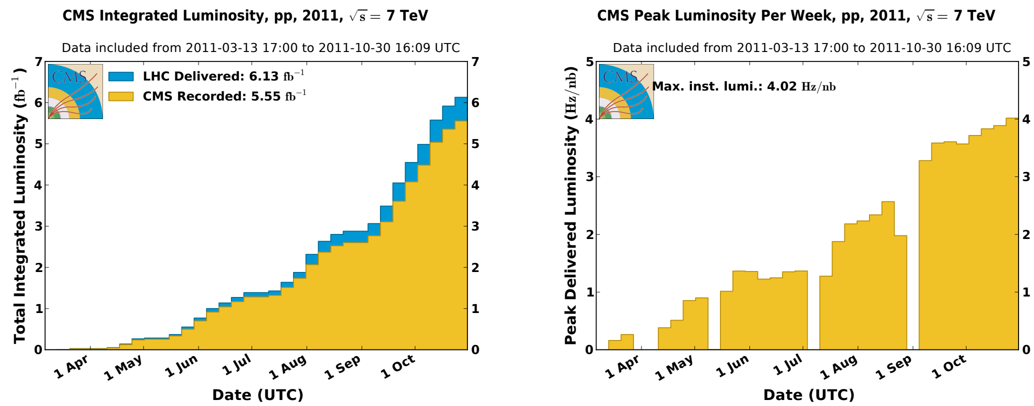

Figure 3.3: Integrated luminosity (left) and peak instantaneous luminosity (right) delivered by the LHC to the CMS experiment for each week during the 2011 run at $\sqrt{s} = 7$ TeV. From Ref. [100].

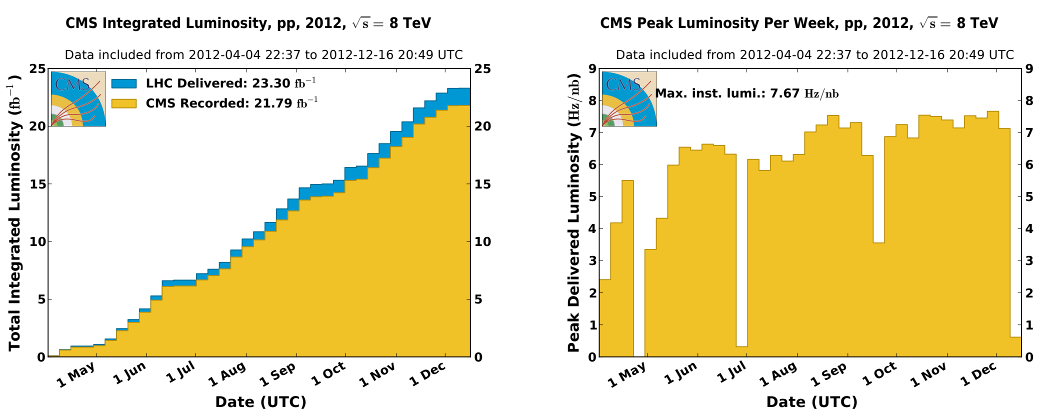

Figure 3.4: Integrated luminosity (left) and peak instantaneous luminosity (right) delivered by the LHC to the CMS experiment for each week during the 2012 run at $\sqrt{s} = 8$ TeV. From Ref. [100].

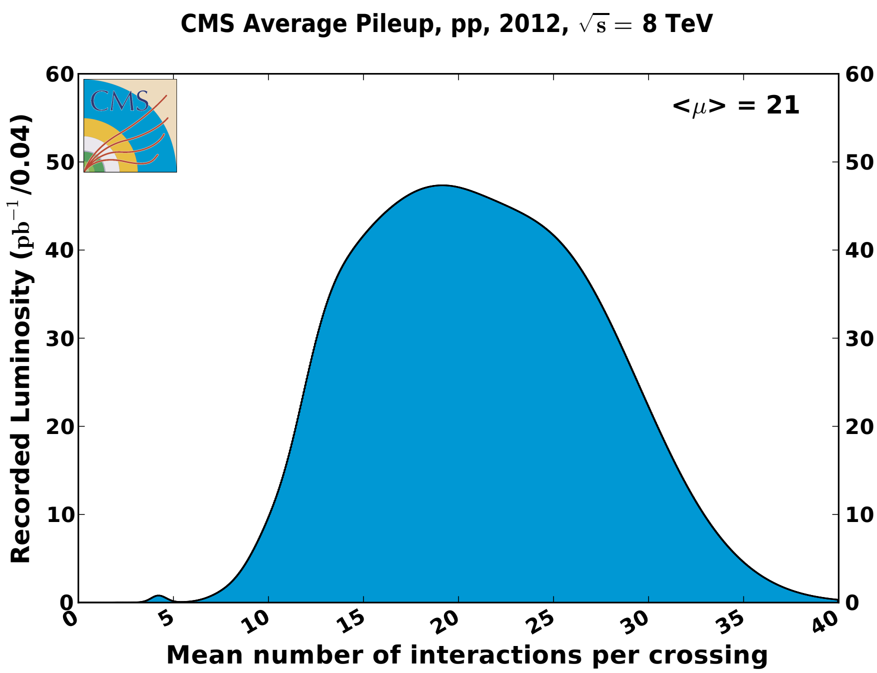

Figure 3.5: Mean number of interactions per bunch crossing during the 2012 data taking run at $\sqrt{s} = 8$ TeV as measured by the CMS experiment. From Ref. [100].

Chapter 4

The CMS Experiment

The Compact Muon Solenoid (CMS) experiment [102] is a 12,500 ton general-purpose particle detector situated at Point 5 of the LHC near the village of Cessy, France. The main goal of the CMS experiment is to reconstruct electrons, muons, photons, and hadrons (mesons or baryons) efficiently and with high resolution. This is accomplished by using a 3.8 T superconducting magnet to bend charged particles and measure their momentum via a silicon-based tracker. Electromagnetically interacting particles are further characterized by their interaction with an electromagnetic calorimeter (ECAL), and similarly strongly interacting particles are characterized by the hadronic calorimeter (HCAL). The identification of muons is performed by a separate muon system consisting of gaseous particle-detectors. Any neutrinos produced in the collision event are not directly detected, but can be inferred by measuring the total imbalance of all particle transverse momenta (p_{T}). Due to the high intensity and collision rate of the proton bunches provided by the LHC, the CMS experiment is finely segmented and therefore has a large number of readout channels. A drawing of the CMS detector can be see in Fig. 4.1 [103].

4.1 Geometry

The CMS experiment is roughly cylindrical in shape and has a 14.6-m diameter and 21.6-m length. The detector elements in the central “barrel” region are cylindrical, and the

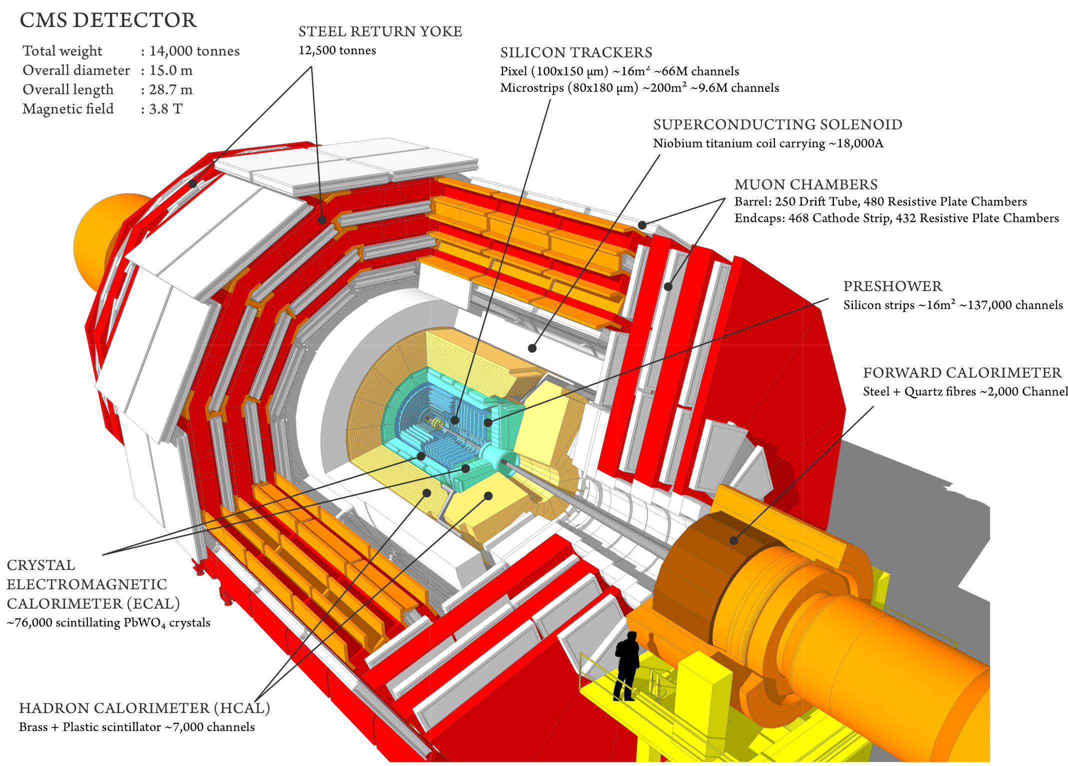

Figure 4.1: A perspective view of the CMS experiment. From Ref. [103].

two outer "endcap" regions are enclosed with disk-like elements. In general the barrel and endcap detectors utilize separate technologies. CMS uses a right-handed coordinate system, with the origin at the nominal collision point inside the experiment, the x axis pointing inward to the center of the LHC ring, the y axis pointing upward (perpendicular to the plane of the LHC ring), and the z axis along the anticlockwise-beam direction towards the Jura mountains, and the radial distance r measured outwards from origin. Thus the transverse components of particle momenta are in the x-y plane. The polar angle θ is measured from the positive z axis and the azimuthal angle ϕ is measured in the x-y plane. A convenient measure is the pseudorapidity defined as $\eta \equiv -\ln(\tan(\theta/2))$, for which particle production is roughly constant.

4.2 Superconducting Magnet

The central feature of the CMS experiment is a superconducting solenoidal magnet designed to produce a 3.8 T field in a free bore of 6-m diameter and 12.5-m length, large enough to enclose the tracker system, ECAL and HCAL. The high field strength is required in order to have good momentum resolution for tracks with p_{T} up to and above 1 TeV. The 220-t cold mass operates at 4.5 K and is defined by a 4-layer winding of NbTi conductor, and the flux is returned through a 10,000-t iron yoke comprising 5 wheels and 2 three-disk endcaps interspersed within the muon system (See Fig. 4.1).

4.3 CMS Subdetectors

4.3.1 Inner Tracker

The CMS inner tracking system is the closest subdetector to the interaction point and has an overall 5.8-meter length and 2.5-meter diameter. It is designed to efficiently and precisely measure the trajectories of charged particles with p_{T} greater than 1 GeV emerging from LHC collisions inside a 3.8T magnetic field. In addition to measuring individual particle trajectories, the system also must reconstruct the vertices of the primary interaction, the vertices of pileup collisions, and secondary vertices of long lived particles (such as b quarks and tau leptons) decaying away from the collision point. In order to cope with the large number of pileup interactions the detector must be radiation hard, have high granularity and a fast response, while keeping the amount of material used as small as possible to prevent multiple Coulomb scattering, bremsstrahlung, nuclear interactions, and photon conversions. Since the particle occupancy is largest near the interaction point and decreases with increasing radius, the tracking system utilizes two different types of silicon detectors at smaller and larger radius. A schematic drawing of the tracking system can be seen in Fig. 4.2.

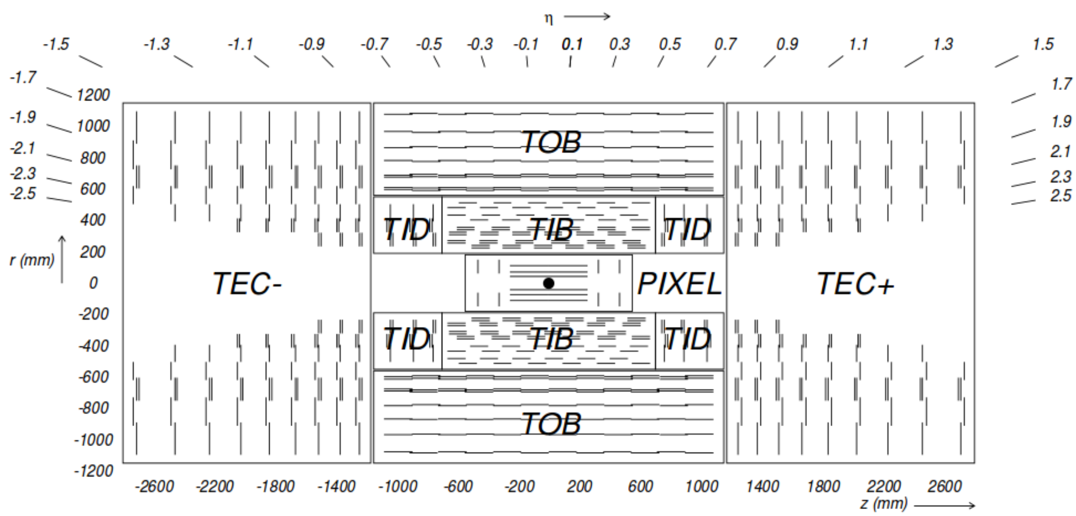

Figure 4.2: A schematic drawing of an $r-z$ slice of the CMS tracking system. From Ref. [102].

The innermost portions of the tracking system are silicon pixel detectors between radii of 4.2 cm and 10.2 cm. The pixel detector is composed of three barrel layers (BPix) two endcap disks (FPix), and has 1440 detector modules covering approximately 1m^2 for a total of 66 million pixels. The layout ensures three measurements over almost the full η-range of the tracker. The pixel detector provides three high precision space points in $r-\phi$ and z on each particle trajectory, with spatial resolution in the range of 15-20 μm. The pixel cell size of 100×150 μm^2 ensures similar resolution in the $r - \phi$ and z directions and therefore allows a 3D reconstruction of track vertices.

Outside of the pixel detector is the silicon strip tracker, which is composed of 4 Tracker Inner Barrel (TIB) layers, 6 Tracker Outer Barrel (TOB) layers, 3 Tracker Inner Disks (TID), and 18 Tracker EndCap (TEC) disks. Up to 4 $r - \phi$ measurements are delivered by the TIB/TID on a trajectory using 320-μm thick silicon micro-strip sensors with their strips parallel to the beam axis in the barrel and radial on the disks. The strip pitch is 80 μm on layers 1 and 2 and 120μm on layers 3 and 4 in the TIB, leading to a single point resolution of 23 μm and 35 μm, respectively. The modules in the first two layers and rings, respectively, of TIB, TID, and TOB as well as rings 1, 2, and 5 of the TECs carry a second micro-strip detector module which is mounted back-to-back with a stereo angle of 100 mrad in order to provide a measurement of the second co-ordinate (z in the barrel and r on the disks). This leads to a single point resolution of 23 μm and 530 μm in TIB and TOB, respectively, and varies with pitch in TID and TEC. The layout of the tracker ensures at least 9 hits (with at least 4 of them being two-dimensional measurements) in the silicon strip tracker in the range of $|\eta| < 2.4$.

The total amount of material for the CMS tracker in units of radiation lengths is shown in Fig. 4.3. It increases from 0.4 X_0 at $|\eta| \approx 0$ to about 1.8 X_0 at $|\eta| \approx 1.4$, before decreasing to about 1 X_0 at $|\eta| \approx 2.5$. As can be seen from Fig. 4.4, the resolution of the transverse impact parameter (distance of closest approach in the $r - \phi$ plane to a matched vertex) determination is less than 30 μm for tracks with p_{T} greater than 6 GeV [104]. The vertex reconstruction efficiency is shown in Fig. 4.5 and is measured to be close to 100% if the vertex contains more than 2 tracks with p_{T} greater 0.5 GeV.

4.3.2 ECAL

The electromagnetic calorimeter (ECAL) of CMS [105] is a hermetic homogeneous calorimeter made of 75848 lead tungstate ($PbWO_4$) crystals mounted in a central barrel part and two endcaps. The ECAL was designed to have high resolution in order to detect the two-

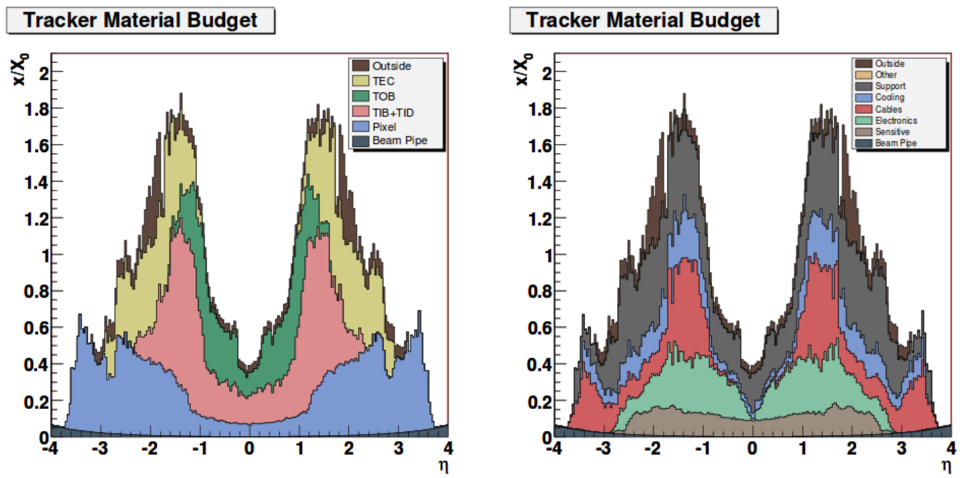

Figure 4.3: Material budget in units of radiation length as a function of pseudorapidity for the different tracking detectors (left) and for the functional contributions (right). From Ref. [102].

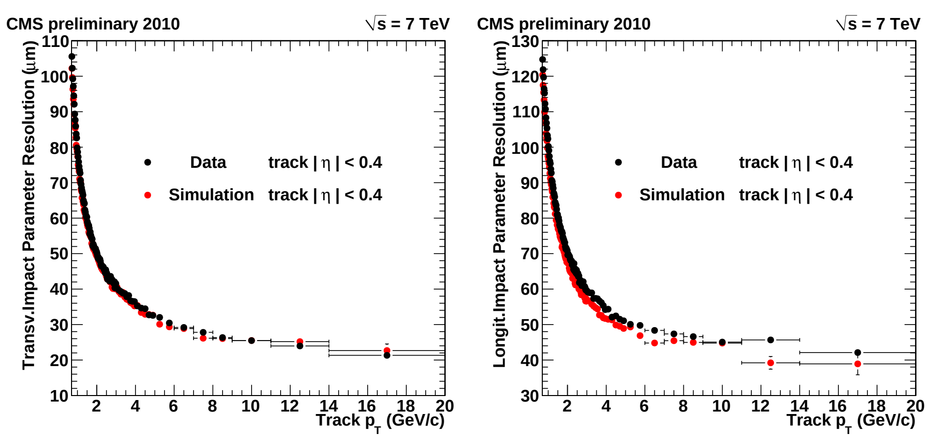

Figure 4.4: Measured resolution of the track transverse (left) and longitudinal (right) impact parameter as a function of the track p_{T} for tracks with $|\eta| < 0.4$. The results from 10.9 nb^{-1} of 7 TeV data are shown in black and the results from simulation are shown in red. From Ref. [104].

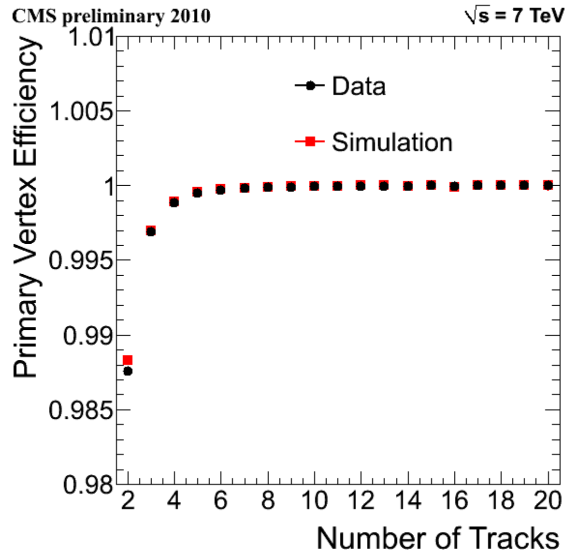

Figure 4.5: Primary vertex efficiency as a function of the number of tracks in a cluster. From Ref. [104].

photon decay of a Higgs boson, therefore it was decided to position the ECAL inside of the CMS magnet to reduce the amount of energy loss in non-instrumented material. Thus the ECAL must be compact, which led to the choice of $PbWO_4$ which has a high density (8.28 g/cm^3), a short radiation length (0.89 cm) and small Molière radius (2.2 cm). Furthermore the scintillation decay time of these crystals is of the same order of magnitude as the LHC bunch crossing time: about 80% of the light is emitted in 25 ns. The system is required to extract the heat dissipated by the read-out electronics to preserve energy resolution, and is therefore cooled by water flow to operate at a temperature of 18°C ± 0.05°C. A layout of the ECAL can be seen in Fig. 4.6.

The ECAL central barrel (EB) covers the range $|\eta| < 1.4442$ and is composed of 36 supermodules each containing 1700 tapered $PbWO_4$ crystals. Each crystal has a frontal area of approximately 2.2×2.2 cm^2 and a length of 23 cm, which corresponds to 25.8 radiation lengths. Two Hamamatsu S8148 5×5 mm^2 avalanche photodiodes (APDs)detect scintillation light from the crystals. The APDs are connected in parallel to the on-detector readout electronics, which are organized in units of 5×5 crystals to be used for triggering. The

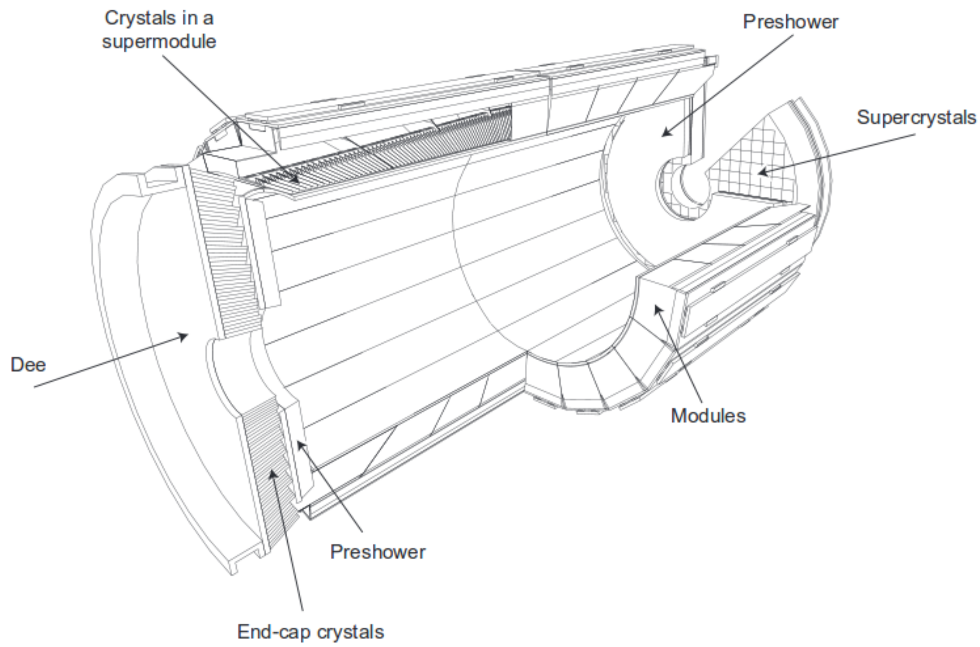

Figure 4.6: A schematic drawing of the CMS ECAL. From Ref. [102].

crystals are contained in a thin-walled structure known as a submodule. The submodules are assembled into modules of different types, according to the position in η, each containing 400 or 500 crystals. Four modules, separated by aluminum conical webs 4-mm thick, are assembled into a supermodule.

The two ECAL endcaps (EE) cover the range $1.556 < |\eta| < 3.0$ and are composed of 5 half-disk dees, each consisting of 3662 tapered crystals. The EE crystals have a frontal area of 2.68×2.68 cm^2 and a length of 22 cm (corresponding to 24.7 radiation lengths). The crystals in each dee are organized into 138 standard 5×5 supercrystal units, and 18 special shaped supercrystals that are located at the inner and outer radii. Scintillation light is detected by type PMT188 vacuum phototriodes (VPTs) glued to the rear face of the crystals. The lower quantum efficiency and internal gain of the vacuum phototriodes, compared to the avalanche photodiodes, is offset by their larger surface coverage on the back face of the crystals.

The ECAL preshower detector is a sampling calorimeter, and is designed to distinguish neutral pions from real photons and improves the position measurement of electrons and photons with high granularity. The preshower is built in two layers, the first of which is a lead absorber and the second of which is a silicon strip sensor which measures the deposited energy.

The resolution of the ECAL depends on whether the electron or photon undergoes bremsstrahlung, the transverse momentum, and also on η. CMS uses the following terminology to categorize electrons:

- G1: Bremsstrahlung energy is fully recovered.
- G2: Bremsstrahlung energy is not fully recovered due to photon conversions.
- EB: Electron is in the ECAL barrel.
- EE: Electron is in the ECAL endcap.

As shown in Fig. 4.7, the di-electron mass resolution at the J/Ψ and Z-boson resonances is less than 4% for the worst categories, and better than 1.5% for the best category [106]. The single electron reconstruction efficiency can be seen in Figs. 4.8 and 4.9, and is nearly 90% in EB and greater than 75% in EE.

4.3.3 HCAL

The CMS hadron calorimeter (HCAL) is used for the measurement of hadron jets as well as to infer the presence of neutrinos or exotic particles which result in an imbalance of transverse energy. A schematic drawing of the HCAL can be seen in Fig. 4.10. The HCAL is divided into the HCAL Barrel (HB) and HCAL Endcap (HE). Like the ECAL, the HCAL is mainly situated within the CMS magnet coil for better energy resolution. However the amount of material needed to absorb the hadron shower is greater than the available volume, therefore an additional outer HCAL (HO) is placed outside of the solenoid. Beyond $|\eta| = 3.0$, the forward hadron calorimeters (HF) placed at 11.2 m from the interaction point

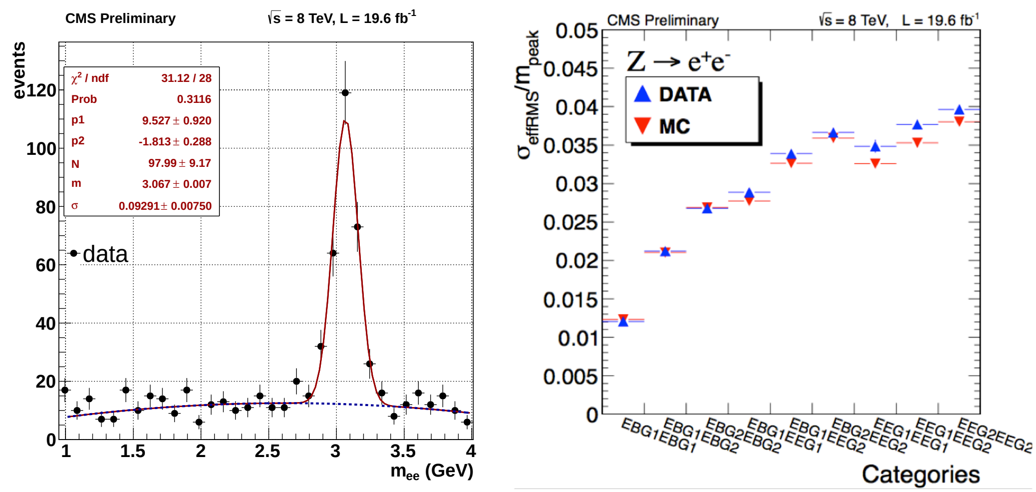

Figure 4.7: Left: $J/\Psi \rightarrow e^+e^-$ reconstructed in the barrel with one electron with $7 < p_T < 10$ GeV. Right: Instrumental di-electron mass resolution as measured from Z$\rightarrow e^+e^-$ events and compared to simulation. See text for the definitions of the categories. From Ref. [106].

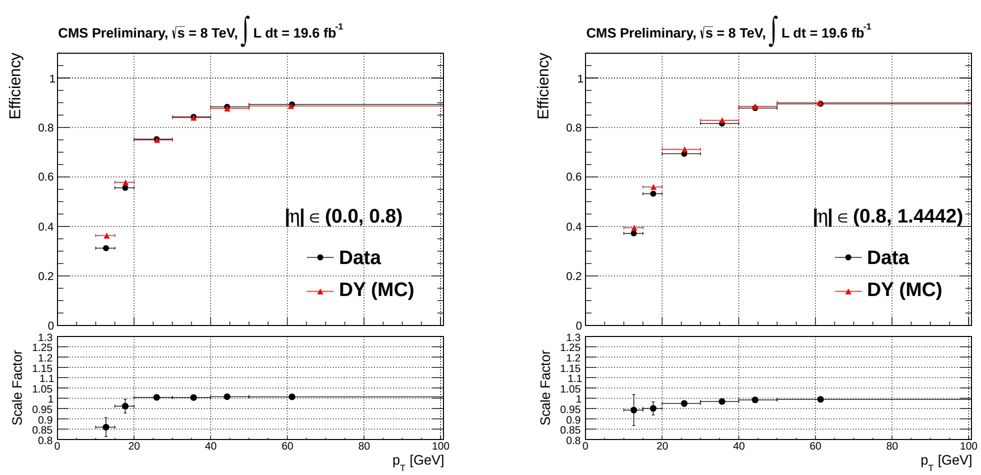

Figure 4.8: Electron selection efficiency for the medium working point on data and on a Drell-Yan Monte Carlo simulation sample as a function of the electron p_T , only statistical errors are shown. The bottom panel shows the ratio between data and simulation with statistical and systematic errors included. Left: Electrons in $0 < |\eta| < 0.8$. Right: Electrons in $0.8 < |\eta| < 1.4442$. From Ref. [106].

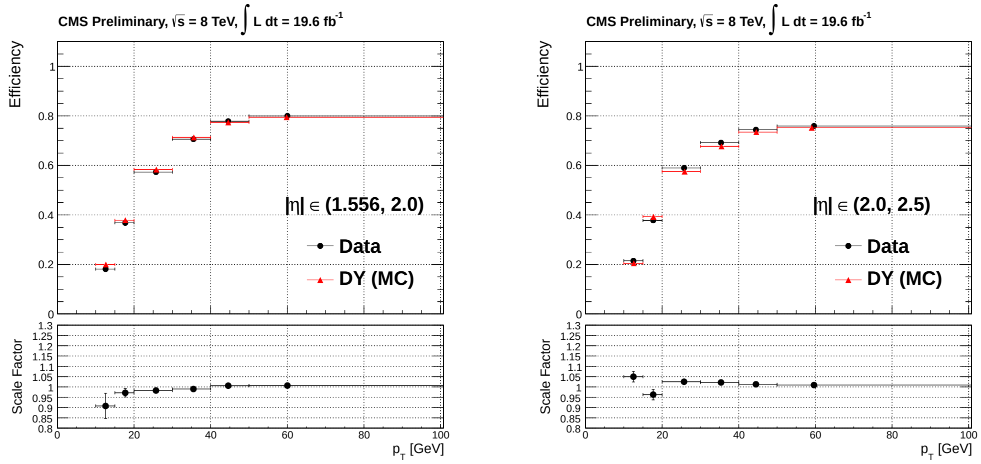

Figure 4.9: Electron selection efficiency for the medium working point which is designed to be approximately 80% efficient on data and on a Drell-Yan Monte Carlo simulation sample as a function of the electron p_{T} . Only statistical errors are shown. The bottom panel shows the ratio between data and simulation with statistical and systematic errors included. Left: Electrons in $1.556 < |\eta| < 2.0$. Right: Electrons in $2.0 < |\eta| < 2.5$. From Ref. [106].

extend the pseudorapidity coverage to $|\eta| = 5.2$ using a Cherenkov-based, radiation-hard technology.

The HB is a sampling calorimeter covering the pseudorapidity range $|\eta| < 1.3$. The HB is divided into two half-barrel sections (HB+ and HB-), which consist of 36 identical azimuthal wedges, and each wedge is further segmented into four azimuthal sectors. The absorbing material in a wedge consists of a 40-mm-thick front steel plate, followed by eight 50.5-mm-thick brass plates, six 56.5-mm-thick brass plates, and a 75-mm-thick steel back plate. The total absorber thickness at 90° is 5.82 interaction lengths (λ_{I}). The HB effective thickness increases with polar angle as $1/\sin\theta$, resulting in 10.6 λ_{I} at $|\eta| = 1.3$. The electromagnetic crystal calorimeter in front of HB adds about 1.1 λ_{I} of material. The active medium in each wedge consists of one layer of 9-mm-thick Bicron BC408 plastic scintillator, 15 layers of 3.7-mm-thick Kuraray SCSN81 plastic scintillator, and one layer of 9-mm-thich Kuraray SCSN81 plastic scintillator. The scintillation light is collected with a 0.94-mm-diameter green double-cladded wavelength-shifting fiber (KurarayY-11) placed in a machined groove

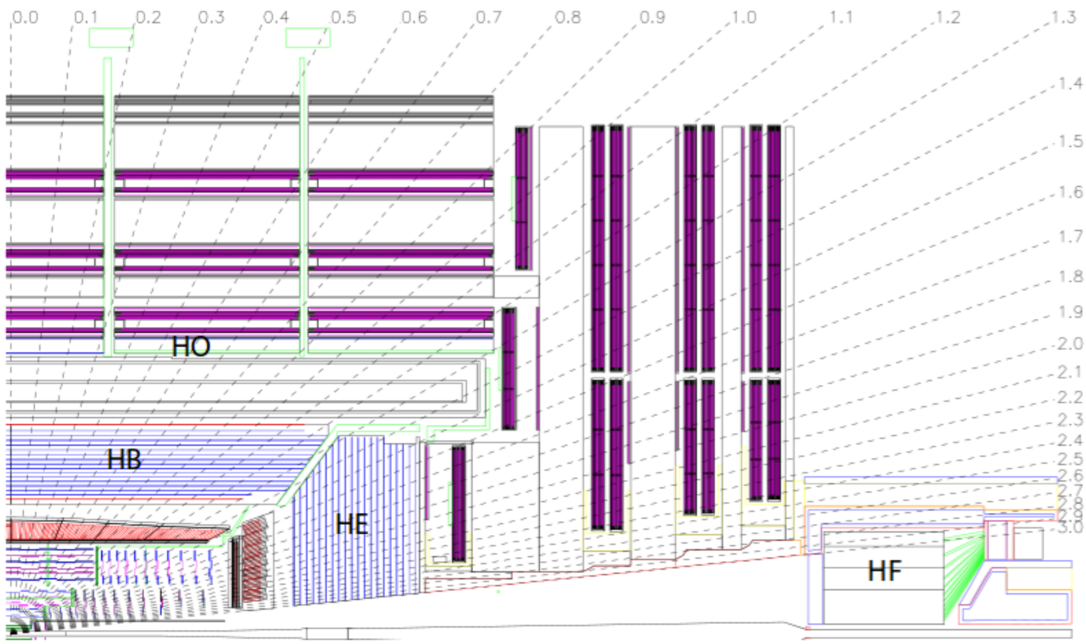

Figure 4.10: A schematic drawing of the CMS HCAL in the $r-z$ plane. The dashed lines denote different values of pseudorapidity. From Ref. [102].

in the scintillator.

The HE covers the pseudorapidity range $1.3 < |\eta| < 3.0$, and consists of an absorber material made of C62000 cartridge brass. The absorber geometry is chosen to minimize the cracks between HB and HE, since the jet energy resolution is limited by magnetic field effects, pileup and parton fragmentation. The brass plates are 79-mm-thick with 9-mm gaps to accommodate the scintillators, and the total length of the calorimeter, including electromagnetic crystals, is about 10 λ_{I}. The granularity of the calorimeters is $\Delta\eta \times \Delta\phi = 0.087\times0.087$ for for $|\eta| < 1.6$ and $\Delta\eta \times \Delta\phi = 0.17\times0.15$ for $|\eta| \geq 1.6$.

The HO ensures adequate sampling depth for $|\eta| < 1.3$. The central ring (ring 0) has two layers of HO scintillators on either side of a 19.5 cm thick piece of iron (the tail catcher iron) at radial distances of 3.82 m and 4.07 m, respectively. All other rings have a single HO layer at a radial distance of 4.07 m. The HO extends the total depth of the calorimeter system to a minimum of 11.8 λ_{I} except at the barrel-endcap boundary region. Scintillator tiles are made from Bicron BC408 scintillator plates of thickness 10^{+0}_{-1}mm and the scintillation light is read out by wavelength shifting fibers.

The HF calorimeter was designed to survive the high radiation environment of the very forward region $3.0 < |\eta| < 5.0$. This requirement led to the choice of quartz fibers as the active medium. The calorimeter consists of a steel absorber structure that is composed of 5 mm thick grooved plates into which the fibers are inserted. The depth of the absorber is 165 cm ($\approx 10\lambda_{\mathrm{I}}$). The fibers run parallel to the beam line, and are bundled to form 0.175 $\times$ 0.175 ($\Delta\eta \times \Delta\phi$) towers.

The uncertainty in the overall Jet Energy Scale (JES) achieved with the CMS calorimetry system can be seen in Figs. 4.11 and 4.12 [107]. The uncertainty is $< 4\%$ for jets with $p_{\mathrm{T}} = 30$ GeV around $|\eta| = 0$, decreases with increasing p_{T} until about 250 GeV before increasing slightly. The uncertainty also increases with increasing $|\eta|$. The resolution of the missing energy determination can be seen in Fig. 4.13 [108].

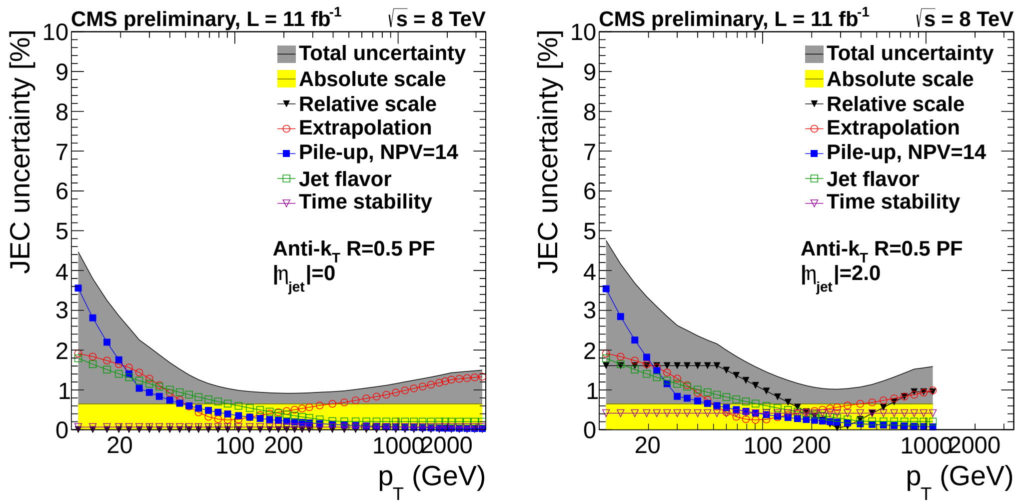

Figure 4.11: Jet energy correction uncertainties as a function of jet transverse momentum for jets reconstructed around $|\eta| = 0$ (left) and $|\eta| = 2.0$ (right). Different contributions are shown with markers of different colors, and the total uncertainty is shown with a grey band. From Ref. [107].

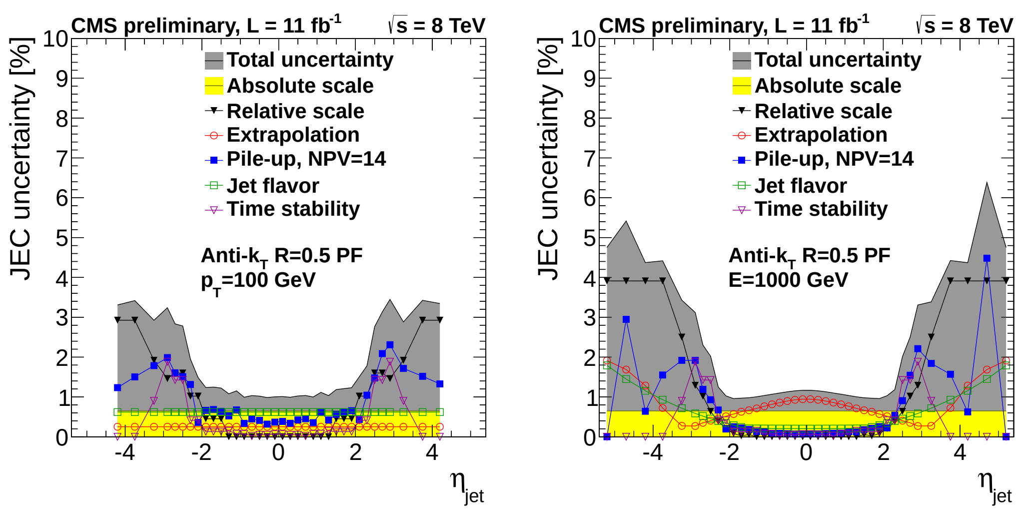

Figure 4.12: Jet energy correction uncertainties as a function of jet pseudorapidity for jets with transverse momentum equal to 100 GeV (left) and 1000 GeV (right). Different contributions are shown with markers of different colors, and the total uncertainty is shown with a grey band. From Ref. [107].

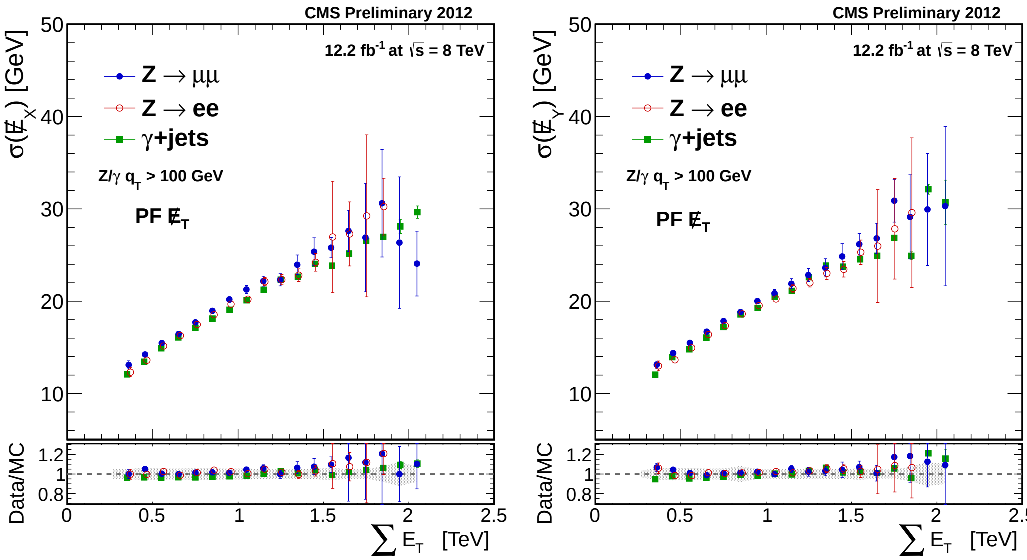

Figure 4.13: Resolution of the PF MET projection along the x-axis (left) and the y-axis (right) as a function of ΣE_T for events with Z boson or a photon. Results are shown for Z→ $\mu\mu$ events (full blue circles), Z→ ee events (open red circles), and photon events (full green squares). From Ref. [108].

4.3.4 Muon System

The CMS muon system is designed to measure the trajectory of muons over the largest possible portion of the kinematic range provided by the LHC. The long lifetime of the muon and the absorption of hadrons by the calorimeters leads to the positioning of the muon system as the outermost subdetector providing excellent identification capability. Like other detectors the muon system has a cylindrical shape, consisting of a barrel section and 2 planar endcap regions. The high-field solenoidal magnet and its flux-return yoke enable good muon momentum resolution and trigger capability. The latter also serves as a hadron absorber for better identification of muons. Three types of gaseous particle detectors are used for muon identification.

The barrel muon system covers the pseudorapidity region $|\eta| < 1.2$. Due to the small neutron-induced background, the low muon rate, and the uniform magnetic field, drift tube chambers (DTs) with rectangular drift cells are used. The DTs are organized into 4 stations interspersed among the layers of the magnet flux return plates. The first 3 stations each contain 8 chambers, in 2 groups of 4, which measure the muon coordinate in the $r - \phi$ bending plane, and 4 chambers which provide a measurement in the z-direction, along the beam line. The fourth station does not contain the z-measuring planes. A schematic drawing of the DT system can be seen in 4.14.

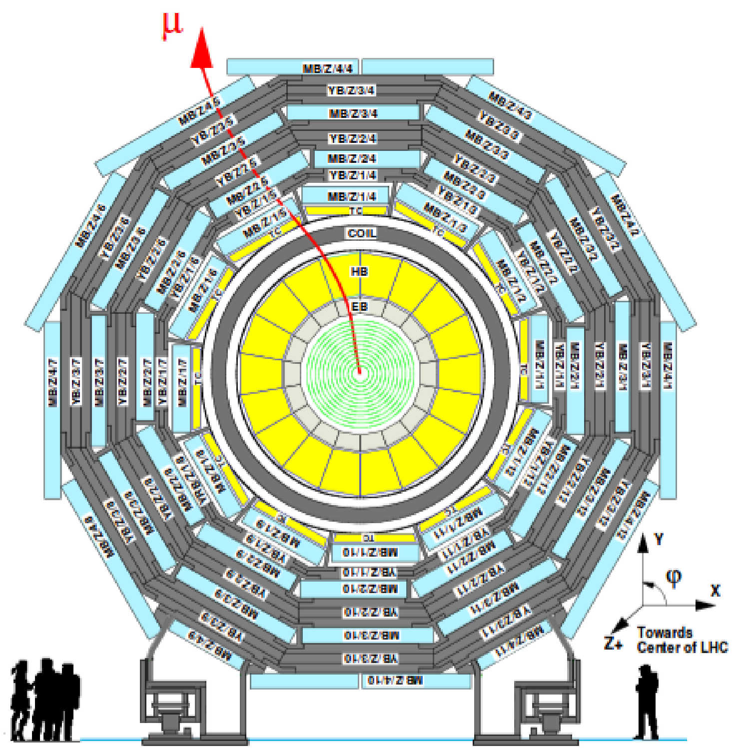

Figure 4.14: A schematic drawing of the CMS barrel muon DT chambers in one of the 5 wheels. From Ref. [102].

The endcap muon system covers the psuedorapidity range $0.9 < |\eta| < 2.4$. The system is instrumented with 468 multiwire proportional cathode strip chambers (CSCs) consisting of 6 anode wire planes interleaved among 7 cathode panels. The anode wires run azimuthally and define a track's radial coordinate. Strips are milled on cathode panels and run lengthwise at constant $\Delta\phi$ width. The muon coordinate along the wires is obtained by interpolating charges induced on strips. The CSCs can operate at high rates and in large and non-uniform magnetic fields. A muon in the pseudorapidity range $1.2 < |\eta| < 2.4$ crosses 3 or 4 CSCs. In the endcap-barrel overlap range, $0.9 < |\eta| < 1.2$, muons are detected by both the barrel drift tubes (DT) and endcap CSCs. A schematic drawing showing the grouping of the CSCs can be seen in 4.15.

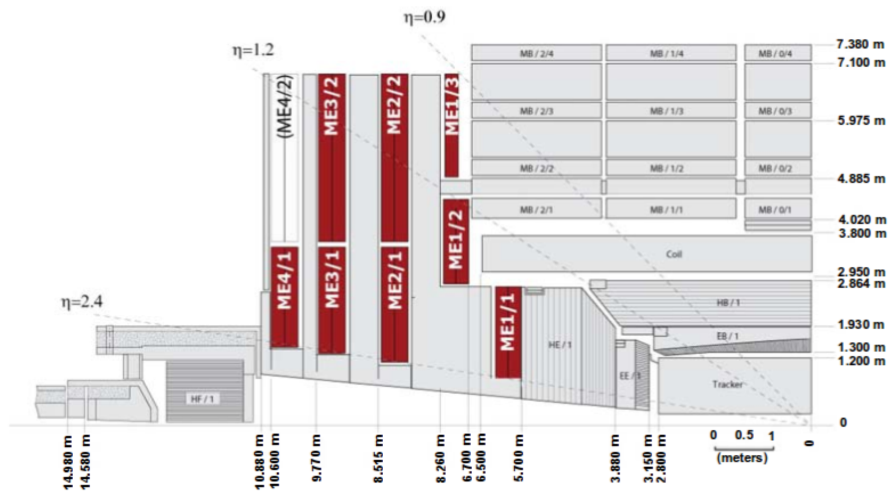

Figure 4.15: Quarter-view of the CMS detector with CSCs of the endcap muon system highlighted in red. From Ref. [102].

The CMS muon system is complemented in the psuedorapidity region $|\eta| < 1.6$ with Resistive Plate Chambers (RPCs), which are gaseous parallel-plate detectors that combine adequate spatial resolution with a time resolution capable of tagging the time of an ionizing event in a much shorter time than the 25 ns between 2 consecutive LHC bunch crossings (BX). Therefore, the muon system with RPCs can identify unambiguously the BX to which a muon track is associated. Furthermore the RPCs can be used to effectively tag backgrounds from cosmic rays, which are usually out of time with respect to the LHC BX. In the barrel iron yoke, the 480 rectangular RPC chambers form 6 coaxial sensitive cylinders around the beam axis and are arranged into 4 stations. In the endcap system they are mounted on both faces of the disks to yield 3 RPC stations. The double-gaps in each station have a trapezoidal shape and are arranged in 3 concentric rings.

The muon identification efficiency as measured from Z$\rightarrow$ $\mu^+\mu^-$ events can be seen in Fig. 4.16 [109]. The identification efficiency is greater than 92% for nearly the entire pseudorapidity range, and is not dependent on the muon p_{T} .

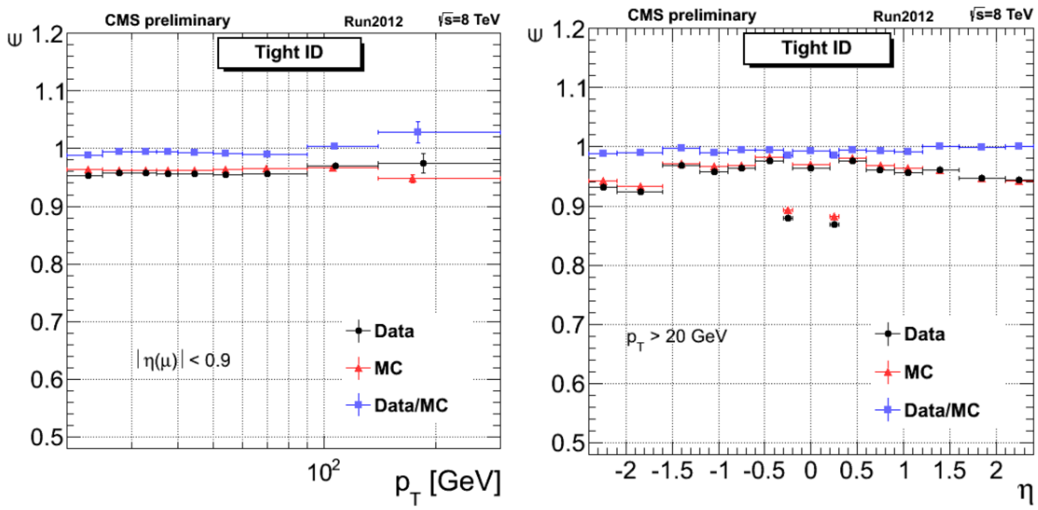

Figure 4.16: Efficiency for muons to pass the tight working point identification from $Z \rightarrow \mu^{+}\mu^{-}$ events. The measurement from data is in black, the measurement from simulation in red, and their ratio is in blue. The inefficient region $0.2 < |\eta| < 0.3$ is due to cracks between DT wheels 0 and ±1. From Ref. [109].

Chapter 5

The CMS Trigger and Data Acquisition Systems

The CMS trigger and data acquisition system [110, 111] is designed to quickly select the most interesting LHC collision events and write them to tape for further analysis. At an instantaneous luminosity of $L = 8 \times 10^{33}\text{cm}^{-2}\text{s}^{-1}$, the proton-proton collision rate is equal to 5×10^{8} Hz [112]. Due to the high granularity of the CMS detector, the data volume for each event is quite large. Furthermore, the data recorded must be promptly reconstructed for physics analysis to maintain the potential to spot new physics. Therefore, the event rate must be reduced by more than 6 orders of magnitude to achieve a manageable average rate of ≈ 300 Hz. This task is complicated by the fact that the processes of interest have a cross section several orders of magnitude lower than the background processes, meaning that the processes of interest must also be selected efficiently. The CMS experiment accomplishes this reduction in two successive stages. The first stage is based on custom electronics and is known as the Level-1 (L1) trigger. The L1 trigger uses coarse detector information to make a decision on whether to store or reject an event with a decision making time (or latency) of $\approx 3\ \mu$s. The L1 trigger has a maximum bandwidth of 100 kHz. The second stage is known as the High-Level Trigger (HLT) [113]. The HLT consists of more sophisticated reconstruction algorithms (including tracking) running on commercial processing units (CPUs). The HLT operates with a latency of ≈ 100 ms and produces a final output rate of ≈ 300 Hz of physics events, plus an additional allotment for monitoring and calibration. The HLT is part of the complete Data Acquisition System (DAQ) which manages the overall flow of data. Besides the HLT, the DAQ also consists of detector front-end electronics, readout modules, a builder network, as well as management and monitoring systems. A schematic drawing of the CMS trigger system can be seen in Fig. 5.1.

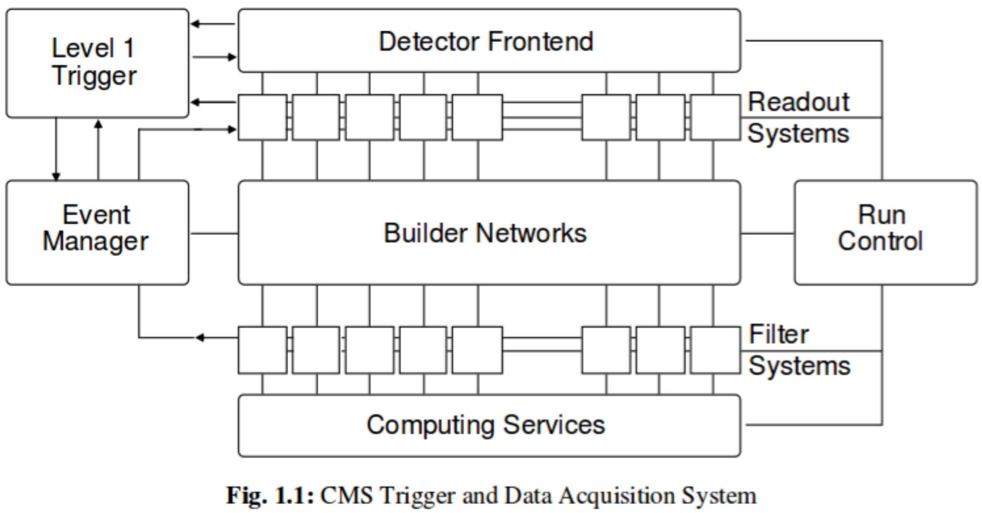

Figure 5.1: A schematic overview of the CMS trigger system. From Ref. [110].

5.1 The L1 Trigger

5.1.1 Constraints

The CMS L1 trigger is based on the identification of muons, electrons, photons, jets, and missing transverse energy. The trigger must have high efficiency and low thresholds to provide high statistics for a wide variety of measurements and searches. The L1 decisions are therefore mostly based on local detector information rather than on global topologies, except in the cases of missing energy and total energy sums. The L1 decision is made on a subset of the total information available for the events at a fixed time after the interaction has occurred every 25 ns. The L1 trigger system must be able to examine a new event every 25 ns in order to avoid having to discard events without having made any trigger decision (data-taking dead time). The 100 kHz maximum output rate of the L1 system is determined by the bandwidth of the readout system and the event builder, as well as the HLT event processing time.

The large volume of tracker and preshower data requires an architecture which can store event data before an L1 accept decision is made and the event is read out. This architecture prevents use of the tracker data in the L1 trigger decisions. The L1 decisions are therefore based entirely upon the calorimeter and muons systems. The L1 trigger subsystems are referred to as the Global Calorimeter Trigger (GCT) and the Global Muon Trigger (GMT). The combined information from these two systems is forwarded to the Global Trigger (GT) for the accept/reject decision. A schematic overview of the L1 trigger can be seen in Fig. 5.2.

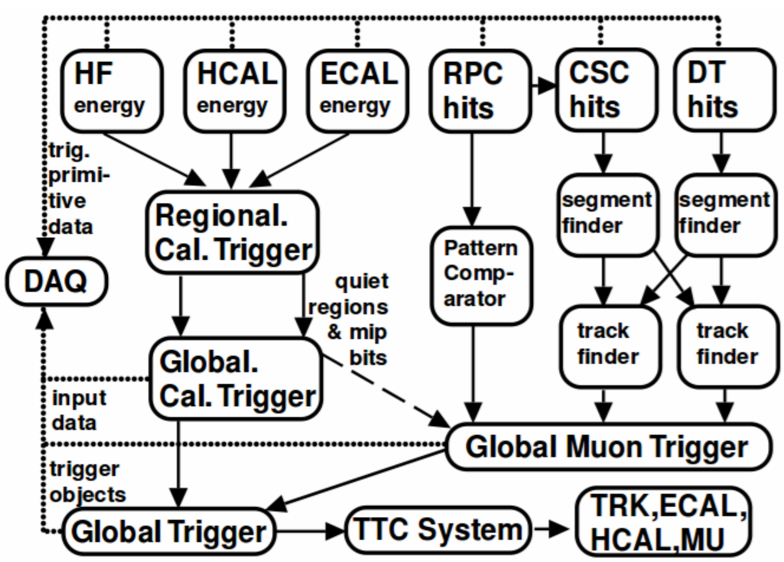

Figure 5.2: A schematic overview of the CMS L1 trigger system. From Ref. [110].

5.1.2 L1 Calorimeter Trigger

Energy deposits in the ECAL and HCAL are calculated in trigger towers that are sent over high speed copper links to the Regional Calorimeter Trigger (RCT), where e/γ candidates are identified. The GCT receives the e/γ candidates and regional energy sums which are used in the calculation of jets. Four isolated and four non-isolated e/γ candidates are then sent to the GT, along with four jet candidates in each of the following categories: central, forward and tau. The GCT also sends total and missing E_T sums as well as an (η, ϕ) grid of quiet regions to the global muon trigger for muon isolation cuts.

The efficiency the single e/γ trigger with a threshold of 20 GeV is shown in Fig. 5.3 (left) as a function of offline electron E_T. The efficiency is greater than 95% at 30 GeV and is approximately 100% efficient at 40 GeV for electrons in the ECAL barrel, and only slightly worse for electrons in the ECAL endcap. In 2012, corrections were applied to account for transparency losses in the ECAL endcap crystals, which improved the steepness of the efficiency turn-on relative to that in 2011. Fig. 5.3 right shows the jet trigger efficiency as a function of offline jet E_T for several online thresholds.

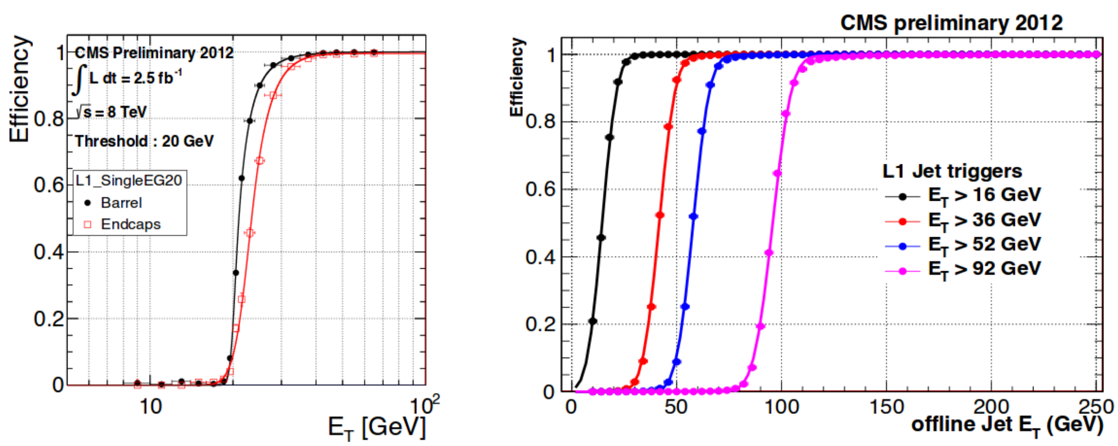

Figure 5.3: Efficiency of the L1 single e/γ trigger (left) and the L1 single jet trigger (right). From Ref. [112].

5.1.3 L1 Muon Trigger

Candidate muons in the L1 trigger system are identified separately in each of the DT, CSC and RPC detectors. Track stubs in the DT and CSC detectors are identified and forwarded to separate track-finders for each sub-detector (DTTF and CSCTF) which builds full muon tracks and assigns them a $p_{\rm T}$ value. The RPC identifies muon candidates directly from hits in pattern comparator logic, and also provides data to the CSC trigger system to help resolve ambiguities caused by 2 muons in the same CSC. The identified candidates from all three systems are sent to the GMT, where they are combined and the four best muon candidates in barrel and endcap are forwarded to the GT.

The efficiency of the L1 muon trigger with a 14 GeV threshold can be seen in Fig. 5.4. The efficiency at the plateau is 2% lower in 2012 with respect to 2011 due to an optimization aimed to reduce the single muon trigger rate by 50% which allowed to keep $p_{\rm T}$ thresholds for 2012 running as low as the ones used for 2011. In both 2011 and 2012 the efficiency of the L1 single muon trigger was greater than 90%.

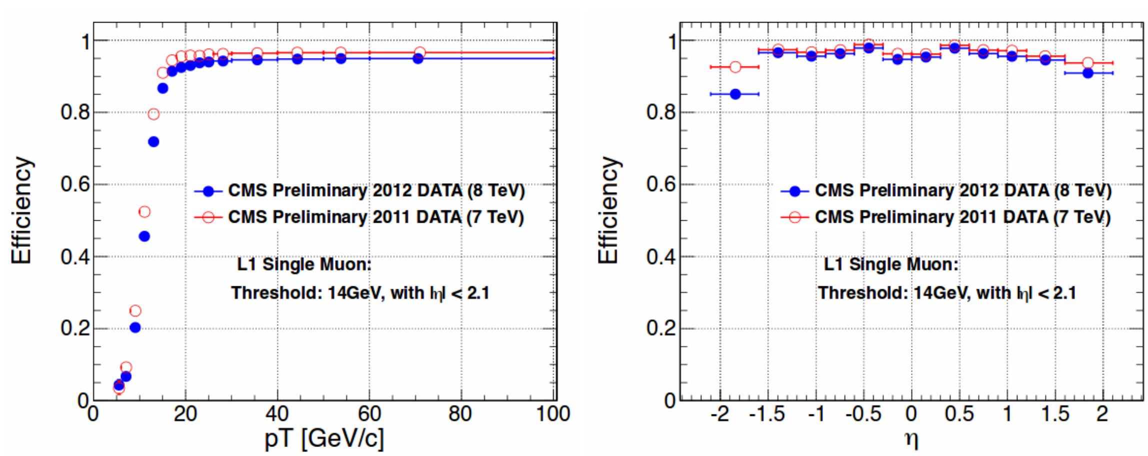

Figure 5.4: Efficiency of the L1 muon trigger with a 14 GeV threshold as a function of the muon $p_{\rm T}$ (left) and η (right). From Ref. [112].

5.1.4 L1 Global Trigger

The Global Trigger is responsible for combining trigger data from the muon and calorimeter systems, synchronizing data arriving at different times and communicating the L1 decision to the timing, trigger and control (TTC) system for distribution to the subdetectors over a network of optical fibers to initiate the readout. All of the trigger objects are accompanied by their coordinates in (η, ϕ) space, which allows the GT to vary thresholds based on location and to require trigger objects to be close or far from each other in space.

5.2 The High Level Trigger

5.2.1 Hardware

The HLT hardware is composed of a "filter farm" of CPUs which execute offline-quality reconstruction algorithms using full detector granularity to improve the resolution obtained by the L1 trigger system. The high output rate of the L1 trigger places significant demands on the filter farm hardware as well as the HLT algorithms in order to minimize dead time. One key feature is the flexibility of the trigger architecture, which allowed the computing power of the HLT filter farm to incrementally increase throughout the first LHC run [114]. The original HLT filter farm consisted of 720 Intel® Xeon® E5430 dual 4-core CPUs. This was then extended in May 2011 with 288 Intel® Xeon® X5650 dual 6-core CPUs with hyper-threading capability. The farm was extended once more to its final configuration in May 2012 with 256 Intel® Xeon® E5-2670 dual 8-core CPUs with hyper-threading capability. The final HLT filter farm consisted of more than 13000 cores at the end of 2012.

5.2.2 Software

The HLT software consists of a wide variety of different algorithms which are organized into "paths". The algorithms used are meant to be as close as possible to the offline reconstruction, but are limited by the available computing power. A single HLT path is composed of a series of modules which are either "producers" which perform reconstruction (e.g. of tracks or jets) or "filters" which make selections (such as p_{T} and η requirements) on the reconstructed objects. The modules are ordered such that when possible the CPU intensive algorithms are executed in the final stages of the path. A schematic drawing of the HLT path structure can be seen in Figure 5.5 [115].

Each path selects a given event topology, such as very basic object selection (e.g. single muon, single electron, single jet, double muon, double electron), "cross-triggers" (e.g. electron plus jets, muon plus jets), as well as highly signal specific topologies (e.g. displaced photons, razor variables [116], α_T [117]). The paths are organized into a "menu" which assigns a pass/fail decision for each path to all events passing the L1 trigger. Each HLT menu is designed to handle a specific maximum instantaneous luminosity by adjusting thresholds and parameters n, known as prescales, such that a path with a prescale n selects only 1 of n passing events. The prescale for primary physics triggers is normally 1, meaning that all events passing that trigger are recorded. The prescale for secondary triggers used for efficiency measurements, background estimations, or calibration and monitoring of the detector are assigned a prescale value greater than 1 which ensures that a sufficient number of events are collected for the trigger's purpose while maintaining a low output rate. The HLT menu is adaptable to different instantaneous luminosities via different prescale "columns" which define a set of prescales for all paths in the menu and can be changed during data taking. In total there were over 400 HLT paths in the final HLT menu used in 2012.

The efficiency of the HLT software algorithms has evolved over the course of the first LHC run and has impressively met the demands of the physics program. A few examples of the efficiency of triggers based upon standard physics objects can be seen in Figs. 5.6, 5.7, and 5.8 [118].

5.2.3 Menu Performance

Two complementary methods are used to monitor the CPU usage of the HLT software algorithms. The first method directly measures the time taken by the HLT selection and reconstruction steps for each event during data-taking. A second method rapidly samples every CPU in the farm to determine its state, and the time per event is calculated based on the frequency of finding the CPU in a non-idle state. The two methods give consistent results. Using the second method, the total busy fraction of the filter farm can also be determined.

To estimate the CPU usage of an HLT menu at a higher instantaneous luminosity, the average busy fraction over the course of a previous LHC fill is measured and a fit is performed as shown in the left panel of Fig. 5.9. An exponential function is found to give a

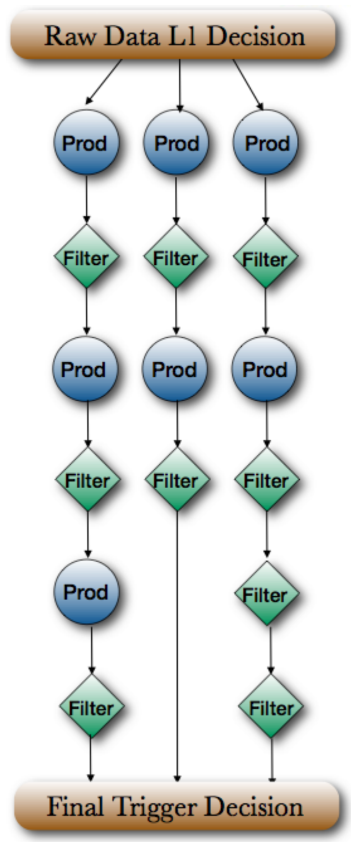

Figure 5.5: Schematic drawing of the HLT path structure. From Ref. [115].

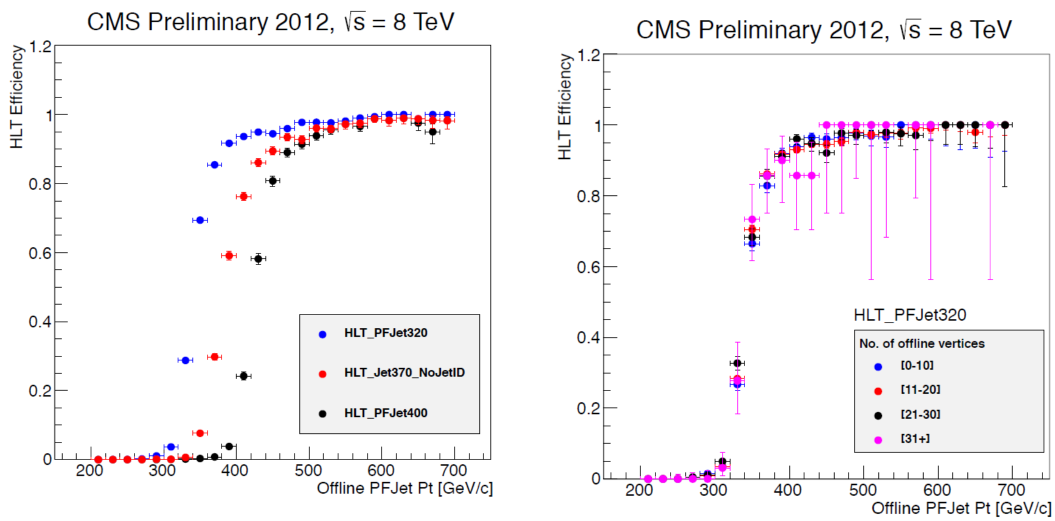

Figure 5.6: Left: HLT efficiency of jet paths with different p_{T} thresholds and identification requirements as a function of the offline jet p_{T} . Right: HLT efficiency of a single jet trigger with 320 GeV p_{T} threshold in bins of different pileup (based on the number of reconstructed offline vertices). From Ref. [118].

good description of the data over a wide range of luminosities. In addition, we also measure the time per event for each type of machine used in the filter farm as shown in the right panel of Fig 5.9. The time per event is observed to be approximately linear as a function of luminosity on the Intel Xeon® E5430® CPUs. The other two types of CPUs employ Intel's® hyper-threading to run twice as many concurrent processes as there are physical cores by using parts of the CPU that would otherwise be idle. As a result, the time per event for these hyper-threaded CPUs increases faster than linearly as the CPU is saturated with increasing luminosity and input rate. Using this information, it is possible to calculate the maximum time per event of the HLT menu for a given L1 input rate, and also the instantaneous luminosity at which this limit would be reached. The figure of merit used is the time per event for an Intel® Xeon® E5430 CPU.

The per-event time budget of the HLT decreases with increasing L1 input rate. With the 2011 configuration of the filter farm, the HLT filter farm could sustain an average processing

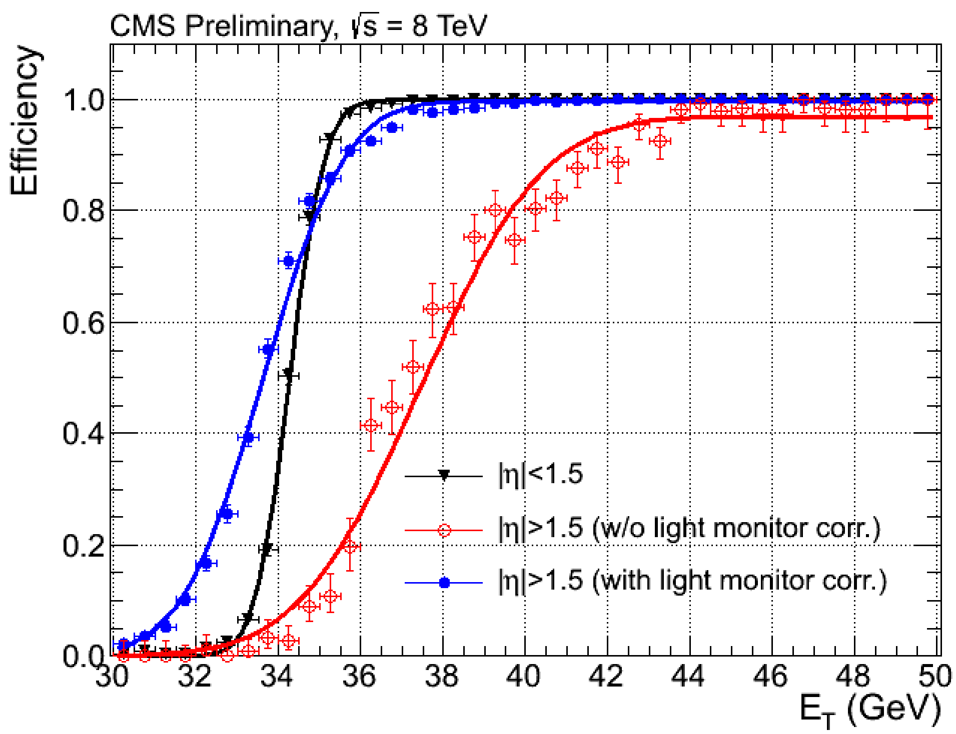

Figure 5.7: HLT efficiency of an online cut of E_T >33 GeV in the barrel ($|\eta|$ <1.5) and endcap ($|\eta|$ >1.5) regions for electrons with loose identification, as a function of the offline E_T. The endcap region is divided into two running periods, before and after the ECAL transparency loss correction were introduced at the HLT. From Ref. [118].

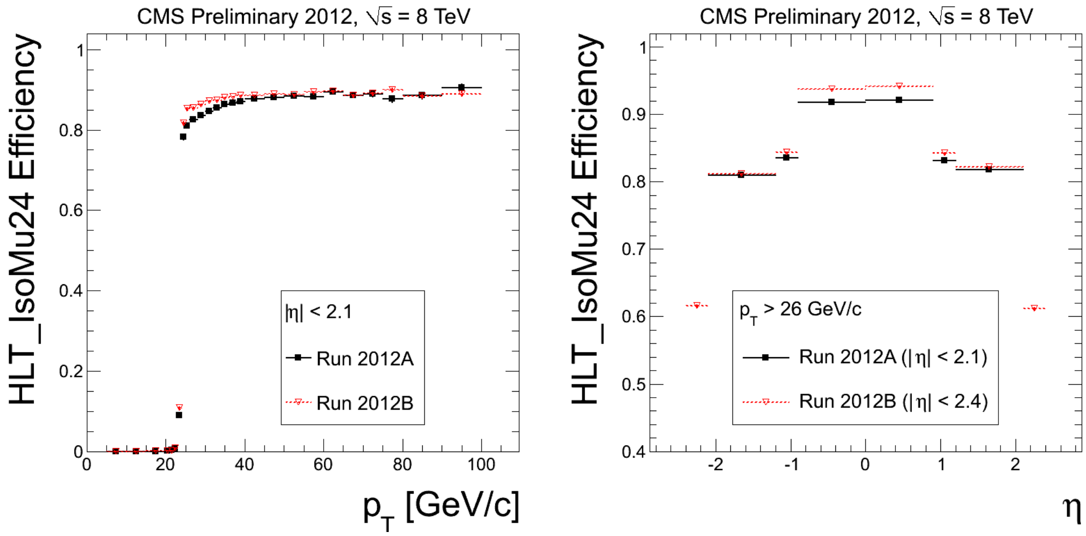

Figure 5.8: HLT Efficiency for a single isolated muon trigger with a 24 GeV p_{T} threshold in Run2012A (black) and Run2012B (red) as a function of p_{T} (left) and η (right) for muons with tight identification requirements designed to give the lowest misidentification probability. The trigger shows a higher efficiency in Run2012B due to the introduction of pileup corrections for the isolation, as well as an extended η-acceptance. From Ref. [118].

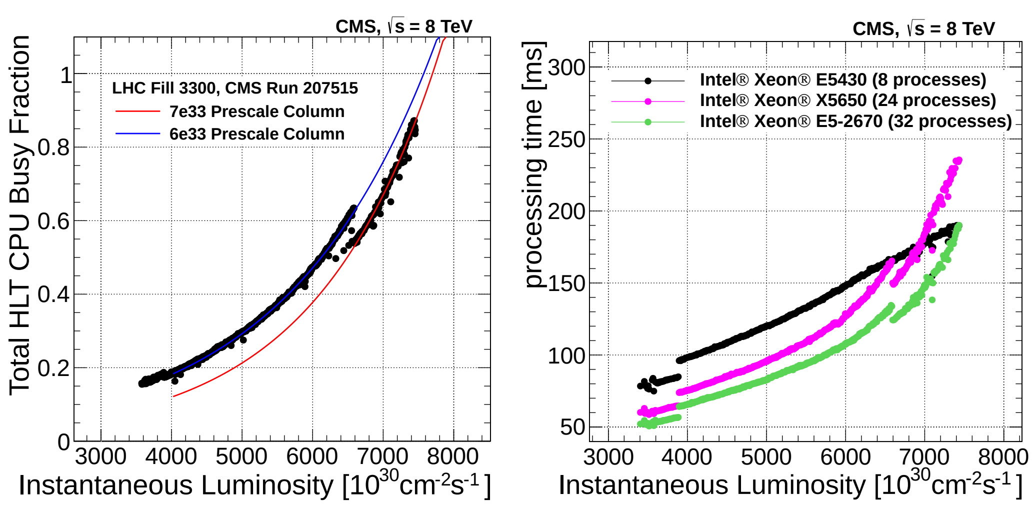

Figure 5.9: Measurements used to measure the CPU capacity of the HLT filter farm. Left: The average CPU busy fraction as a function of instantaneous luminosity for one LHC fill. Luminosity sections with data-taking dead time $> 40\%$ have been removed. Right: HLT processing time per event as a function of instantaneous luminosity on the three different machine types used in the filter farm.

time of up to $\sim$ 90 ms per event for an L1 input rate of 100 kHz without incurring dead time. With increased CPU power available in 2012, the farm could sustain a per-event time of $\sim$ 200 ms.

During the commissioning of the LHC, the luminosity was much lower than design. The flexibility of the CMS trigger system was again utilized to implement full reconstruction of pixel tracks at the HLT. As can be seen in Fig. 5.10, this global pixel track reconstruction approximately doubled the CPU time per event but enabled the observation of long-range near-side two particle correlations [119] in proton-proton collisions for the first time.

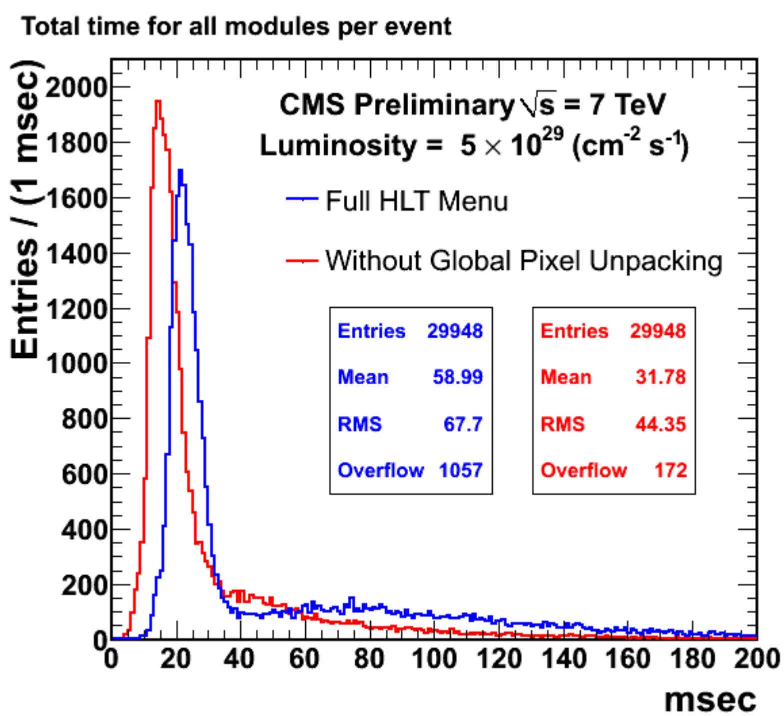

Figure 5.10: HLT processing time per event with and without global pixel unpacking during commissioning at $L = 5 \times 10^{29}\text{cm}^{-2}\text{s}^{-1}$.

Each menu is validated in an offline environment before being used for online data-taking. Each new version of the menu is compared to a previous version on a single machine to ensure that the CPU consumption does not exceed expectations. The menus are tested by running the HLT once with each menu over the same sample of previously collected events. The measurement is done using a machine with similar core architecture to the Intel® Xeon® E5430 CPU, and is performed using the direct timing measurement described above. New luminosity and L1 input rate limits can then be determined by using the relative performance of the new menu and the measured performance of the older menu. An example of an offline comparison of the times per event for two different HLT menus is shown in Figure 5.11. When testing a new menu, the time per event for each HLT path is also checked to determine which paths are the most CPU intensive. The algorithms for CPU intensive paths are then optimized to ensure that the total processing time does not exceed the limitations of the system.

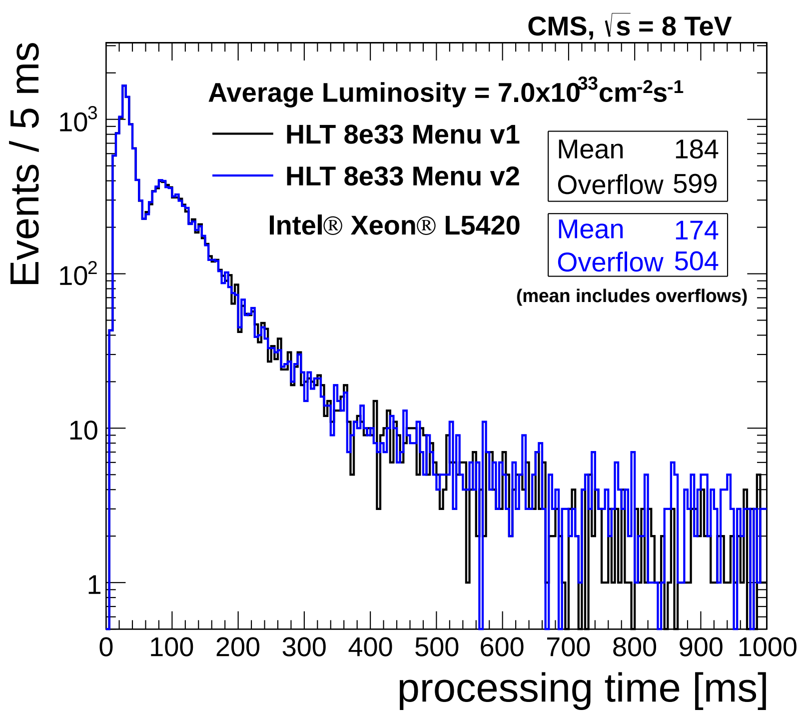

Figure 5.11: Comparison of the time per event measured for two different HLT menus using a validation machine outside of the event filter farm.

In addition to the CPU performance, another important parameter for the HLT is the event rate, which is constrained by the offline storage and processing capabilities. A convenient measure is the “cross section” of the HLT menu, which is defined as the event rate divided by the instantaneous luminosity. If the HLT menu has the same efficiency and noise component as a function of instantaneous luminosity, the cross section should be flat. A plot of the HLT cross section during 2012 can be seen in Fig. 5.12 [120]. In the second half of 2012, with a long shutdown of the LHC machine for upgrades imminent, the event rate of the HLT was increased in a program known as “data parking”. In this program, additional rate (approximately 500 Hz at an instantaneous luminosity of $6.5 \times 10^{3}3\ \mathrm{cm}^{-2}\mathrm{s}^{-1}$) was recorded without being reconstructed promptly, but instead stored and reconstructed after the 2012 run had finished. In this way the constraint from processing capabilities was avoided. The total HLT cross section is shown in blue and the prompt and parked components are shown in green and yellow, respectively.

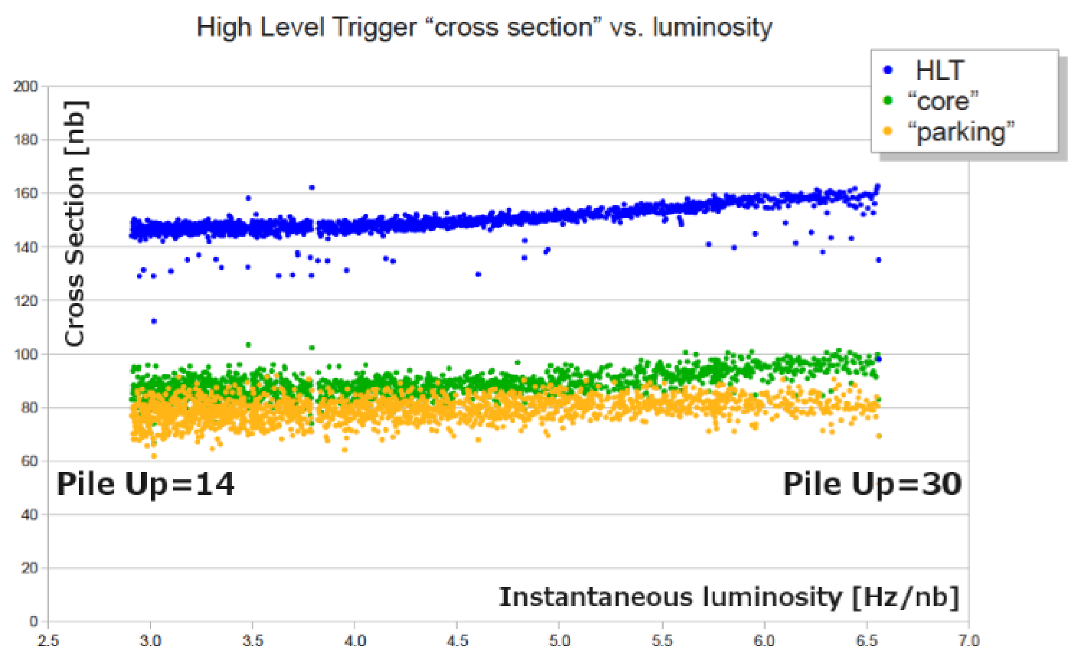

Figure 5.12: Cross section of the HLT menu in 2012 as a function of the instantaneous luminosity. From Ref. [120].

5.3 DAQ

The L1 and HLT are supported by a sytem of hardware and software modules known as the DAQ system. The DAQ system was designed to be modular which has enabled its expansion as the luminosity increased. The DAQ assembles data fragments from separate detector components into full events in two stages [121] and transports them between the L1, HLT, and data storage center. An overview of the DAQ architecture can be seen in Fig. 5.13.

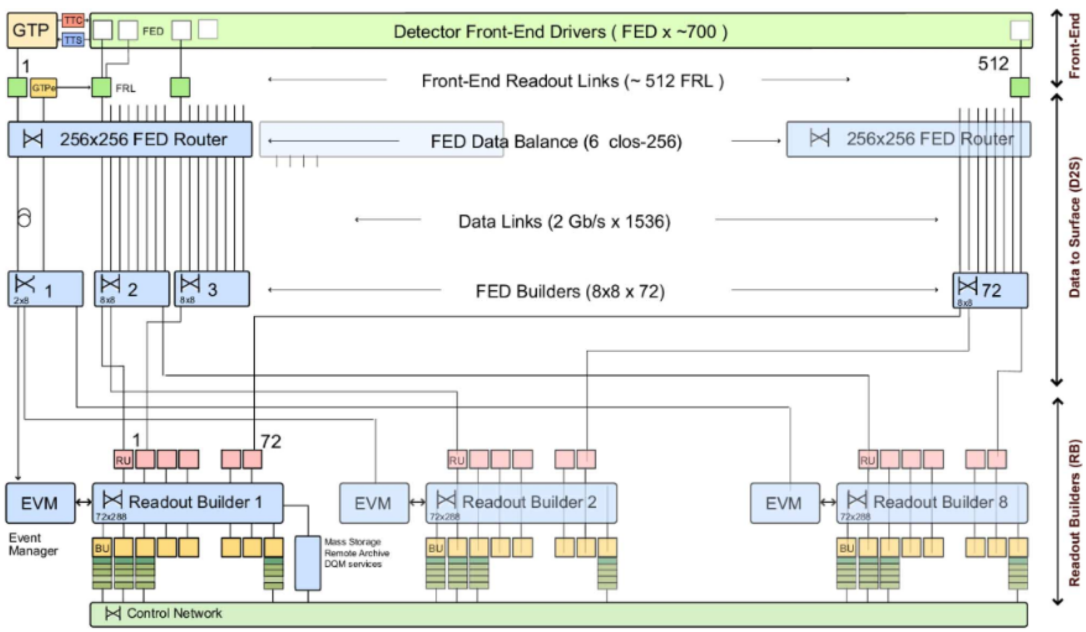

Figure 5.13: Simplified sketch of the CMS DAQ system. From Ref. [121].

The first stage begins when an event is accepted by the L1, after which data fragments corresponding to the accepted event are read out from the front-end drivers (FED's). The FED's are subdetector specific data sources which feed 476 front-end readout links (FRL's) which merge the data of up to two FEDs into one stream. The 2 kB outputs of the FRL's are then assembled into 16 kB "super-fragments" by the FED builders and are distributed to Readout Units (RU's). Myrinet technology [122] is used in the FED builder and for transfer of data from the detector to the surface.

Besides Filter Units (FU's) which execute the HLT software algorithms, the HLT filter farm also consists of Builder Units (BU's) which receive super-fragments from the RU's via TCP/IP based on Gigabit Ethernet, and assemble them into complete events of approximately 1 MB. Each RU builds events at 12.5 kHz with a total data throughput of approximately 200 MB/s. The BU ships an assembled event to a FU of the HLT CPU farm upon request from an FU. The FU then unpacks the raw data into detector-specific data structures and performs the software algorithms of the HLT. Associated builder and filter units (BUFU's) are located in a single multi-core machine and communicate via shared memory. The data flow in each RU is supervised by an event manager (EVM) which also keeps track of the memory occupancy of the RU's. The event manager can request a reduced trigger rate if an RU is has insufficient memory to buffer incoming super-fragments.

The HLT software collects the accepted events and divides them into different physics or calibration "streams", and forwards them for offline processing. The different streams is utilized to optimize the data access for the offline analysis. Events from the different streams undergo different reconstruction. For example, events in the physics stream will be fully reconstructed using all detector information, whereas calibration or monitoring streams will be reconstructed using only use a subset of the available data. In normal operation, the accepted events are immediately sent on to the offline Tier-0 centre for the initial offline processing step.

Chapter 6

The Search for tb Resonances

6.1 Introduction

Massive charged gauge bosons, generically referred to as W′, are predicted by various extensions of the standard model (SM) [69, 123–126]. Searches for W' bosons at the Large Hadron Collider (LHC) have been conducted in the lepton-neutrino, diboson, and light-quark final states [88–91, 127–132]. While the most stringent limits come from the searches in the leptonic final states ($\mathrm{W}' \rightarrow \ell\nu$ where ℓ is a charged lepton), the constraints do not apply to W′ bosons with purely right-handed couplings if the mass of the hypothetical right-handed neutrino is larger than a few GeV [133]. Dedicated searches for W′ bosons with purely right-handed couplings have been performed by the CMS [92] and ATLAS [93] collaborations assuming the mass of the right-handed neutrino is less than the mass of the W′ boson. Searches for W′ bosons that decay to a quark final state such as $\mathrm{W}'^{+} \rightarrow \mathrm{t\bar{b}}$ (or charge conjugate) make no assumptions regarding the mass of the right-handed neutrino and are thus complementary to searches in the leptonic channels. Furthermore, the decay chain $\mathrm{W}' \rightarrow \mathrm{tb}$, $\mathrm{t} \rightarrow \mathrm{bW} \rightarrow \mathrm{b}\ell\nu$ is in principle fully reconstructible, thereby leading to resonant mass peaks even in the case of wider W′ resonances. In addition, due to the presence of leptons in the final state, it is easier to suppress the QCD multijet background for this decay chain than for a generic $\mathrm{W}' \rightarrow \mathrm{qq}'$ decay. Finally, in some models the W′ boson may couple more strongly to the third generation of fermions than to the first and second generations [134, 135]. Thus the $W' \to tb$ decay is an important channel in the search for W' bosons.

Experimental searches for $W' \to tb$ decays have been performed at the Tevatron [136–138] and at the LHC [139, 140]. The CMS search at $\sqrt{s} = 7$ TeV [139] used a multivariate analysis based on boosted decision trees (BDT) [141] to set a lower mass limit of 1.85 TeV for W' bosons with purely right-handed couplings. The results of this search are shown in Fig. 6.1.

If the W' boson has left-handed couplings, interference between $W' \to tb$ and SM single-top-quark production via $W \to tb$ can contribute as much as 5–20% of the total W' rate, depending on the W' mass and its couplings [142]. This interference effect was taken into account in the CMS search. The analysis also set constraints on an arbitrary set of left- and right-handed couplings of the W' boson.

This chapter describes the first $W' \to tb$ search at $\sqrt{s} = 8$ TeV and uses data collected by the CMS experiment, corresponding to an integrated luminosity of 19.5 fb^{-1}. For a W' boson with a mass of 2 TeV, the production cross section at $\sqrt{s} = 8$ TeV is larger by approximately a factor of two compared to $\sqrt{s} = 7$ TeV [143]. The dataset used in this analysis corresponds to an integrated luminosity that is approximately a factor of four larger than that in the $\sqrt{s} = 7$ TeV analysis. Following the earlier publication [139], we analyze events with a lepton (e, μ), jets, and missing transverse energy (E_T^{miss}) for an arbitrary combination of left- and right-handed couplings.

6.1.1 Signal Modeling

The $W' \to tb \to \ell\nu bb$ decay is characterized by the presence of a high-p_T isolated lepton, significant E_T^{miss} associated with the undetected neutrino, and at least two high-p_T b-jets. The signal modeling is identical to that in Ref. [139] and uses the following model-independent lowest order effective Lagrangian to describe the interaction of the W' boson with SM fermions:

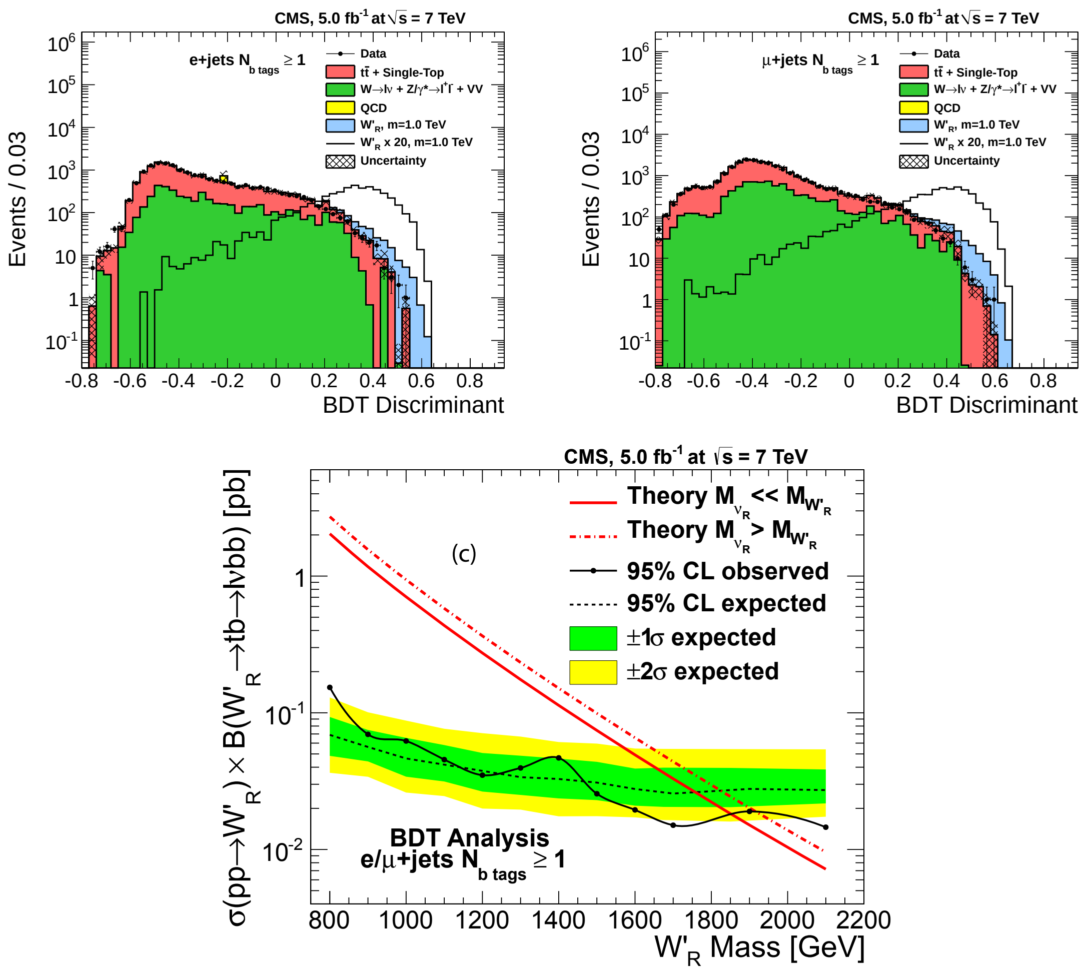

Figure 6.1: Distribution of the BDT output discriminant. The data, expected backgrounds, and a W'_R signal with mass of 1.0 TeV are shown for the electron+jets (muon+jets) samples in the top left (top right). The hatched bands represent the total normalization uncertainty on the predicted backgrounds. Bottom: The expected and measured 95% confidence level upper limits on the production cross section of right handed W' bosons obtained using the BDT discriminant for the combined electron+jets and muon+jets samples. The 1σ and 2σ excursions from the expected limit are also shown. The solid red line represents the theoretical prediction.

$$\mathcal{L} = \frac{V_{f_i f_j}}{2\sqrt{2}} g_w \overline{f}_i \gamma_\mu \big(a^{\mathrm{R}}_{f_i f_j}(1+\gamma^5) + a^{\mathrm{L}}_{f_i f_j}(1-\gamma^5)\big) \mathrm{W}'^{\mu} f_j + \mathrm{h.c.}\,, \tag{6.1}$$

where $a^{\mathrm{R}}_{f_i f_j}, a^{\mathrm{L}}_{f_i f_j}$ are the right- and left-handed couplings of the W$'$ boson to fermions f_i and f_j, $g_w = e/(\sin\theta_W)$ is the SM weak coupling constant and θ_W is the weak mixing angle; $V_{f_i f_j}$ is the CKM matrix element if the fermion f is a quark, and $V_{f_i f_j} = \delta_{ij}$ if it is a lepton, where δ_{ij} is the Kronecker delta and i, j are the generation numbers. For our search we consider models where $0 < a^{\mathrm{L,R}}_{f_i f_j} < 1$. The notation is defined in such a way that, for a so-called SM-like W$'$ boson, $a^{\mathrm{L}}_{f_i f_j} = 1$ and $a^{\mathrm{R}}_{f_i f_j} = 0$.

We produce simulated samples using the following nomenclature:

- W'_{L} with $a^{\mathrm{L}}_{ud} = a^{\mathrm{L}}_{cs} = a^{\mathrm{L}}_{tb} = 1$ and $a^{\mathrm{R}}_{ud} = a^{\mathrm{R}}_{cs} = a^{\mathrm{R}}_{tb} = 0$
- W'_{R} with $a^{\mathrm{L}}_{ud} = a^{\mathrm{L}}_{cs} = a^{\mathrm{L}}_{tb} = 0$ and $a^{\mathrm{R}}_{ud} = a^{\mathrm{R}}_{cs} = a^{\mathrm{R}}_{tb} = 1$
- $\mathrm{W}'_{\mathrm{LR}}$ with $a^{\mathrm{L}}_{ud} = a^{\mathrm{L}}_{cs} = a^{\mathrm{L}}_{tb} = 1$ and $a^{\mathrm{R}}_{ud} = a^{\mathrm{R}}_{cs} = a^{\mathrm{R}}_{tb} = 1$

The differences between W$'$ bosons with left- and right-handed couplings that are relevant for our search are as follows. Firstly, W'_{L} bosons, which have left-handed couplings, couple to the same fermion multiplets as the SM W boson. As a consequence, there will be interference between the two tb production diagrams with a W boson and with a W'_{L} boson. Secondly, W'_{R} bosons with purely right-handed couplings do not interfere with the SM W boson. Since their leptonic decays involve a right-handed neutrino ν_{R} of unknown mass, they decay exclusively to qq' final states if the mass of the right-handed neutrino, M(ν_{R}), is greater than the mass of the W$'$ boson, M(W$'$). If M(ν_{R}) < M(W$'$), they may decay to $\ell\nu$ and qq' final states, leading to different branching fractions for the W$' \to$ tb decay. In the absence of interference between the SM W boson and the W$'$ boson, and if M(ν_{R}) $\ll$ M(W$'$), there is no practical difference between W'_{L} and W'_{R} for our search.

The invariant mass distributions at $\sqrt{s} = 7$ TeV for W'_{R}, W'_{L}, and $\mathrm{W}'_{\mathrm{LR}}$ bosons are shown in Figure 6.2. These distributions are obtained from the samples and selection used in Ref. [139] and match the reconstructed jets, lepton, and $\mathrm{E}_{\mathrm{T}}^{\mathrm{miss}}$ of a W$'$ boson with mass 1.2 TeV to the generator level objects. These distributions show the resonant structure around the generated W′ mass, and a minimum corresponding to the destructive interference between the amplitudes for production of left-handed fermions via the SM W and W'_L bosons. The same features are present in the samples used for the analysis described here.

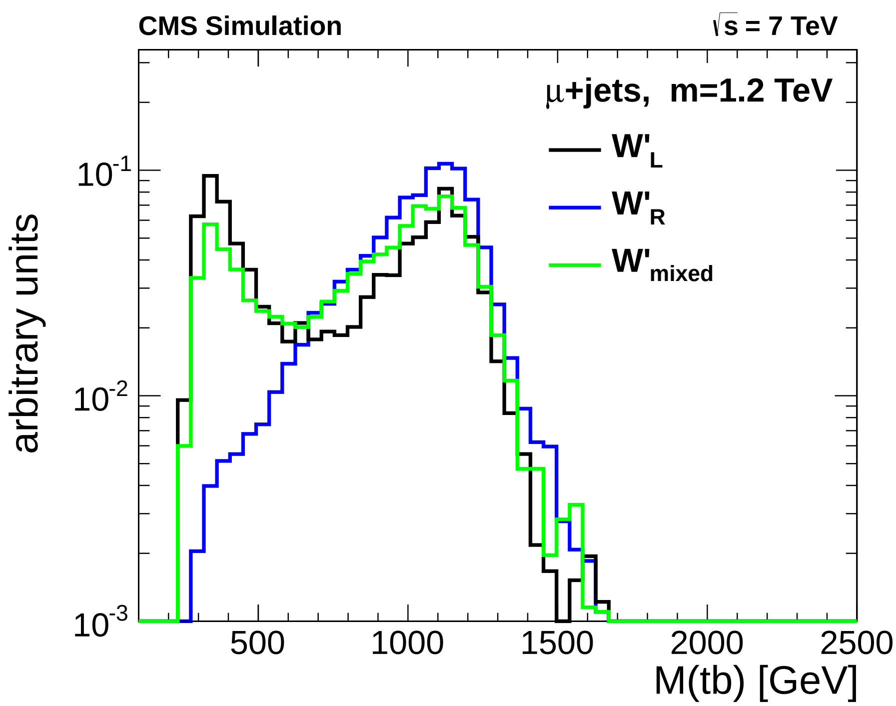

Figure 6.2: Simulated invariant mass distributions for production of W'_R, W'_L, and W'_{LR} with a mass 1.2 TeV. For the cases of W'_L and W'_{LR}, the invariant mass distributions also include the contribution from s-channel single top quark production and show a minimum corresponding to the destructive interference between the amplitudes for production of left-handed fermions via the W and W'_L bosons. From Ref. [139].

Tables 6.1, 6.2, and 6.3 list the leading order (LO) production cross sections at $\sqrt{s}$ = 8 TeV for a W′ boson with right-handed couplings (W'_R), for a W′ boson with SM-like couplings (W'_L),and for a W′ boson with both left and right hand couplings (W'_{LR}). The W'_L and W'_{LR} cross sections take into account the s-channel SM W diagram and the s-channel W′

diagram, and the interference between the two. The SINGLETOP MC generator [143] is used, which simulates electroweak top-quark production processes based on the complete set of tree-level Feynman diagrams calculated by the COMPHEP package [144]. Finite decay widths and spin correlations between resonance state production and subsequent decay are taken into account. The factorization scale is set to the W′-boson mass for the generation of the samples and the computation of the leading-order (LO) cross section. The LO cross section is scaled to next-to-leading order (NLO) using a K factor of 1.2 based on Refs. [145, 146]. In order to ensure that the NLO rates and shapes of relevant distributions are reproduced, the SINGLETOP generator includes NLO corrections, and normalization and matching between various partonic subprocesses are performed. The top-quark mass is chosen to be 172.5 GeV and the CTEQ6M [147] parton distribution functions (PDF) are used. The uncertainties on the cross-section are about 8.5% and include contributions from NLO scale (3.3%), PDFs (7.6%), α_s(1.3%) and top quark mass (< 1%).

6.2 Datasets and Background Monte Carlo Samples

The data sets used for the analysis presented in this note were collected using the CMS detector during the LHC run in 2012. Data was recorded at the center-of-mass energy $\sqrt{s} = 8$ TeV and a total of 19.5 fb^{-1} was collected and reconstructed with the 53X version of the CMS software.

Table 6.4 lists the datasets analyzed, and the corresponding luminosity. A summary of the Monte Carlo (MC) samples used for the background studies/estimation is provided in Table 6.5. The $\mathrm{t\bar{t}}$, W+jets, and Z/γ^*+jets background processes are generated with MADGRAPH 5.1 [148]. The $\mathrm{t\bar{t}}$ background is normalized to the next-to-NLO (NNLO) cross section [149]. The SM single-top-quark backgrounds are estimated using samples generated with POWHEG [150], normalized to an approximate NNLO cross section [151]. For the W'_{R} search, s-channel, t-channel, and tW single-top-quark events are considered as backgrounds. Because of interference between W′ and s-channel single-top-quark production, in the analysis for W'_{L} and $\mathrm{W}'_{\mathrm{LR}}$ bosons only the t-channel and the tW processes contribute to the

Process	MC Generator	σ (pb)	Number of events
$\mathrm{W'_R} \to \mathrm{tb}$ (with W $\to e/\mu/\tau/\nu$)			
$\mathrm{M(W'_R)}$ = 800 GeV	COMPHEP	2.3002 (LO)	920654
$\mathrm{M(W'_R)}$ = 900 GeV	COMPHEP	1.3818 (LO)	942816
$\mathrm{M(W'_R)}$ = 1000 GeV	COMPHEP	0.85538 (LO)	907958
$\mathrm{M(W'_R)}$ = 1100 GeV	COMPHEP	0.54325 (LO)	831508
$\mathrm{M(W'_R)}$ = 1200 GeV	COMPHEP	0.35203 (LO)	965528
$\mathrm{M(W'_R)}$ = 1300 GeV	COMPHEP	0.23219 (LO)	881046
$\mathrm{M(W'_R)}$ = 1400 GeV	COMPHEP	0.15547 (LO)	920262
$\mathrm{M(W'_R)}$ = 1500 GeV	COMPHEP	0.10518 (LO)	907297
$\mathrm{M(W'_R)}$ = 1600 GeV	COMPHEP	0.072012 (LO)	892146
$\mathrm{M(W'_R)}$ = 1700 GeV	COMPHEP	0.049683 (LO)	924438
$\mathrm{M(W'_R)}$ = 1800 GeV	COMPHEP	0.034576 (LO)	841448
$\mathrm{M(W'_R)}$ = 1900 GeV	COMPHEP	0.024249 (LO)	835381
$\mathrm{M(W'_R)}$ = 2000 GeV	COMPHEP	0.017124 (LO)	841836
$\mathrm{M(W'_R)}$ = 2100 GeV	COMPHEP	0.012176 (LO)	926108
$\mathrm{M(W'_R)}$ = 2200 GeV	COMPHEP	0.0087191 (LO)	932785
$\mathrm{M(W'_R)}$ = 2300 GeV	COMPHEP	0.0062918 (LO)	784768
$\mathrm{M(W'_R)}$ = 2400 GeV	COMPHEP	0.0045757 (LO)	894786
$\mathrm{M(W'_R)}$ = 2500 GeV	COMPHEP	0.0033568 (LO)	878643
$\mathrm{M(W'_R)}$ = 2600 GeV	COMPHEP	0.0024870 (LO)	944599
$\mathrm{M(W'_R)}$ = 2700 GeV	COMPHEP	0.0018624 (LO)	915158
$\mathrm{M(W'_R)}$ = 2800 GeV	COMPHEP	0.0014102 (LO)	835281
$\mathrm{M(W'_R)}$ = 2900 GeV	COMPHEP	0.0010818 (LO)	910111
$\mathrm{M(W'_R)}$ = 3000 GeV	COMPHEP	0.00084115 (LO)	932601

Table 6.1: Details of the $\mathrm{W'_R}$ Monte Carlo samples used for the analysis.

background. The diboson (WW) background is generated with PYTHIA 6.424 [152].

For all simulated samples, PYTHIA tune Z2* [153] is used for parton showering, hadronization, and simulation of the underlying event. The PYTHIA and MADGRAPH backgrounds use the CTEQ6L1 PDFs, and the POWHEG backgrounds use the CTEQ6M PDFs [147]. The resulting events are processed with the full GEANT4 [154] simulation of the CMS detector.

Process	MC Generator	σ (pb)	Number of events
$W'_L \rightarrow tb$ (with W $\rightarrow e/\mu/\tau/\nu$)			
$M(W'_L) = 800$ GeV	COMPHEP	3.1089 (LO)	941306
$M(W'_L) = 900$ GeV	COMPHEP	2.2731 (LO)	906657
$M(W'_L) = 1000$ GeV	COMPHEP	1.8087 (LO)	908337
$M(W'_L) = 1100$ GeV	COMPHEP	1.547 (LO)	798919
$M(W'_L) = 1200$ GeV	COMPHEP	1.3870 (LO)	959534
$M(W'_L) = 1300$ GeV	COMPHEP	1.2945 (LO)	963820
$M(W'_L) = 1400$ GeV	COMPHEP	1.2390 (LO)	942066
$M(W'_L) = 1500$ GeV	COMPHEP	1.2061 (LO)	952749
$M(W'_L) = 1600$ GeV	COMPHEP	1.1869 (LO)	954829
$M(W'_L) = 1700$ GeV	COMPHEP	1.1761 (LO)	948063
$M(W'_L) = 1800$ GeV	COMPHEP	1.1705 (LO)	936673
$M(W'_L) = 1900$ GeV	COMPHEP	1.1678 (LO)	911699
$M(W'_L) = 2000$ GeV	COMPHEP	1.1673 (LO)	903371
$M(W'_L) = 2100$ GeV	COMPHEP	1.1680 (LO)	861801
$M(W'_L) = 2200$ GeV	COMPHEP	1.1692 (LO)	922413
$M(W'_L) = 2300$ GeV	COMPHEP	1.1711 (LO)	964171
$M(W'_L) = 2400$ GeV	COMPHEP	1.1727 (LO)	931031
$M(W'_L) = 2500$ GeV	COMPHEP	1.1746 (LO)	911826
$M(W'_L) = 2600$ GeV	COMPHEP	1.1763 (LO)	931038
$M(W'_L) = 2700$ GeV	COMPHEP	1.1780 (LO)	907930
$M(W'_L) = 2800$ GeV	COMPHEP	1.1797 (LO)	917514
$M(W'_L) = 2900$ GeV	COMPHEP	1.1810 (LO)	940379
$M(W'_L) = 3000$ GeV	COMPHEP	1.1825 (LO)	934903

Table 6.2: Details of the W'_L Monte Carlo samples used for the analysis.

6.3 Object Reconstruction and Event Selection

The analysis relies on the reconstruction of three types of objects: electrons, muons and jets. The events are reconstructed using a full Particle Flow (PF) approach [155, 156]. The PF event reconstruction aims to reconstruct and identify all observable particles in the event (electrons, muons, photons, charged hadrons and neutral hadrons) by combining information from all CMS sub-detectors in the form of charged-particle inner tracks, muon detector tracks, and calorimetric clusters. This list of individual particles is then used to

Process	MC Generator	σ (pb)	Number of events
$W'_{\mathrm{LR}} \to$ tb (with W $\to e/\mu/\tau/\nu$)			
M(W'_{LR}) = 800 GeV	COMPHEP	5.4166 (LO)	920851
M(W'_{LR}) = 900 GeV	COMPHEP	3.6684 (LO)	962105
M(W'_{LR}) = 1000 GeV	COMPHEP	2.6815 (LO)	952695
M(W'_{LR}) = 1100 GeV	COMPHEP	2.1031 (LO)	499057
M(W'_{LR}) = 1200 GeV	COMPHEP	1.7539 (LO)	949408
M(W'_{LR}) = 1300 GeV	COMPHEP	1.5389 (LO)	957707
M(W'_{LR}) = 1400 GeV	COMPHEP	1.4043 (LO)	499049
M(W'_{LR}) = 1500 GeV	COMPHEP	1.3194 (LO)	972899
M(W'_{LR}) = 1600 GeV	COMPHEP	1.2650 (LO)	948242
M(W'_{LR}) = 1700 GeV	COMPHEP	1.2305 (LO)	951497
M(W'_{LR}) = 1800 GeV	COMPHEP	1.2090 (LO)	963803
M(W'_{LR}) = 1900 GeV	COMPHEP	1.1954 (LO)	978267
M(W'_{LR}) = 2000 GeV	COMPHEP	1.1872 (LO)	929173
M(W'_{LR}) = 2100 GeV	COMPHEP	1.1824 (LO)	913931
M(W'_{LR}) = 2200 GeV	COMPHEP	1.1798 (LO)	938946
M(W'_{LR}) = 2300 GeV	COMPHEP	1.1787 (LO)	903118
M(W'_{LR}) = 2400 GeV	COMPHEP	1.1784 (LO)	956188
M(W'_{LR}) = 2500 GeV	COMPHEP	1.1791 (LO)	962673
M(W'_{LR}) = 2600 GeV	COMPHEP	1.1792 (LO)	945159
M(W'_{LR}) = 2700 GeV	COMPHEP	1.1803 (LO)	919176
M(W'_{LR}) = 2800 GeV	COMPHEP	1.1813 (LO)	921391
M(W'_{LR}) = 2900 GeV	COMPHEP	1.1825 (LO)	927989
M(W'_{LR}) = 3000 GeV	COMPHEP	1.1835 (LO)	932353

Table 6.3: Details of the W'_{LR} Monte Carlo samples used for the analysis.

build jets, determine the missing transverse energy, and to quantify charged lepton isolation. The details of the object selection are provided below.

6.3.1 Trigger

Events are required to pass either the inclusive isolated muon trigger with a p_{T} threshold of 24 GeV and $|\eta| < 2.1$ (HLT_IsoMu24_eta2p1_v*) or the inclusive isolated electron trigger with a p_{T} threshold of 27 GeV and identification requirements designed to be approximately 80% efficient (HLT_Ele27_WP80_v*). Data-to-simulation scale factors are applied to the MC

Sample	Luminosity (fb^{-1})
Muon Datasets	19.5
/SingleMu/Run2012A-13Jul2012-v1/AOD	
/SingleMu/Run2012A-recover-06Aug2012-v1/AOD	
/SingleMu/Run2012B-13Jul2012-v1/AOD	
/SingleMu/Run2012C-24Aug2012-v1/AOD	
/SingleMu/Run2012C-PromptReco-v2/AOD	
/SingleMu/Run2012C-EcalRecover_11Dec2012-v1/AOD	
/SingleMu/Run2012D-PromptReco-v1/AOD	
Electron Datasets	19.5
/SingleElectron/Run2012A-13Jul2012-v1/AOD	
/SingleElectron/Run2012A-recover-06Aug2012-v1/AOD	
/SingleElectron/Run2012B-13Jul2012-v1/AOD	
/SingleElectron/Run2012C-24Aug2012-v1/AOD	
/SingleElectron/Run2012C-PromptReco-v2/AOD	
/SingleElectron/Run2012C-EcalRecover_11Dec2012-v1/AOD	
/SingleElectron/Run2012D-PromptReco-v1/AOD	

Table 6.4: Data samples used for the analysis.

Process	MC Generator	σ (pb)	Number of events
Background Samples:			
$t\bar{t}$	MADGRAPH	245 (NNLO)	6923750
$t\bar{t}$	POWHEG	245 (NNLO)	21591169
Single top t-channel (tqb)	POWHEG	56.4 (∼NNLO)	3758227
Single top t-channel ($\bar{t}q\bar{b}$)	POWHEG	30.7 (∼NNLO)	1935072
Single top tW-channel	POWHEG	11.1 (∼NNLO)	497658
Single top $\bar{t}$W-channel	POWHEG	11.1 (∼NNLO)	493460
W($\rightarrow$)$\ell\nu$+jets	MADGRAPH	37509.0 (NNLO)	76041475
Z/γ^*($\rightarrow \ell\ell$)+jets ($M_{\ell\ell} > 50$)	MADGRAPH	3503.71 (NNLO)	30459503
WW	PYTHIA	54.838 (NLO)	10000431
Single top s-channel ($t\bar{b}$)	POWHEG	3.79 (∼NNLO)	259961
Single top s-channel ($\bar{t}b$)	POWHEG	1.76 (∼NNLO)	139974
Samples for Systematic Uncertainties:			
$t\bar{t}$ scale up	MADGRAPH	245 (NNLO)	5009488
$t\bar{t}$ scale down	MADGRAPH	245 (NNLO)	5387181
$t\bar{t}$ matching up	MADGRAPH	245 (NNLO)	5415010
$t\bar{t}$ matching down	MADGRAPH	245 (NNLO)	5476728

Table 6.5: Details of the background Monte Carlo samples used for the analysis.

to account for differences in the muon (electron) trigger efficiency. In the muon channel, we apply the scale factors which are determined using a "tag and probe" method. In this method, Z→ $\mu^+\mu^-$ events are selected and one muon is "tagged" as a muon by applying tight identification requirements. A second muon is then used as a "probe" and is combined with the tag muon to reconstruct a Z-boson candidate. The resulting invariant mass distribution is then fitted to extract the signal component before and after applying a particular selection requirement (in this case that the muon is matched to an object which passed the trigger). The resulting ratio of signal events determines the efficiency and can be extracted in both data and MC. The scale factor between data and MC for the muon trigger efficiency ranges from approximately 0.96 to 0.98 depending on the muon η (see Table 6.6).

In the electron channel, the trigger efficiency with respect to the selection used in this analysis is also derived using the tag and probe method. The efficiency is parametrized as a function of a the probe electron $|\eta|$ in data and $Z/\gamma^*(\rightarrow \ell\ell)$+jets MC, by counting the number of events in the invariant mass window $80 < M(\ell\ell) < 100$ GeV for all probes, and for probes matched to a trigger object. The results are shown in Fig. 6.3, and are used to derive a data-to-MC scale factor of 0.973 ± 0.002 for $|\eta| < 1.5$ and 1.020 ± 0.005 for $1.5 < |\eta| < 2.5$. No significant dependence on the probe electron p_{T} is observed, but a conservative systematic uncertainty of 2% is assigned to cover small variations in the scale factor for low p_{T} as well as the statistical uncertainty on the derived scale factor.

6.3.2 Event cleanup and vertex selection

Several event selections are applied which are designed to eliminate beam background, detector electronics noise, and other spurious detector related backgrounds.

- No scraping: the event is rejected if the fraction of high purity tracks is $< 25\%$ in events with at least 10 tracks. This requirement removes beam-induced background arising from interactions between the beam and residual gas particles or beam collimators.

- Require at least one good primary vertex (PV); the PV must have more than 4 degrees

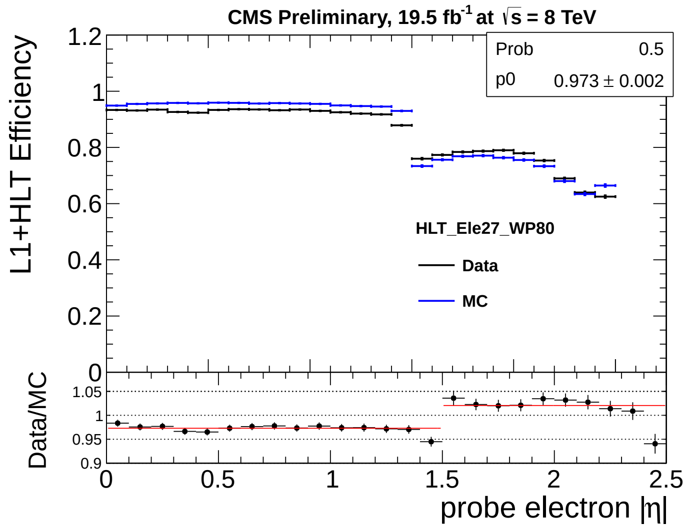

Figure 6.3: The combined L1+HLT efficiency in data and $Z/\gamma^*(\rightarrow \ell\ell)$+jets MC for the HLT path HLT_Ele27_WP80_v* as a function of the probe electron p_T as described in Section 6.3.1.

of freedom, which is roughly equivalent to the number of tracks associated with the given vertex, and must be less than 24 cm away from the nominal interaction point in z and less than 2 cm away radially.

- Events which are determined to have anomolous energy depositions (noise) in the HCAL are rejected.
- Events with unphysically large laser correction values in the ECAL are rejected.

6.3.3 Electron selection

Electron candidates are reconstructed from a collection of electromagnetic clusters with matched pixel tracks. The momentum of the electron track is fitted using a Gaussian Sum Filter (GSF) [157] algorithm along its trajectory with the algorithm taking into account the possible emission of bremsstrahlung photons in the silicon tracker. The following selection criteria are applied:

- $p_T > 50$ GeV

- $|\eta| < 2.5$; we also exclude the barrel and endcap transition region ($1.4442 < |\eta_{sc}| < 1.556$, where η_{sc} is the position of the electron ECAL supercluster).
- Cut-based electron ID — "Tight" requirement (See Table. 6.7).
- Particle Flow based relative isolation, defined as the sum of the transverse momenta of all additional reconstructed particle candidates inside a cone around the electron $\Delta R = \sqrt{(\Delta\eta)^2 + (\Delta\phi)^2} < 0.3$ divided by the p_{T} of the electron, is required to be less than 0.10. Only charged particles originating from the primary vertex are considered. For neutral particles, the median energy density is determined event by event and the contribution within the isolation cone is subtracted.
- Events where the electron is determined to be from a converted photon are rejected.
- Transverse impact parameter of the electron with respect to the beamspot < 0.02 cm.
- ΔR between the electron and any jet in the event > 0.3.

We also apply a loose electron veto and reject events containing an additional loose electron satisfying:

- $p_{\mathrm{T}} > 20$ GeV
- $|\eta| < 2.5$
- Cut-based "veto" ID (See Table. 6.7)
- Particle Flow based relative isolation less than 0.15

Data-to-MC scale factors binned in electron p_{T} and η are derived using the tag and probe method and applied as corrections to the simulation (See Table 6.6).

6.3.4 Muon selection

Muons are reconstructed by combining tracks which are first reconstructed independently in the inner tracker and in the muon system. In the "Global Muon" reconstruction algorithm the two tracks are propagated to a common surface and matched to create a combined global track, which improves the momentum resolution for high p_{T} muons. Alternatively, the "Tracker Muon" reconstruction, which is more efficient for low p_{T} muons, considers all inner tracks as muon candidates, and the inner is track is propagated to the muon system to find at least one matching track segment. Events containing one muon with the following selection criteria are considered in the analysis:

- Reconstructed as a Global Muon
- $p_{\mathrm{T}} > 50$ GeV
- $|\eta| < 2.1$
- Transverse impact parameter of the muon with respect to the beamspot < 0.2 cm
- χ^2/ndof of the global track fit < 10
- Number of Muon chamber hits > 0
- Number of Pixel Hits > 0
- Number of chambers with matched segments > 1
- Longitudinal distance of closest approach of the tracker track with respect to the primary vertex $d_z < 5$ mm
- Number of tracker layers with hits > 5
- Particle Flow based relative isolation, defined for mouns similarly as for electrons, is required to be less than 0.12. Only charged particles from the primary vertex are considered for the isolation. For neutral particles, a correction is applied by subtracting the energy deposited in the isolation cone by charged particles not associated with the primary vertex, multiplied by a factor of 0.5 which is the approximate ratio of neutral to charged hadron production in the hadronization process of pile-up interactions [158].

- ΔR between the muon and any jet in the event > 0.3.

We also apply a loose muon veto and reject events containing an additional loose Global or Tracker muon satisfying:

- $p_{\mathrm{T}} > 10$ GeV
- $|\eta| < 2.4$
- Particle flow based relative isolation less than 0.2

Data-to-MC scale factors for the efficiency of the identification and isolation criteria binned in muon p_{T} and η are derived using the tag and probe method and applied as corrections to the simulation (See Table 6.6).

Table 6.6: Data-to-MC scale factors used for electrons and muons. The scale factors are shown separately for the trigger efficiencies and for the reconstruction and identification efficiencies.

Electron Scale Factors		
η range	Trigger	Reco. and Id.
$\lvert\eta\rvert <0.8$	0.973	0.988
$0.8< \lvert\eta\rvert <1.4442$	0.973	0.981
$1.556< \lvert\eta\rvert <2.0$	1.020	0.991
$2.0< \lvert\eta\rvert <2.5$	1.020	1.015
Muon Scale Factors		
η range	Trigger	Reco. and Id.
$\lvert\eta\rvert <0.9$	0.976	0.987
$0.9< \lvert\eta\rvert <1.2$	0.961	0.990
$1.2< \lvert\eta\rvert <2.1$	0.983	1.000

6.3.5 Jets

The analysis requires at least two Particle Flow jets that satisfy the following:

Variable	$\lvert\eta\rvert$ <1.4442		1.566< $\lvert\eta\rvert$ <2.5	
	Veto	Tight	Veto	Tight
$\lvert\Delta\eta\rvert$	<0.007	<0.004	<0.01	<0.005
$\lvert\Delta\phi\rvert$	<0.8	<0.03	<0.7	<0.02
$\sigma_{i\eta i\eta}$	<0.01	<0.01	<0.03	<0.03
H/E	<0.15	<0.12	—	<0.10
vertex d0	<0.04	<0.02	<0.04	<0.02
vertex dZ	<0.2	<0.1	<0.2	<0.1
$\lvert$1/E - 1/p$\rvert$	—	<0.05	—	<0.05

Table 6.7: Definition of "Veto" and "Tight" electron identification criteria. The matching variables $|\Delta\eta|$ and $|\Delta\phi|$ are between the supercluster position and the track direction at vertex extrapolated to ECAL assuming no radiation. The variable $\sigma_{i\eta i\eta}$ is the cluster shape covariance, and the variable H/E is the ratio of energy in HCAL behind the supercluster to supercluster energy. The vertex matching variables d0 and dZ are between the electron track and the primary vertex.

- Jets are reconstructed using the anti-k$_T$ algorithm [159] with a distance parameter of 0.5.
- Jet energy corrections are applied to correct for residual non-uniformity and non-linearity of the detector response and to subtract the average contribution from pileup interactions.
- Leading jet p_{T} (jet) > 120 GeV
- Second leading jet p_{T} (jet) > 40 GeV
- Additional jets p_{T} (jet) > 30 GeV
- Jet $|\eta| < 2.4$
- Loose particle flow jet identification [160].

For the simulated samples, the jet p_{T} is smeared ($\sim$ 5-29% depending on η) to account for the better jet energy resolution seen in the MC compared to data [160].

6.3.6 Missing Transverse Energy

- Particle Flow E_T^{miss} > 20 GeV

6.3.7 B-tagging

The properties of the bottom hadrons (relatively large masses, long lifetimes and daughter particles with hard momentum spectra) can be used to identify the hadronic jets into which a b quark fragments. This process of identifying jets originating from a b quark is known as b-tagging. For this analysis we use the Combined Secondary Vertex tagger with the medium operating point (CSVM) [161]. This algorithm combines secondary vertex information with track-based lifetime information when no secondary vertex is reconstructed to obtain the best b-tagging performance (high efficiency and low mistage rate). A data-to-MC b-tagging efficiency scale factor $SF_b = SF(p_T\ )$ and a mistag rate scale factor $SF_{light} = SF(p_T\ , \eta)$ for light jets are applied on a jet-by-jet basis to all b-jets, c-jets and light jets in the MC samples. The same method is used as the one described in Ref. [139].

Additionally, as reported in Ref. [162], a scale factor of 1.21 needs to be applied to W+b events, and a scale factor of 1.66 has to be applied to W+c events in order to match the fraction of W+ heavy flavor events observed in data. We apply these heavy flavor correction scale factors to any event where a b-quark and/or c-quark is present from a W boson decay. An additional correction in the light jet scale factor (0.83) is applied, as discussed in in section 6.4.1.

6.3.8 Pileup Reweighting

The effects of additional proton-proton interactions in each beam crossing (pileup) are modeled by superimposing extra minimum-bias interactions onto simulated events, with the distribution of the number of pileup interactions matching that in data. Good agreement between data and MC is seen after reweighting (see Fig. 6.4). We use a minimum bias cross-section of 69.3 mb as the nominal value, and also use 73.5 mb as a systematic uncertainty.

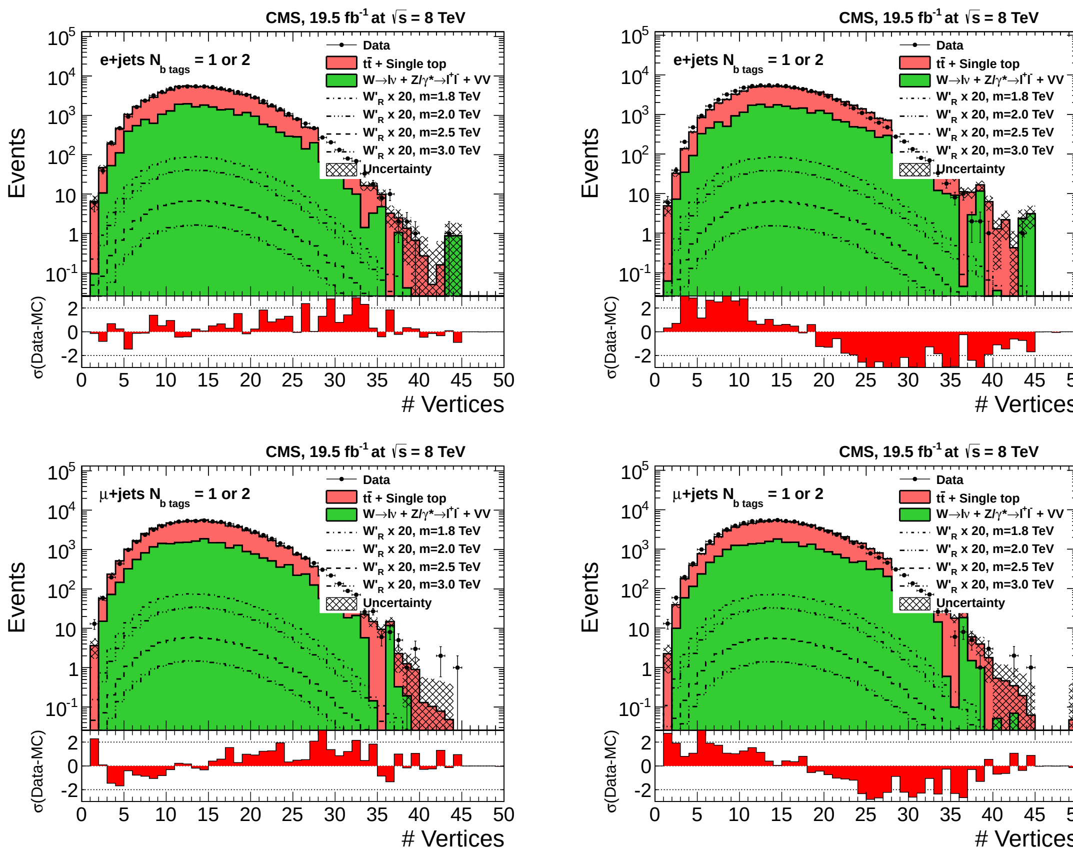

Figure 6.4: A comparison of the number of primary vertices measured in data and MC for a minimum bias cross-section of 69.3 mb (left) and 73.5 mb (right) for the electron (top) and muon (bottom) samples.

6.4 Background Modeling

6.4.1 W+Jets Modeling

The W+jets background is estimated using Monte Carlo events generated with MADGRAPH [163]. Before requiring a b-tagging criteria, the overall W+jets yield is normalized to the NNLO cross-section. The fraction of heavy flavor (W+b, W+c) events is then scaled by an additional empirical correction derived using lepton+jets samples with various jet multiplicities [162]. This empirical correction was derived for events with somewhat different topology compared to our selection. In order to check the validity of these scale factors we look at two samples: events with zero b-tagged jets (0 b-tags sample) and the inclusive sample after all the selection criteria, except any b-tagging requirement (preselection sample). The 0 b-tags sample is completely independent from our signal sample, which requires at least one b-tagged jet, and is dominated by W+light jets. The preselection sample is W+jets dominated, and includes a significant fraction of W+b and W+c events. The signal fraction in these samples is negligible. After applying the empirical corrections from Ref. [162], we observe a residual difference between the data and the background estimate. By comparing MC prediction for W+jets events with data in the 0 b-tags and preselection samples, through an iterative process, we extract W+light jets and heavy flavor jets scale factors. We start by estimating the W+light jet fraction using the 0 b-tag sample. This sample also includes a small fraction of W+b and W+c events. For the first iteration we include all other background contributions according to the nominal predictions. That is for $t\bar{t}$, and single top we use the theoretical cross-sections and for W+b and W+c we use both theoretical cross-sections and scale factors from Ref. [162]. The W+light jet scale factor obtained is then used in the pre b-tag sample where we determine the heavy flavor fraction scale factor. We use these heavy flavor factors in the 0 b-tag sample again and refine our estimate of the W+light jet scale factor, which can then, in turn, refine our heavy flavor estimate in the pre b-tag sample.

We find that, for our selection, the W+light jets contribution needs to be reduced by a factor of 0.83, whereas the W+bb and W+cc contribution does not need to be adjusted relative to the corrections derived in Ref. [162]. By taking into account the b-tagging uncertainty and uncertainties on other backgrounds, we assign an uncertainty of 13% on the W+light jets scale factor, and 15% on the heavy flavor scale factor. Given that the electron sample may suffer from a separate category of background, namely QCD multijet production, the scale factors are derived in the muon+jets sample and applied to both samples. The heavy flavor scale factor obtained is within the uncertainties for the heavy flavor corrections already applied from Ref. [162] and Ref. [139]. Figure 6.5 shows example distributions where one can see an improvement after applying these data driven scale factors.

W+Jets Shape

Events with 0 b-tagged jets that satisfy all other selection criteria are expected to originate predominantly from the W+jets background. These events can be used to verify the shape of the W+jets background in data. Figure 6.6 shows the comparison of the invariant mass with 0 b-tagged jets derived from the data to the same distribution in the W+jets Monte Carlo sample. The contributions of the other backgrounds are corrected for by subtracting them from the data. To demonstrate that the W+jets background shape is independent of the number of b-tagged jets, the mass distribution with no b-tagged jets is compared to that with one or more b-tagged jets. This comparison is shown in Figure 6.7.

6.4.2 $\mathrm{t\bar{t}}$ Modeling

Top-Quark p_{T} Shape

The top-quark p_{T} distribution in data is not well modeled by the simulation in both MADGRAPH and POWHEG. We reweight the MADGRAPH sample using an empirical function based on the $\mathrm{t\bar{t}}$ differential cross section measured in Refs. [164, 165]. An empirical function to reweight the top-quark p_{T} distribution to match the observed data is applied to the generator level quantities and is given by:

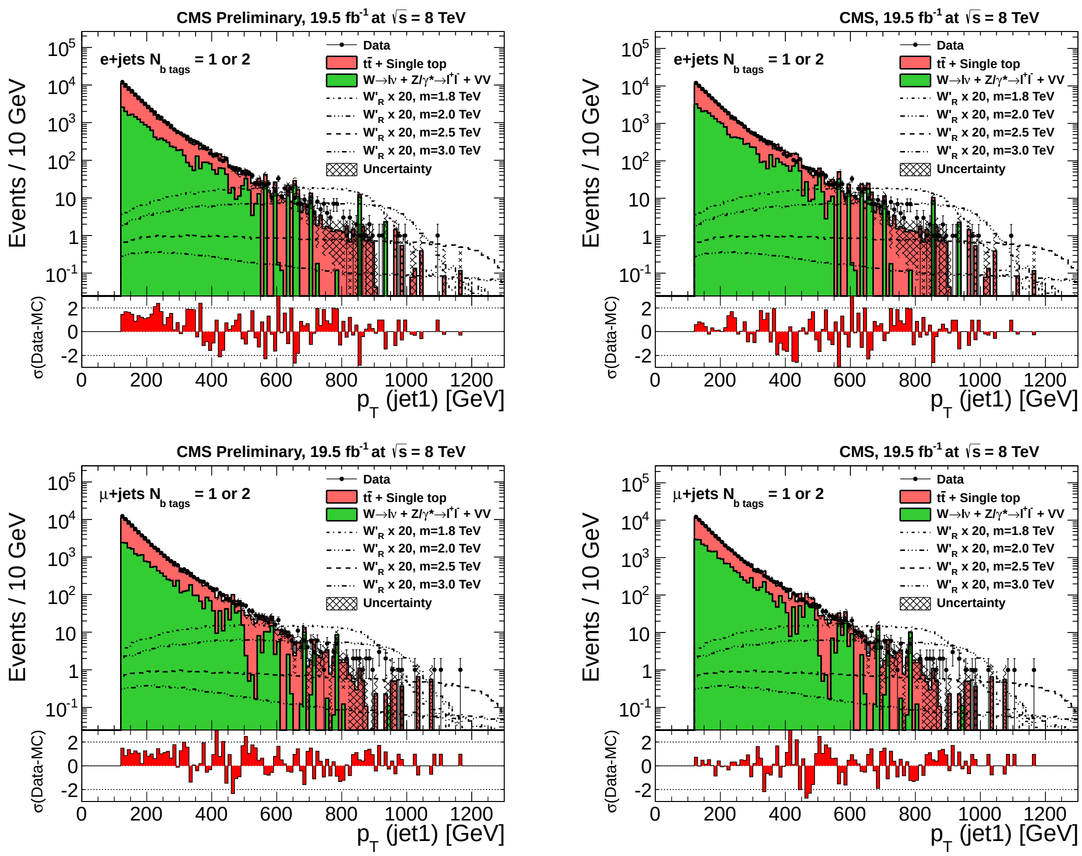

Figure 6.5: Distributions showing improvement in the background modeling after applying the data driven W+jets scale factors. Left: p_{T} (leading jet) for the electron (top) and muon (bottom) samples in events with at least one b-tagged jet. Right: the same distributions after applying the scale factor.

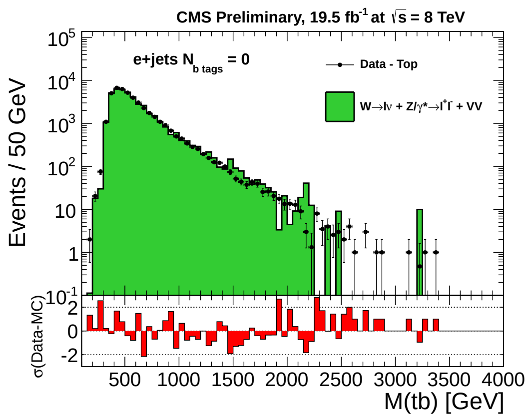

Figure 6.6: Distributions of the tb invariant mass the in the electron (left) and muon (right) samples comparing the data-driven estimate of the W+jets background shape to the W+jets MC.

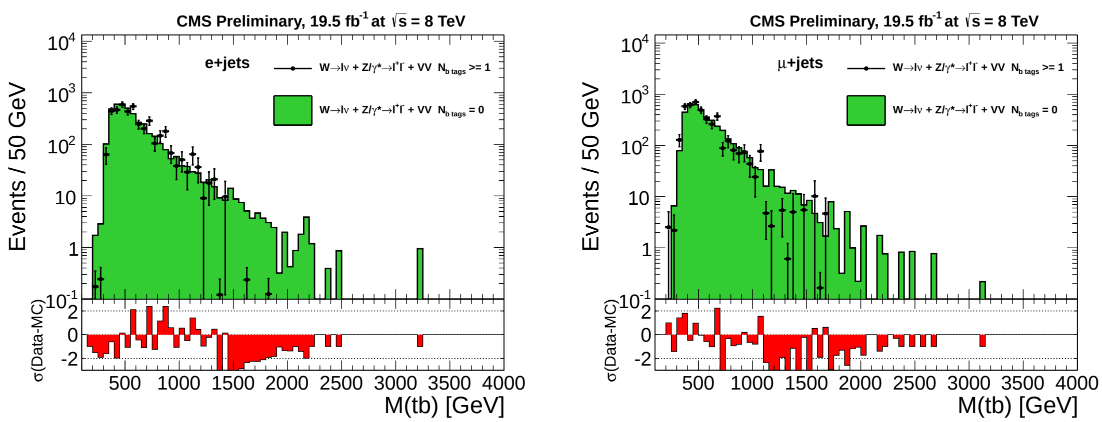

Figure 6.7: A comparison of the tb invariant mass in events with no b-tagged jets and in events with one or more b-tagged jets. The events for both distributions are from the W+jets Monte Carlo sample. The electron channel is on the left and the muon channel is on the right.

$$w = \sqrt{\left(e^{0.156-0.00137\cdot p_T^t}\right)\left(e^{0.156-0.00137\cdot p_T^{\bar{t}}}\right)} \quad (6.2)$$

In order to verify the applicability of these weights in a different kinematic region, we perform an independent "reco-level" study of the top-quark p_{T} distribution. We define a control region in data which is dominated by $\mathrm{t\bar{t}}$ events in order to reweight the simulation to match the observed distribution. The selection criteria which define the control region are $N_{jets} \geq 4$,$N_{b-tags} \geq 2$, and $400 < \mathrm{M(tb)} < 750$ GeV. The requirement on M(tb) ensures small (if any) signal contamination. In this region we observe 15956 total events in the electron and muon channels combined. Of these events, 98% are expected to originate from $\mathrm{t\bar{t}}$ and single-top events, and a potential 800 GeV W′ signal would account for less than 1% of the total events. We perform a fit to the ratio of data to expected background events using both a Landau and linear function. The results are shown in Fig. 6.8. The top-quark p_{T} and M(tb) distributions in the signal region after applying the generator level reweighting and the "reco-level" reweighting are in very good agreement. We reweight the $\mathrm{t\bar{t}}$ samples using the generator-level reweighting, and use the unweighted distribution as a systematic uncertainty in the final limit setting. Using the "reco-level" reweighting as the central value has no significant effect on the final result compared to using the generator-level reweighting.

6.4.3 Kinematic Distributions

Several relevant kinematic distributions after the event selection and data-driven corrections to the W+jets and $\mathrm{t\bar{t}}$ modeling described above are shown in Figs. 6.9, 6.10, 6.11, and 6.12.

6.5 Event Reconstruction

The distinguishing feature of a W′ signal is a narrow resonance structure in the tb invariant-mass spectrum. The tb invariant is reconstructed from the combination of the charged lepton, the neutrino, the jet which gives the best top-quark mass reconstruction, and the highest-p_{T} jet in the event that is not associated with the top quark. The xy components of the neutrino momentum are obtained from the missing transverse energy. The z component

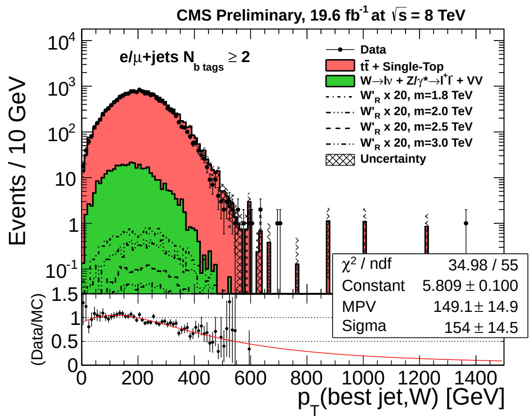

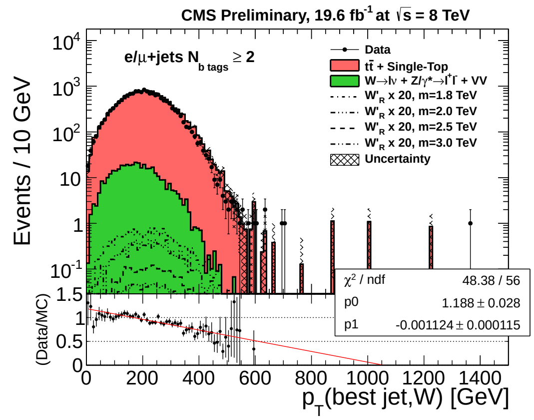

Figure 6.8: Distributions of the top-quark p_{T} spectrum in the $\mathrm{t\bar{t}}$ dominated control region. The left plot shows a fit to the data/MC ratio using a Landau function, and the right plot shows the fit to a linear function. The Landau function fit is used to reweight the $\mathrm{t\bar{t}}$ samples, and invariant mass distributions obtained using a reweighting based on the linear fit and the original distribution without any reweighting are used as systematic uncertainties on the $\mathrm{t\bar{t}}$ shape.

is calculated by constraining the invariant mass of the lepton-neutrino pair to the W-boson mass (80.4 GeV). This constraint leads to a quadratic equation in p_z^ν. In the case of two real solutions, both of the solutions are used to reconstruct the W-boson candidates. In the case of complex solutions, the real part is assigned to p_z^ν and the imaginary part is forced to zero by relaxing the W-boson mass constraint and recomputing p_{T}^ν. The p_{T}^ν solution that gives the invariant mass of the lepton-neutrino pair closest to 80.4 GeV is chosen, resulting in a single W-boson candidate. Top-quark candidates are then reconstructed using the W-boson candidate(s) and all of the selected jets in the event and the top-quark candidate with mass closest to 172.5 GeV is chosen. The W′-boson candidate is obtained by combining the best top-quark candidate with the highest-p_{T} jet, excluding the one used for the best top-quark candidate.

We further apply three additional criteria which are imposed to improve the signal-to-background discrimination: we require the p_{T} of the best top-quark candidate $p_{\mathrm{T}}^{\mathrm{top}} >$ 85 GeV, the p_{T} of the vector sum of the two leading jets $p_{\mathrm{T}}^{\mathrm{jet1,jet2}} > 140$ GeV, and the

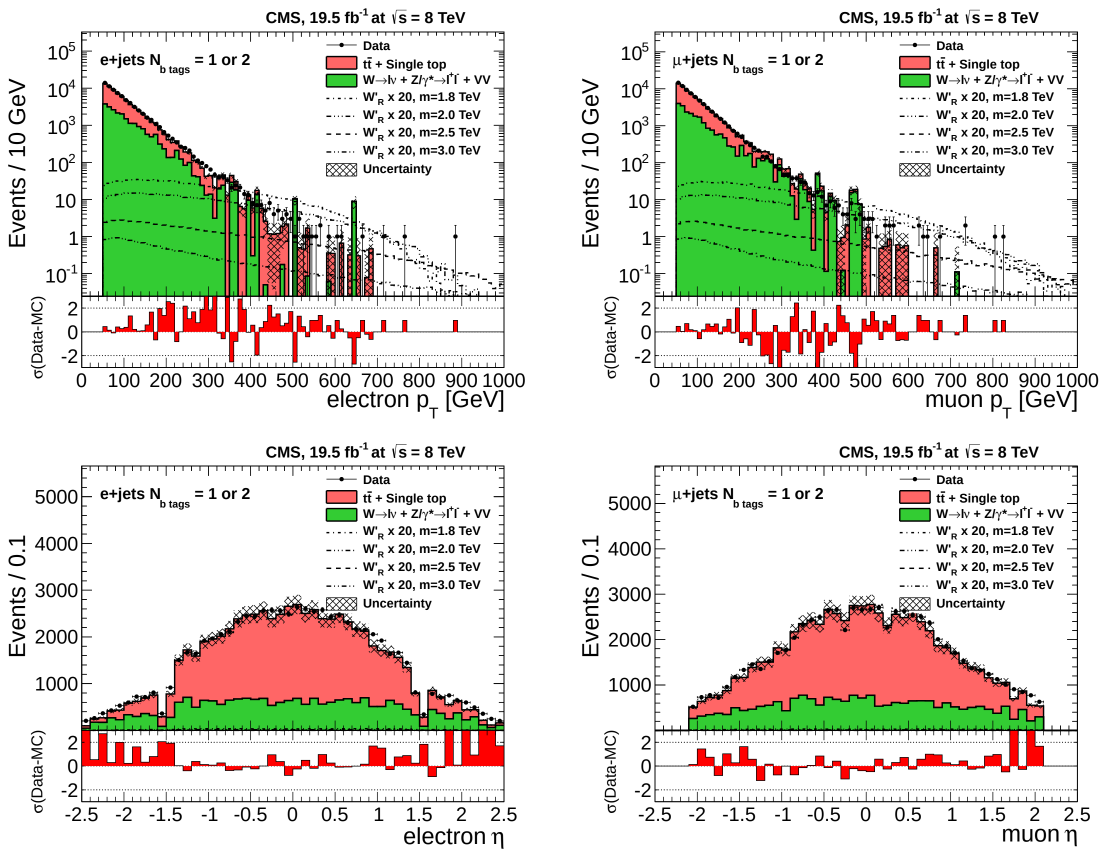

Figure 6.9: The reconstruced lepton p_T (top) and η (bottom) distributions in data and MC for the electron (left) and muon (right) samples.

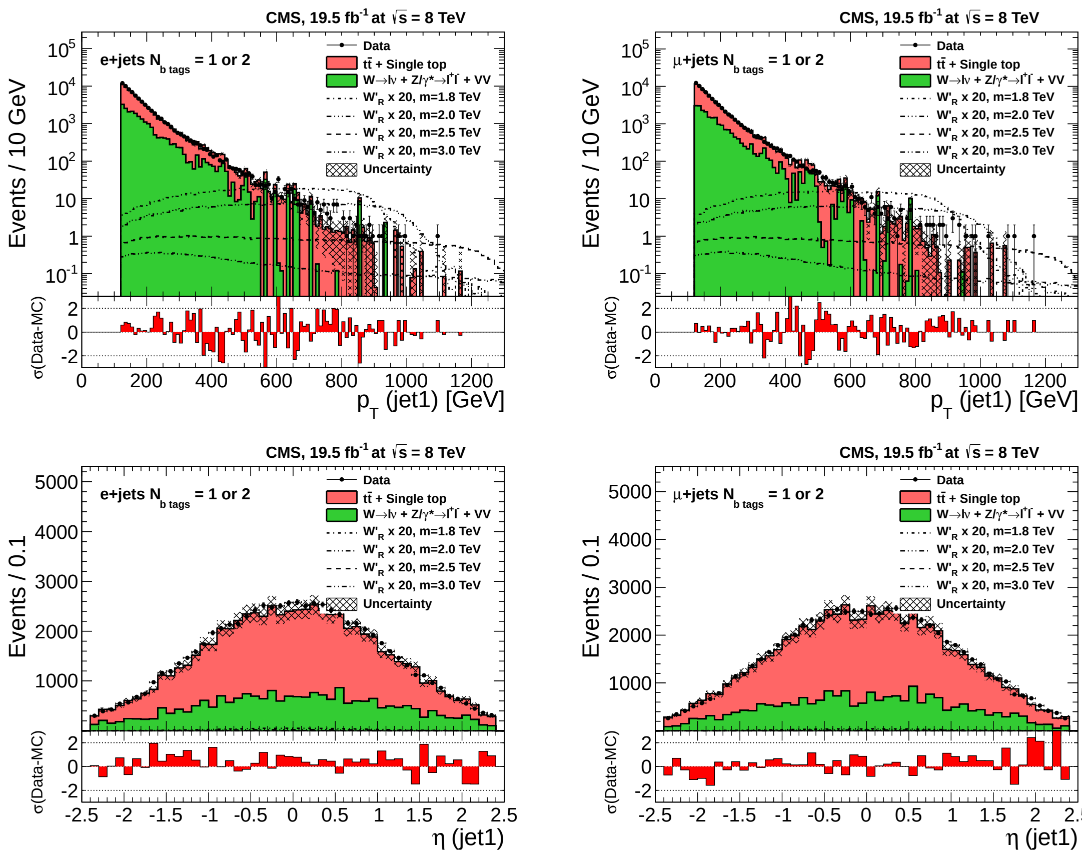

Figure 6.10: The reconstructed leading jet p_{T} (top) and η (bottom) distributions in data and MC for the electron (left) and muon (right) samples.

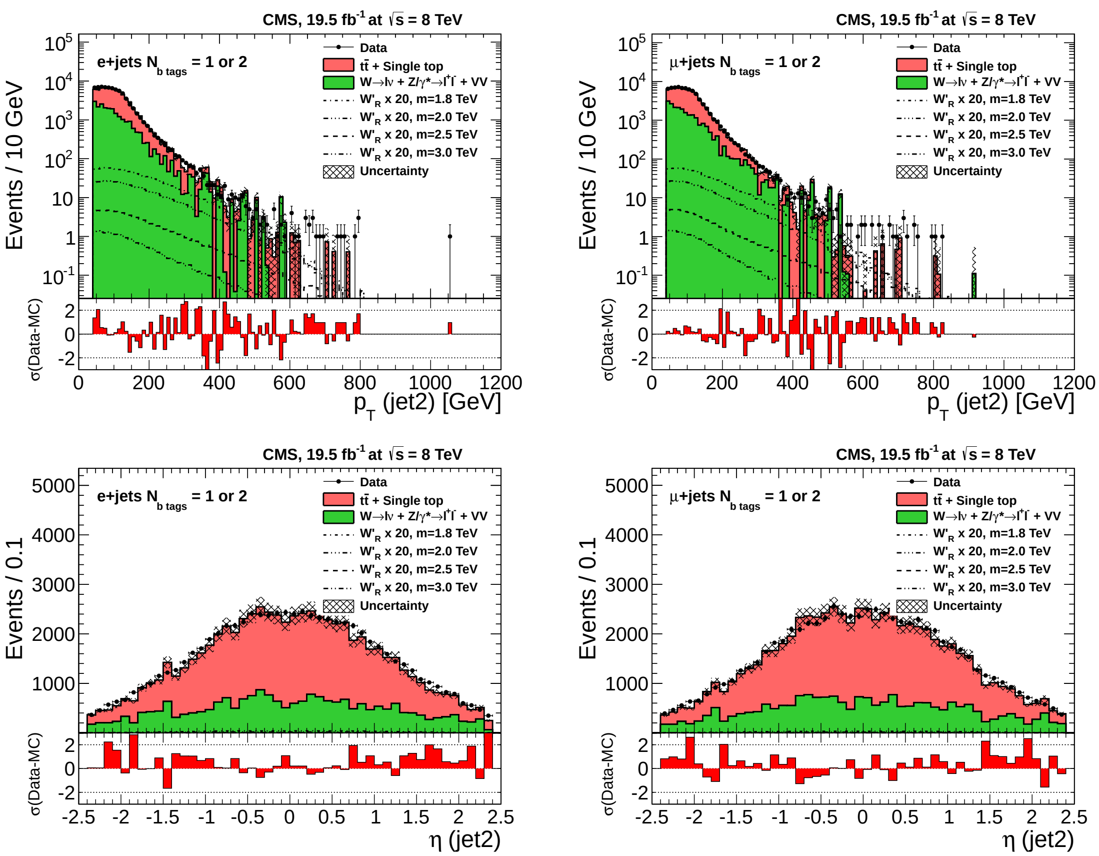

Figure 6.11: The reconstructed second leading jet p_{T} (top) and η (bottom) distributions in data and MC for the electron (left) and muon (right) samples.

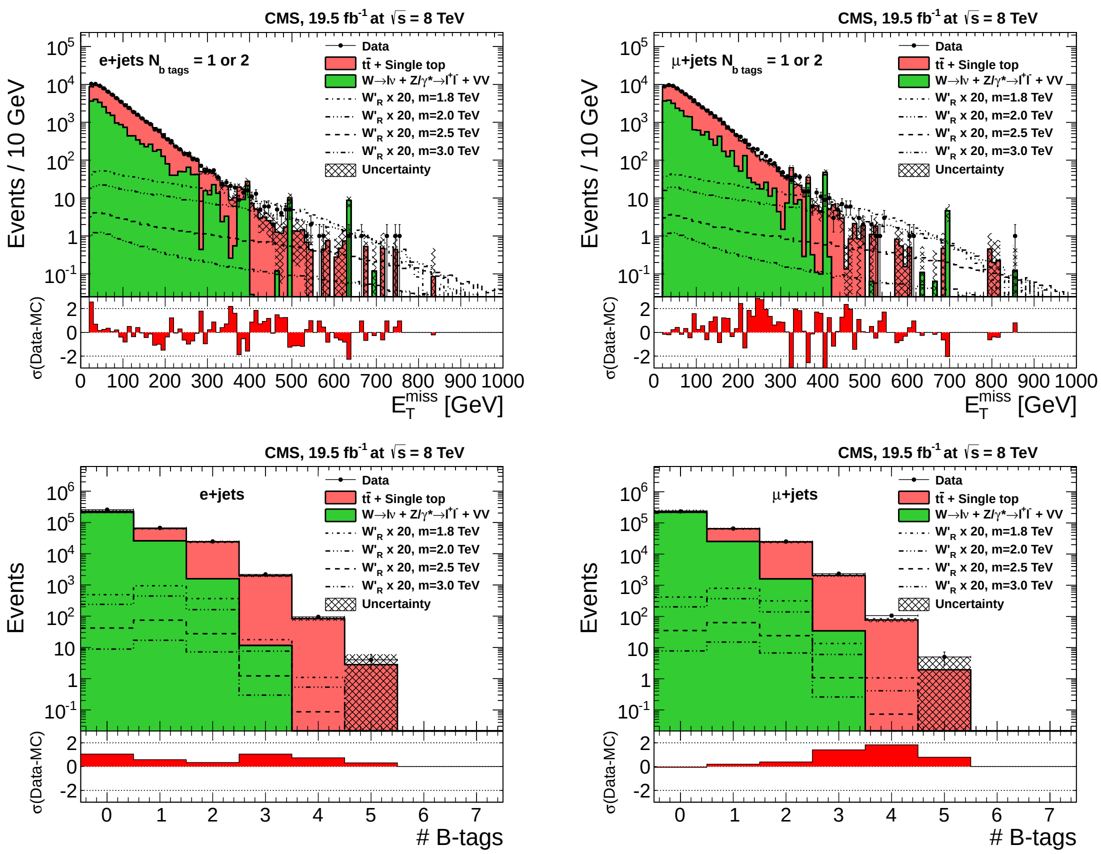

Figure 6.12: The reconstructed E_T^{miss} (top) and b-tag multiplicity (bottom) distributions in data and MC for the electron (left) and muon (right) samples.

mass of the best top-quark candidate with 130 GeV < M(t) < 210 GeV. These values were optimized by simultaneously varying the thresholds for the selection and running the full limit setting procedure, described in Section 6.7. The thresholds chosen are those which maximized the expected sensitivity. The application of these selection criteria improves the signal-to-background discrimination. These distributions are shown in Figs. 6.13, 6.14, and 6.15

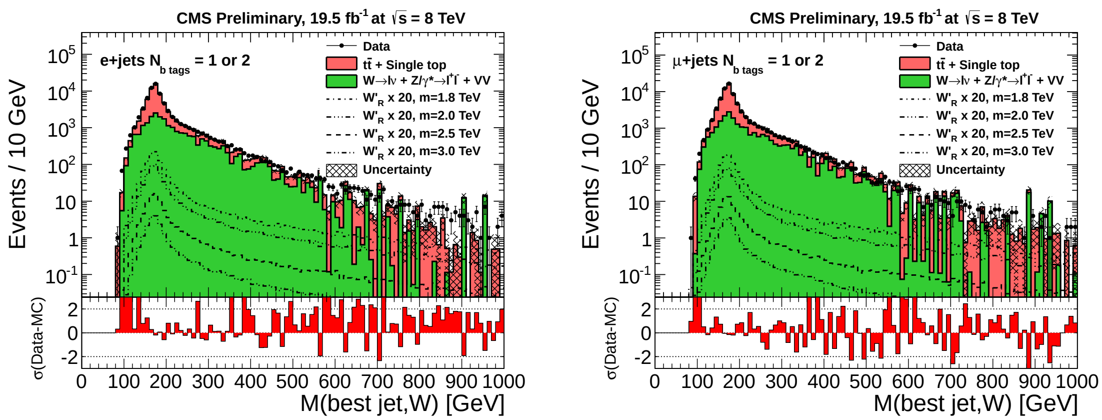

Figure 6.13: The reconstructed M(t) distributions in Data and MC for the electron (left) and muon (right) channels

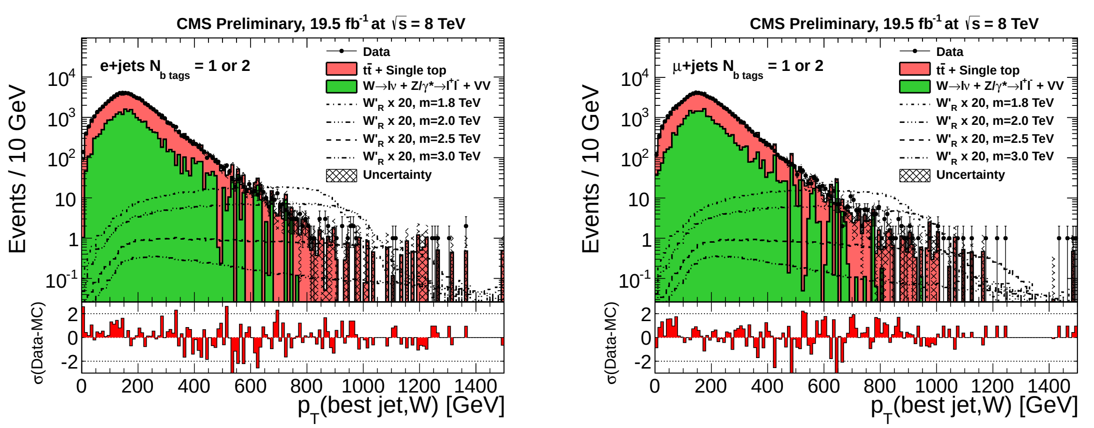

Figure 6.14: The reconstructed $p_{\mathrm{T}}^{\mathrm{top}}$ distributions in Data and MC for the electron (left) and muon (right) channels

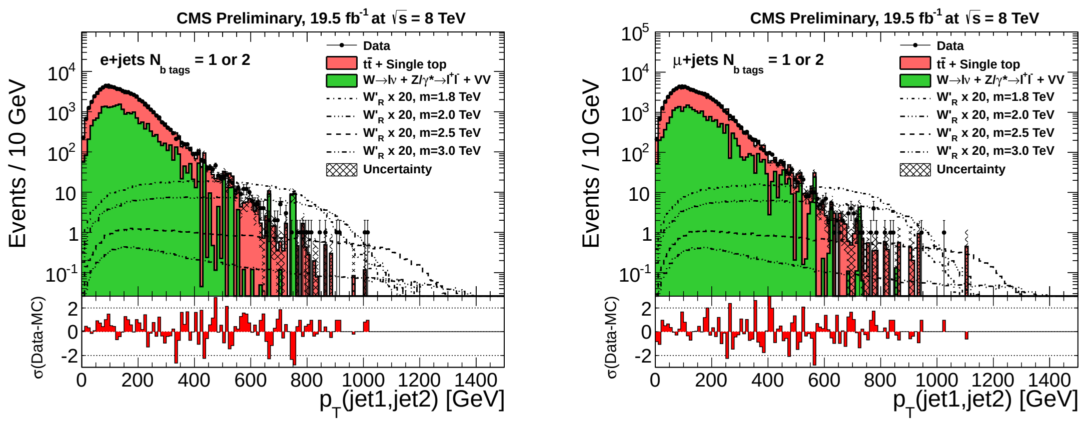

Figure 6.15: The reconstructed $p_{\mathrm{T}}^{\mathrm{jet1,jet2}}$ distributions in Data and MC for the electron (left) and muon (right) channels

Due to the low statistics in the W+jets sample at high mass after requiring at least one b-tagged jet, we use the shape of the preselection sample scaled to the expected ≥ 1 b-tag event yield as the final template. The shape of the two samples has been checked to be nearly identical.

Fig. 6.16 shows the reconstructed tb invariant mass distribution for our data and W$'$ signals generated at four different mass values (1800, 2000, 2500, and 3000 GeV), and Fig. 6.17 is the same distribution after the additional selection criteria described above. Fig. 6.18 shows the the distribution with the W+jets shape taken from the preselection sample as described above. Also included in the plots are the main background contributions.

The number of events remaining with one and two b-tagged jets after the preselection and final selection are listed in Table 6.8. The yields measured in data and those predicted from simulation agree within the statistical and systematic uncertainties, which are described in the following section.

6.6 Systematic Uncertainties

Systematic uncertainties were evaluated in two ways:

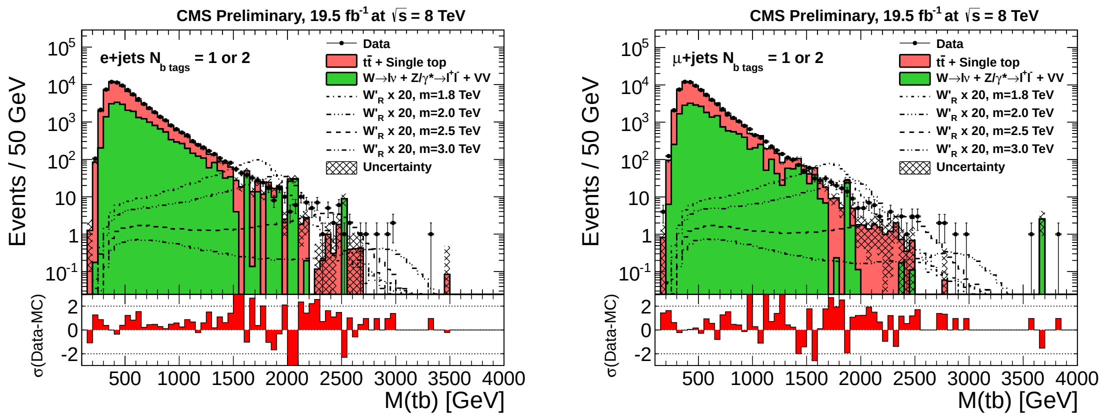

Figure 6.16: Reconstructed tb invariant mass distributions Events with electrons (muons) are shown on the left (right) for data, background and four different W'_R signal mass points. All events are required to have at least one b-tagged jet.

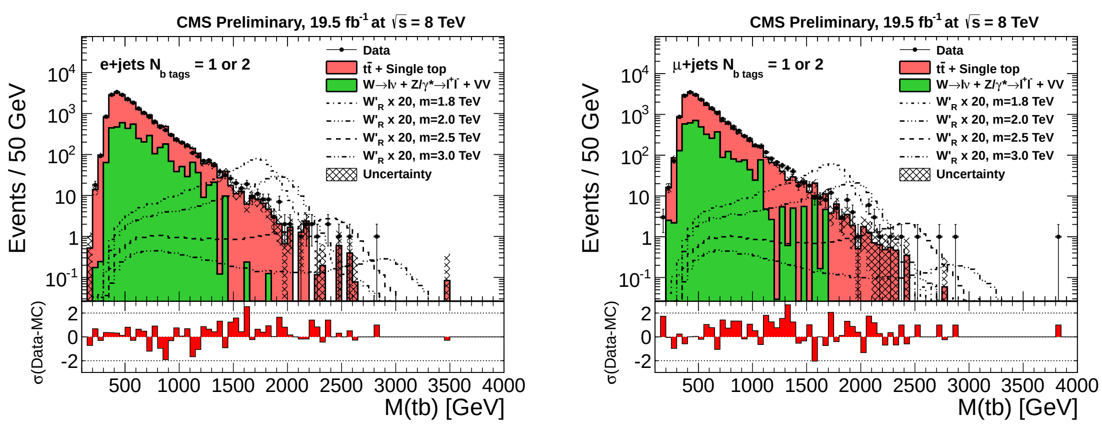

Figure 6.17: Reconstructed tb invariant mass distributions with the additional requirements $p_T^{\text{jet1,jet2}} > 140$ GeV, $p_T^{\text{top}} > 85$ GeV, and 130 GeV $<$ M(t) $<$ 210 GeV. Events with electrons (muons) are shown on the left (right) for data, background and four different W'_R signal mass points. All events are required to have at least one b-tagged jet.

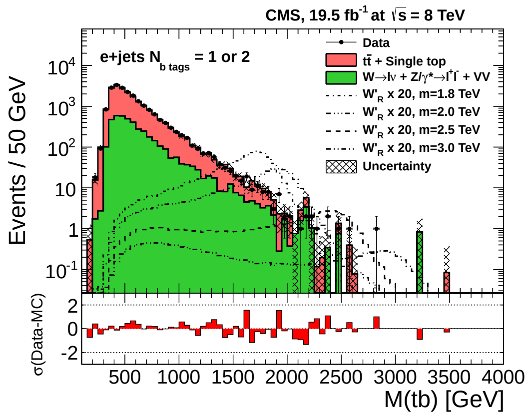

Figure 6.18: Reconstructed tb invariant mass distributions with the additional requirements $p_{\mathrm{T}}^{\mathrm{jet1,jet2}} > 140$ GeV, $p_{\mathrm{T}}^{\mathrm{top}} > 85$ GeV, and 130 GeV $< \mathrm{M(t)} <$ 210 GeV. Events with electrons (muons) are shown on the left (right) for data, background and four different W'_{R} signal mass points. All events are required to have at least one b-tagged jet. For the W+jets distribution, the preselection distribution scaled to the ≥ 1 b-tag yield is shown.

- Uncertainty on the normalization:

  This category includes uncertainties in the integrated luminosity, theoretical cross-sections and branching fractions, object identification efficiencies, and trigger efficiencies. In the limit estimation, these are defined through log-normal priors based on their mean values and their uncertainties.

- Uncertainties that also change the shape of the distributions:

  This category includes the uncertainty from the jet energy scale, jet energy resolution, b-tagging, light quark mistagging efficiencies, and event pileup conditions. These were evaluated by raising and lowering the jet energy scale correction (of order 2-3% as a function of jet p_{T} and η), the jet energy resolution (by 6-10%, depending on the jet p_{T} and η), or the b-tag efficiency and mistag rate scale factors by one standard deviation and repeating the analysis. For the W+jets samples, uncertainties relating to the extraction of the light- (13%) and heavy-flavor (15%) scale factors from data are included [161]. For the $\mathrm{t\bar{t}}$ background, the invariant mass distribution before

Table 6.8: Number of selected data, signal, and background events. For the background samples, the number of expected events is computed corresponding to an integrated luminosity of 19.5 fb^{-1}. The final two columns for each sample include the following selections: $p_{\mathrm{T}}{}^{\mathrm{t}} > 85$ GeV, $p_{\mathrm{T}}{}^{\mathrm{jet1,jet2}} > 140$ GeV, $130 < \mathrm{M(t)} < 210$ GeV. The combined statistical and systematic uncertainty on the total background prediction is also shown. The standard model s-channel tb process contributes to the background only in the search for W'_{R} bosons due to its interference with the $\mathrm{W}'_{\mathrm{L}} \to \mathrm{tb}$ process. The number of events for the W'_{L} signal takes into account the interference with the SM s-channel tb process.

	Number of selected events							
	Electron sample				Muon sample			
	Preselection		Final selection		Preselection		Final selection	
Process	1 b-tag	2 b-tags	1 b-tag	2 b-tags	1 b-tag	2 b-tags	1 b-tag	2 b-tags
Signal:								
$\mathrm{M(W'_R)} = 1.8$ TeV	45.2	12.7	32.2	9.3	38.0	10.8	26.3	7.7
$\mathrm{M(W'_R)} = 2.0$ TeV	20.9	5.6	14.6	4.0	17.5	4.7	11.8	3.2
$\mathrm{M(W'_R)} = 2.5$ TeV	3.5	0.9	2.3	0.6	3.0	0.8	1.8	0.5
$\mathrm{M(W'_R)} = 3.0$ TeV	0.8	0.3	0.5	0.2	0.7	0.2	0.4	0.2
$\mathrm{M(W'_L)} = 1.8$ TeV	143.0	60.9	57.1	19.7	148.8	63.7	58.1	19.5
$\mathrm{M(W'_L)} = 2.0$ TeV	125.2	57.9	44.7	17.8	128.3	61.0	45.7	18.1
$\mathrm{M(W'_L)} = 2.5$ TeV	115.8	58.6	38.4	17.2	122.3	62.6	41.6	17.7
$\mathrm{M(W'_L)} = 3.0$ TeV	121.3	58.1	41.0	16.7	126.6	64.4	42.2	17.9
Background:								
$\mathrm{t\bar{t}}$	34561	7888	12383	1639	35349	8191	12610	1650
s-channel (tb)	175	93	58	28	196	102	63	32
t-channel (tqb)	2113	357	710	108	2275	373	747	114
tW-channel	2557	362	847	107	2645	372	861	113
$\mathrm{W}(\to \ell\nu)$+jets	19970	563	3636	99	19697	679	3704	62
$Z/\gamma^*(\to \ell\ell)$+jets	1484	83	260	10	1497	73	275	17
WW	205	9	47	3	219	7	47	2
Total bkg.	61065	9357	17942	1993	61877	9797	18307	1991
	±6188	±1504	±2514	±399	±6098	±1524	±2488	±400
Data	63050	9646	18175	2063	62955	9865	18558	2081
Total bkg. / Data	0.969	0.970	0.987	0.966	0.983	0.993	0.986	0.957
	±0.10	±0.16	±0.14	±0.19	±0.10	±0.15	±0.13	±0.19

the top-quark p_{T} reweighting described in section 6.4.2 is included as a systematic uncertainty. The variation of the renormalization and factorization scale Q^2 used in the strong coupling constant $\alpha_s(Q^2)$, and the jet-parton matching scale uncertainties in the MLM scheme [166] are evaluated for the $\mathrm{t\bar{t}}$ background sample. These uncertainties are evaluated by raising and lowering the corresponding parameters by one standard deviation (or in the case of the renormalization and factorization scale Q and the jet parton matching scale by a factor 2 and 0.5), and repeating the analysis. A bin-wise interpolation using a cubic spline between histogram templates at the different variations is performed and a nuisance parameter is associated to the interpolation and included in the limit estimation.

For the W+jets background jet energy resolution (J.E.R) and jet energy scale (J.E.S) systematics, the same procedure to form the final templates as described in Section 6.4.1 is used. For the b-tag systematic, we use the nominal preselection derived W+jets sample and normalize to the expected yields for the $\pm 1\sigma$ distributions. The uncertainty on the b-tag scale factor varies between 2% and 8% depending on the jet p_{T} . For jet p_{T} > 800 GeV, we use the scale factor at 800 GeV with twice the uncertainty since no scale factor has been derived in this kinematic region. Details of these uncertainties for the signal and background samples are shown in Table 6.9.

The process $\mathrm{W}' \rightarrow \mathrm{tb} \rightarrow \mathrm{Wbb}$ with $\mathrm{W} \rightarrow \tau\nu \rightarrow (e/\mu)\nu\nu$ has a small but non-negligible contribution to the analysis. In order to obtain high statistics in the e+jets and μ+jets samples, events with $\mathrm{W} \rightarrow \tau\nu$ are not included in the signal sample generation. The contribution from these events is estimated from the 7 TeV analysis by determining the fraction of events in the final sample which originate from $\mathrm{W} \rightarrow \tau\nu \rightarrow (e/\mu)\nu\nu$ decays. This contribution is found to be 11.6% averaged over different W' masses, in both the electron and muon channels. The shape of the tb invariant mass spectrum is also found to be sufficiently similar between $\mathrm{W} \rightarrow \tau\nu \rightarrow (e/\mu)\nu\nu$ and $\mathrm{W} \rightarrow (e/\mu)\nu$ decays, as shown in Fig. 6.19. Therefore, the contribution from τ decays can be accounted for by scaling the signal templates by an additional 11.6%. A systematic uncertainty on the signal efficiency for τ events of

2% is included which accounts for the spread in the efficiencies observed at all masses.

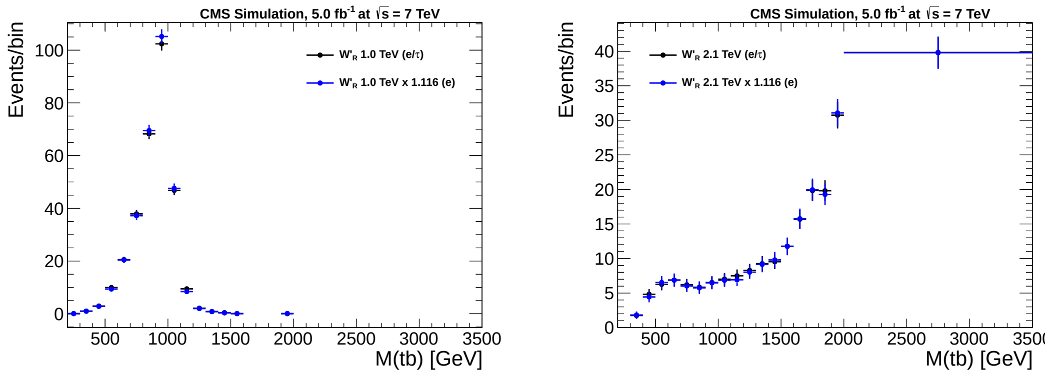

Figure 6.19: Comparison of W′ signal templates at 7 TeV for W→ $(e/\tau)\nu$ events and W→ $e\nu$ events only at two different W′ masses (left: M(W′)=1.0 TeV, right: M(W′)=2.1 TeV). The latter template is scaled by an additional factor of 11.6%.

Table 6.9: Systematic Uncertainties. For systematics with a (*) refer to Tables 6.10 and 6.11 for further information.

Source	Rate Uncertainty	Shape
Luminosity	2.6%	No
Trigger Efficiency	2%/1% (e/μ)	No
Lepton efficiencies	1%	No
$t\bar{t}$ and single top cross-section	8%	No
Jet Energy Scale	$\pm\sigma(p_T,\eta)(*)$	Yes
Jet Energy Resolution	$\pm\sigma(p_T,\eta)(*)$	Yes
b-tagging (CSVM)	$\pm\sigma(p_T,\eta)(*)$	Yes
c-tagging (CSVM)	$\pm\sigma(p_T,\eta)(*)$	Yes
light quark mis-tagging (CSVM)	$\pm\sigma(p_T,\eta)(*)$	Yes
Pileup	(*)	Yes
W+jets Heavy Flavor Fraction	(*)	Yes
W+jets Shape (data/MC diff using 0-btags)	No	Yes
$t\bar{t}$ jet-parton matching scale	(*)	Yes
$t\bar{t}$ renormalization and factorization scale	(*)	Yes
top-quark p_T reweighting	(*)	Yes

The percent difference in the number of events between the nominal and systematic samples for both μ+jets and e+jets is shown in Tables 6.10 and 6.11. The reconstructed tb invariant mass distribution of the total background for the nominal and $\pm 1\sigma$ variations are shown in Figures 6.20, 6.21, 6.22 and 6.23. The data and background distributions used for the limit setting procedure in the next section with the total uncertainty for each bin can be seen in Fig. 6.25.

Table 6.10: Fractional change in rate for systematic uncertainty sources which affect both shape and rate in the 1 b-tag channel.

	V+jets				$t\bar{t}$ + single-t			
	μ+jets		e+jets		μ+jets		e+jets	
Systematic	$+1\sigma$	-1σ	$+1\sigma$	-1σ	$+1\sigma$	-1σ	$+1\sigma$	-1σ
J.E.S.	1.077	0.9368	1.067	0.9569	1.032	0.9564	1.033	0.9557
J.E.R.	1.017	0.9969	1.023	0.9813	1.003	0.9966	1.001	0.9967
B-Tag	1.043	0.9402	1.039	0.9247	1.019	0.9819	1.018	0.98
Pileup	0.9991	—	0.9901	—	0.9949	—	0.9989	—
H.F.	1.083	0.9168	1.076	0.9237	—	—	—	—
Matching Scale	—	—	—	—	0.9785	1.015	0.9593	1.002
Q^2 Scale	—	—	—	—	0.9716	0.9952	0.9623	0.9838
top p_T reweighting	—	—	—	—	1.141	1	1.145	1

6.7 Results

6.7.1 Cross Section Limits for W'_{R}

The W′-boson mass distribution observed in the data and the prediction for the total expected background agree within statistical and systematic uncertainties. We set upper limits on the W′-boson production cross section for different W′-boson masses. The limits are computed using a Bayesian approach with a flat prior on the signal cross section with the THETA package [167]. The systematic uncertainties described in the previous section are treated as nuisance parameters and are marginalized using Markov Chain Monte Carlo method. Systematic uncertainties which affect both signal and background are considered

Table 6.11: Fractional change in rate for systematic uncertainty sources which affect both shape and rate in the 2 b-tag channel.

	V+jets				$t\bar{t}$ + single-t			
	μ+jets		e+jets		μ+jets		e+jets	
Systematic	$+1\sigma$	-1σ	$+1\sigma$	-1σ	$+1\sigma$	-1σ	$+1\sigma$	-1σ
J.E.S.	1.067	0.8038	1.192	1.015	1.054	0.9534	1.039	0.9377
J.E.R.	1.042	0.859	1.061	1.002	1.01	0.9991	0.9993	0.9858
B-Tag	1.165	0.8406	1.092	0.998	1.057	0.9311	1.056	0.949
Pileup	0.9832	—	0.9687	—	1.003	—	1.003	—
H.F.	1.116	0.8839	1.133	0.8668	—	—	—	—
Matching Scale	—	—	—	—	0.9644	1.006	0.9574	0.9687
Q^2 Scale	—	—	—	—	0.9812	0.9813	0.9215	0.9557
top p_T reweighting	—	—	—	—	1.158	1	1.162	1

to be fully correlated. In order to reduce the statistical uncertainty in the predicted event yields obtained from the simulated samples, we bin the invariant-mass distribution using one bin from 100 GeV to 300 GeV, 17 bins of 100 GeV width from 300 to 2000 GeV, and two additional bins from 2000 to 2200 GeV and from 2200 to 4000 GeV. Four categories are defined according to the lepton flavor (electron or muon) and b-tag multiplicity (one or two b-tagged jets) to improve the sensitivity of the analysis. The resulting distributions serve as the inputs to the limit setting procedure. The data, background and three different signal distributions can be seen in Figs. 6.26, 6.27 and 6.28.

The limit is based on the posterior probability defined by using all categories simultaneously. A binned likelihood is used to calculate upper limits on the signal production cross section times total leptonic branching fraction: $\sigma(\mathrm{pp} \to \mathrm{W}') \times \mathrm{BR}(\mathrm{W}' \to \mathrm{tb} \to \ell\nu\mathrm{bb})$, where $\ell = e/\mu/\tau$. The limit computation accounts for the effects of systematic uncertainties (discussed in Section 6.6) in the normalization and shape of the invariant-mass distributions, as well as statistical fluctuations in the background templates. Expected limits on the production cross section for each W'_{R}-boson mass are also computed as a measure of the sensitivity of the analysis.

In Figs. 6.29, 6.30 and 6.31, the solid black line denotes the observed limit and the red lines represent the predicted theoretical cross section times leptonic branching fraction. The lower mass limit is defined by the mass value corresponding to the intersection of the observed upper limit on the production cross section times leptonic branching fraction with the theoretical prediction. For W′ bosons with right-handed couplings to fermions the observed (expected) limit is 2.05 (2.02) TeV at 95% confidence level (CL). These limits also apply to a left-handed W′ boson when no interference with the SM is taken into account. Assuming heavy right-handed neutrinos ($\mathrm{M}(\nu_\mathrm{R}) > \mathrm{M}(\mathrm{W}')$), the observed (expected) limit is 2.13 (2.12) TeV at 95% CL.

6.7.2 Limits on coupling strengths

The effective Lagrangian given by Eq. 6.1 can be analyzed for arbitrary combinations of left-handed or right-handed coupling strengths [139]. The cross section for single-top-quark production in the presence of a W′ boson for any set of coupling values can be written in terms of the cross sections σ_L for purely left-handed couplings $(a^\mathrm{L}, a^\mathrm{R}) = (1, 0)$, σ_R for purely right-handed couplings $(a^\mathrm{L}, a^\mathrm{R}) = (0, 1)$, σ_LR for mixed couplings $(a^\mathrm{L}, a^\mathrm{R}) = (1, 1)$, and σ_SM for SM couplings $(a^\mathrm{L}, a^\mathrm{R}) = (0, 0)$. It is given by:

$$\begin{aligned}
\sigma &= \sigma_\mathrm{SM} + a^\mathrm{L}_{ud} a^\mathrm{L}_{tb} \left(\sigma_\mathrm{L} - \sigma_\mathrm{R} - \sigma_\mathrm{SM}\right) \\
&+ \left(\left(a^\mathrm{L}_{ud} a^\mathrm{L}_{tb}\right)^2 + \left(a^\mathrm{R}_{ud} a^\mathrm{R}_{tb}\right)^2\right) \sigma_\mathrm{R} \\
&+ \frac{1}{2}\left(\left(a^\mathrm{L}_{ud} a^\mathrm{R}_{tb}\right)^2 + \left(a^\mathrm{R}_{ud} a^\mathrm{L}_{tb}\right)^2\right) \left(\sigma_\mathrm{LR} - \sigma_\mathrm{L} - \sigma_\mathrm{R}\right).
\end{aligned} \tag{6.3}$$

We assume that the couplings to first-generation quarks, a_{ud}, that are important for the production of the W′ boson, and the couplings to third-generation quarks, a_{tb}, that are important for the decay of the W′ boson, are equal. For each value of a^L and a^R, the predicted invariant-mass distributions are obtained by combining the four event samples according to Eq. (6.3).

We vary both a^L and a^R in the range (0,1) with a step size of 0.1, for each M(W′). For each of these combinations of a^L, a^R, and M(W′), we determine the expected and observed

95% CL upper limits on the cross section and compare them to the corresponding theory prediction. If the limit is below the theory prediction, this point in $(a^{\mathrm{L}}, a^{\mathrm{R}}, \mathrm{M}(\mathrm{W}'))$ space is excluded. Figure 6.32 shows the excluded W'-boson mass for each point in the $(a^{\mathrm{L}}, a^{\mathrm{R}})$ plane. The observed (expected) mass limit for a W' boson with only left-handed couplings, including interference with the SM, is 1.84 (1.84) TeV. These constraints, as well as those presented Section 6.7.1, are the most stringent limits on W'-boson production in the tb decay channel obtained to date.

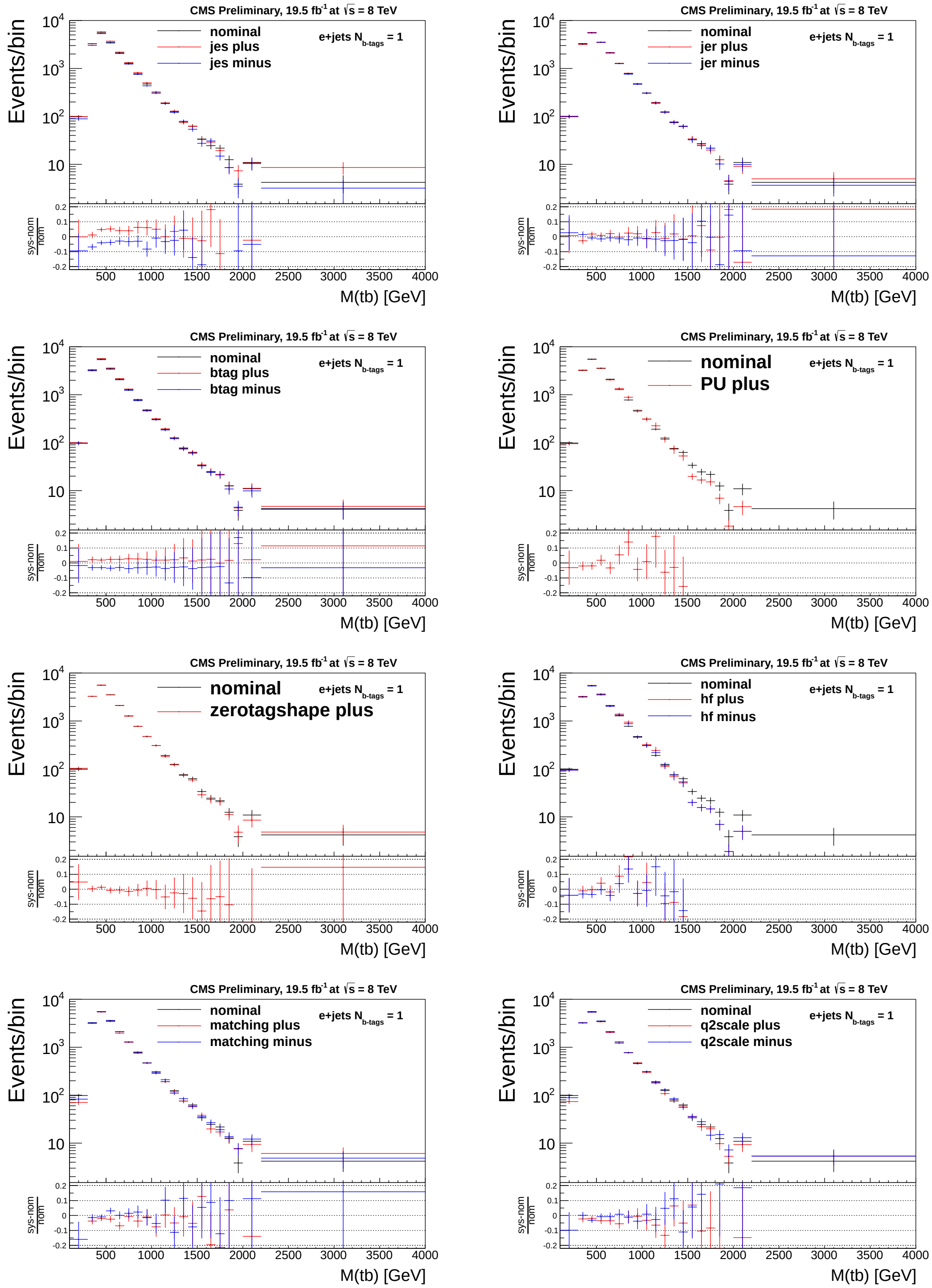

Figure 6.20: The reconstructed tb invariant mass distribution of the total background for the nominal (black), $+1\sigma$ (red), and -1σ (blue) variations for the 1 b-tag electron channel. Also shown is the bin-by-bin percent difference.

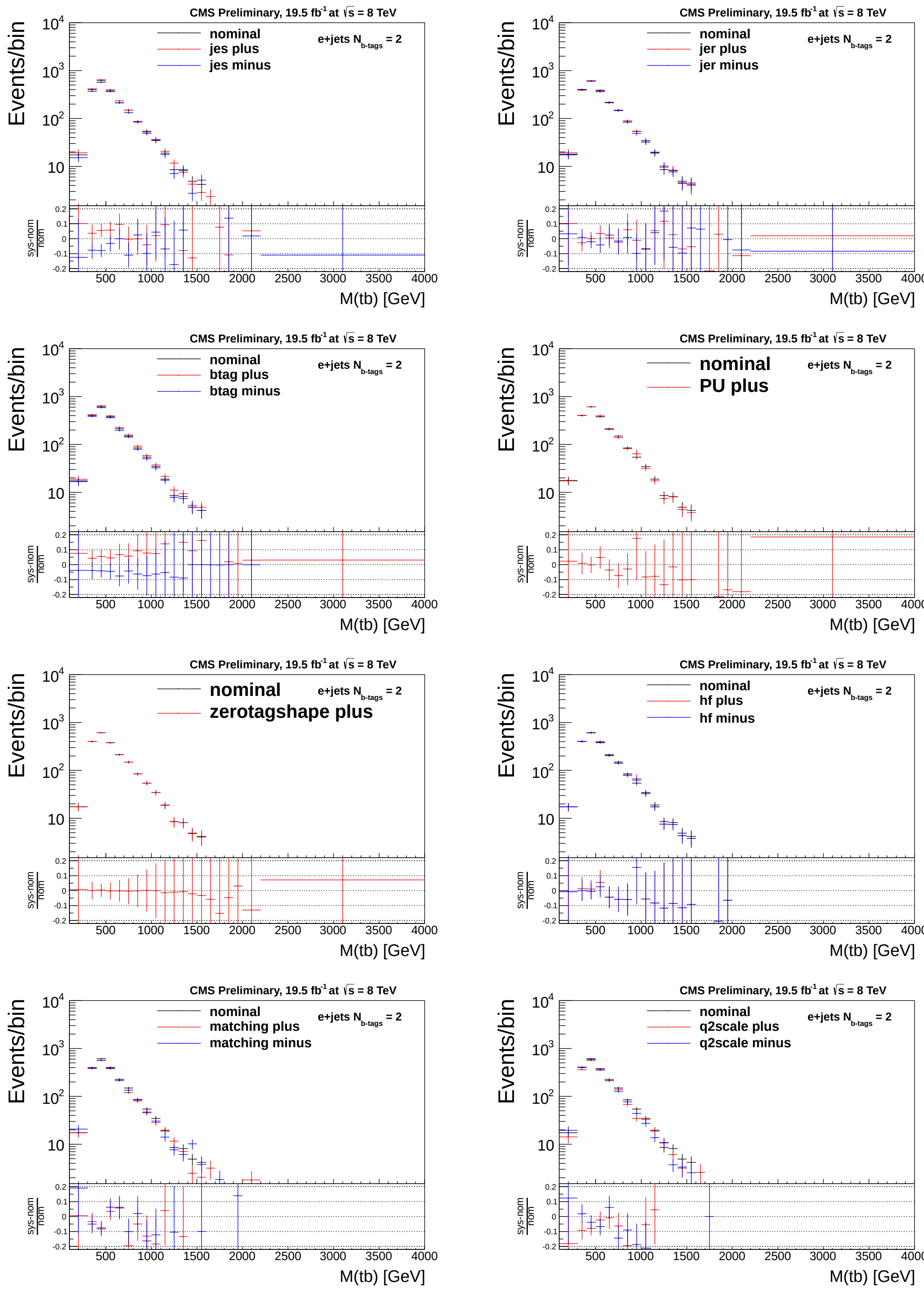

Figure 6.21: The reconstructed tb invariant mass distribution of the total background for the nominal (black), $+1\sigma$ (red), and -1σ (blue) variations for the 2 b-tag electron channel. Also shown is the bin-by-bin percent difference.

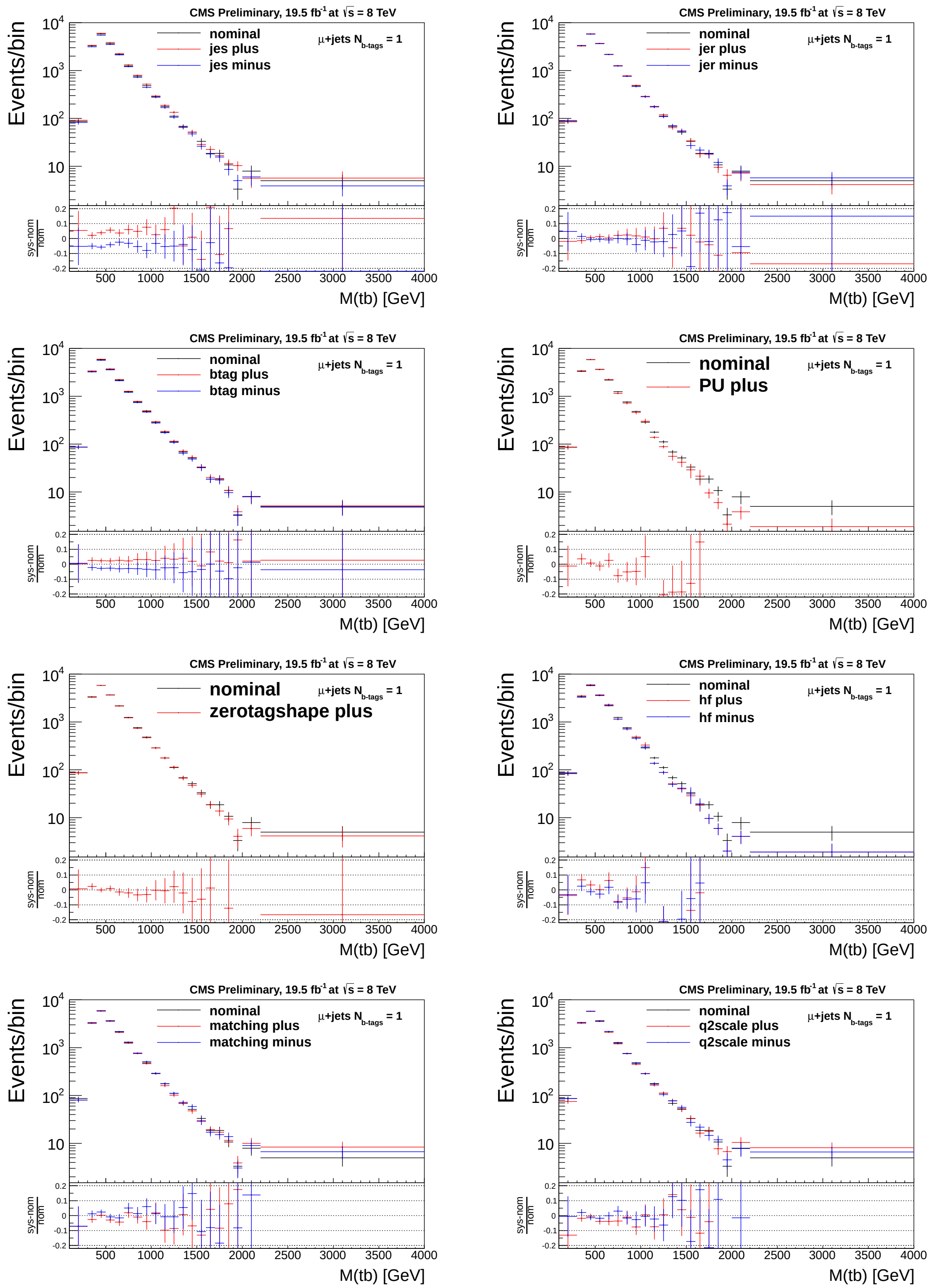

Figure 6.22: The reconstructed tb invariant mass distribution of the total background for the nominal (black), $+1\sigma$ (red), and -1σ (blue) variations for the 1 b-tag muon channel. Also shown is the bin-by-bin percent difference.

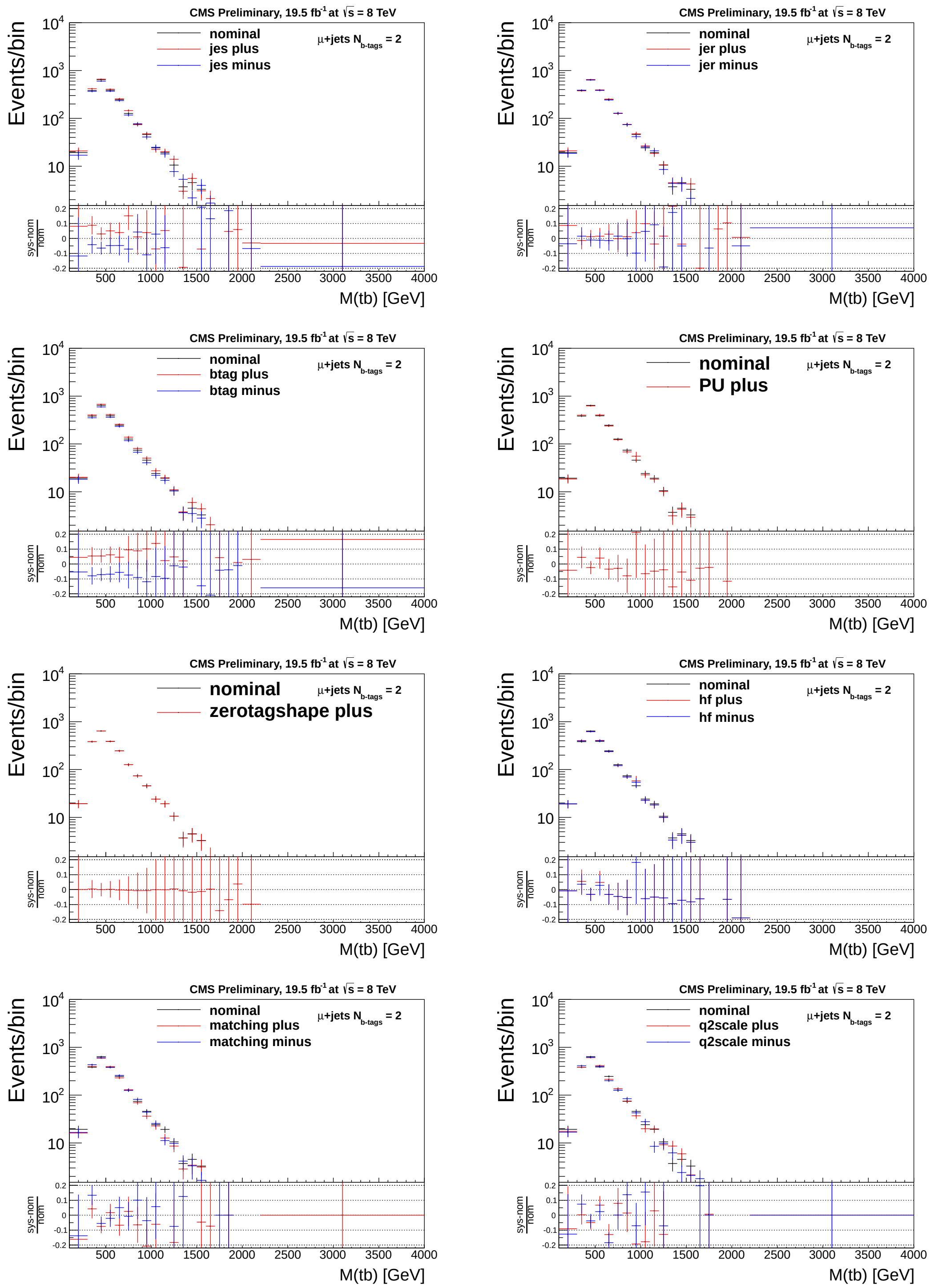

Figure 6.23: The reconstructed tb invariant mass distribution of the total background for the nominal (black), $+1\sigma$ (red), and -1σ (blue) variations for the 2 b-tag muon channel. Also shown is the bin-by-bin percent difference.

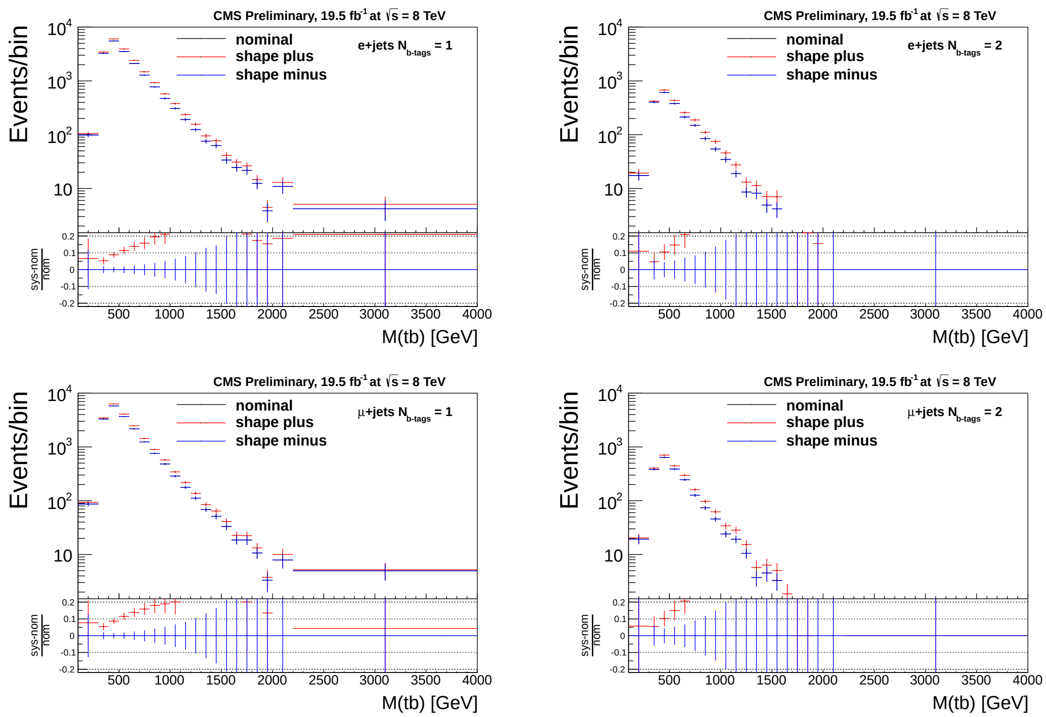

Figure 6.24: The reconstructed tb invariant mass distribution of the total background for the nominal (black), $+1\sigma$ (red), and -1σ (blue) variations due to the top-quark p_{T} shape systematic on the $\mathrm{t\bar{t}}$background shape. Also shown is the bin-by-bin percent difference.

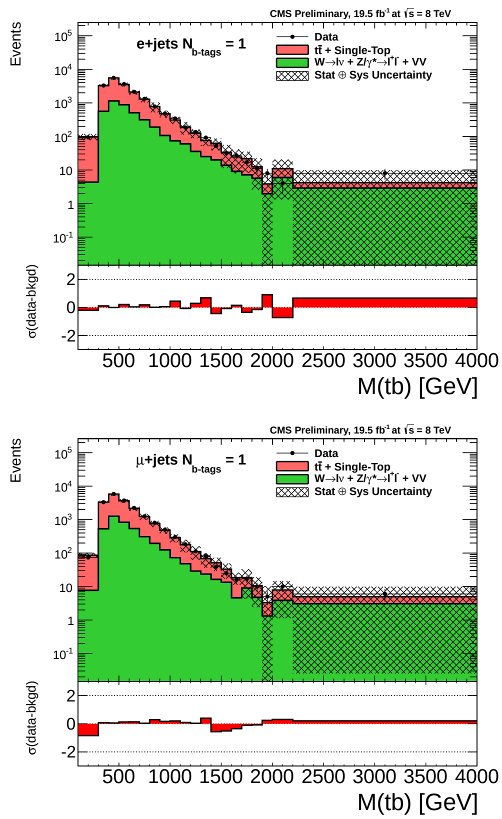

Figure 6.25: The templates used for the limit setting, including the total statistical plus systematic uncertainty on the background. The electron channel is in the top row and the muon channel is in the bottom row, with the 1 b-tag templates on the left and the 2 b-tag templates on the right.

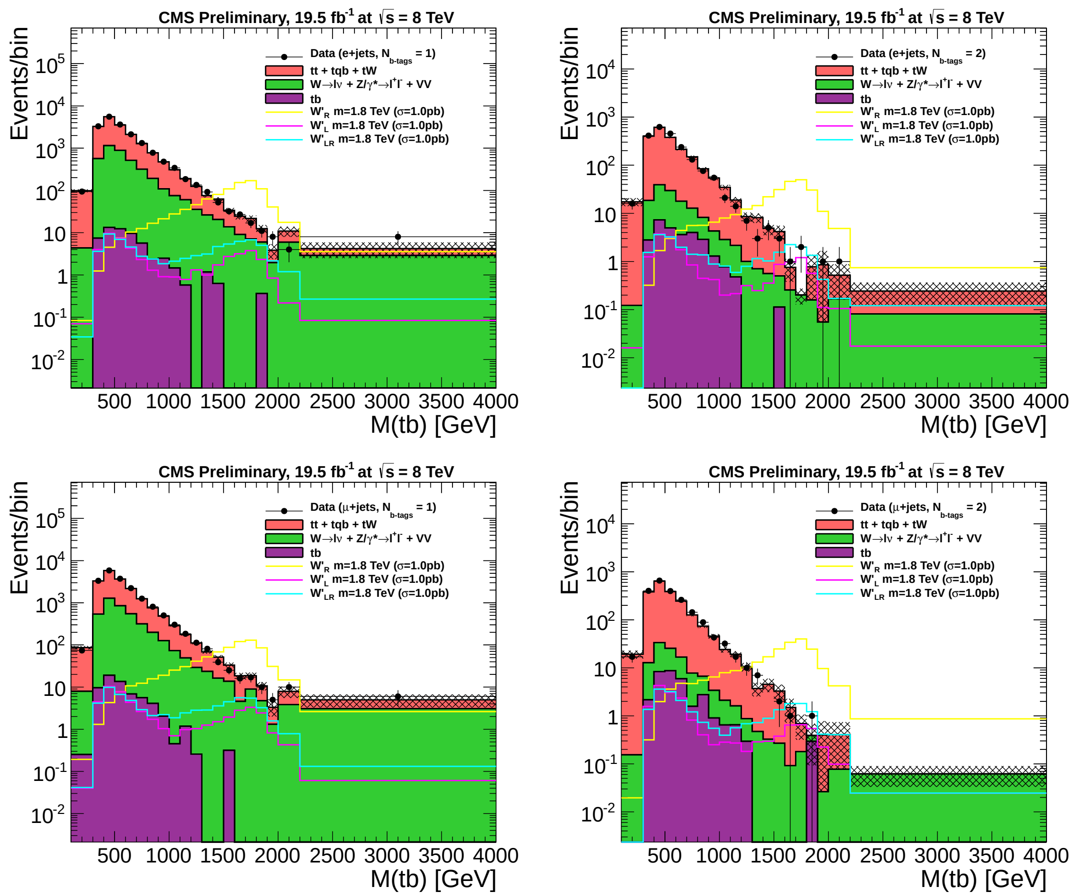

Figure 6.26: The templates used for the limit setting, including Left, Right, and Mixed W′ samples for M(W′)=1.8 TeV. The electron channel is on the top and the muon channel is on the bottom, with the 1 b-tag templates on the left and the 2 b-tag templates on the right. The uncertainty band is the statistical error only.

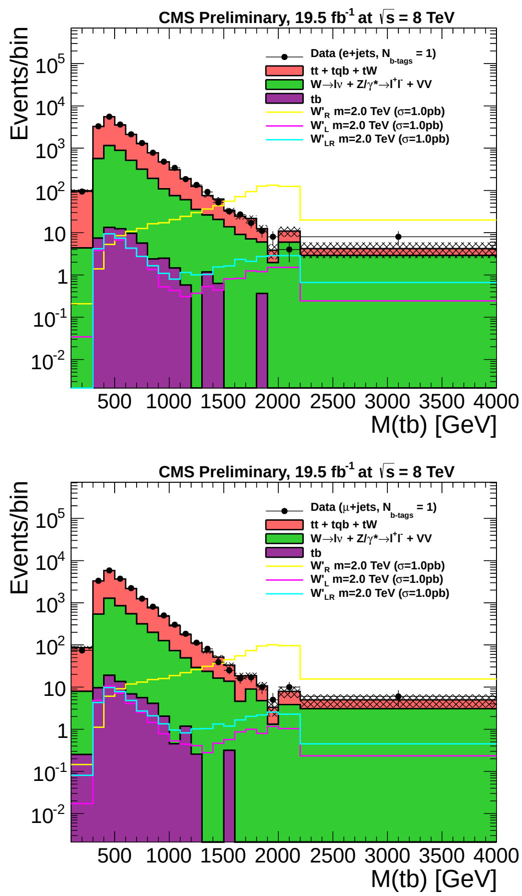

Figure 6.27: The templates used for the limit setting, including Left, Right, and Mixed W′ samples for M(W′)=2.0 TeV. The electron channel is on the top and the muon channel is on the bottom, with the 1 b-tag templates on the left and the 2 b-tag templates on the right. The uncertainty band is the statistical error only.

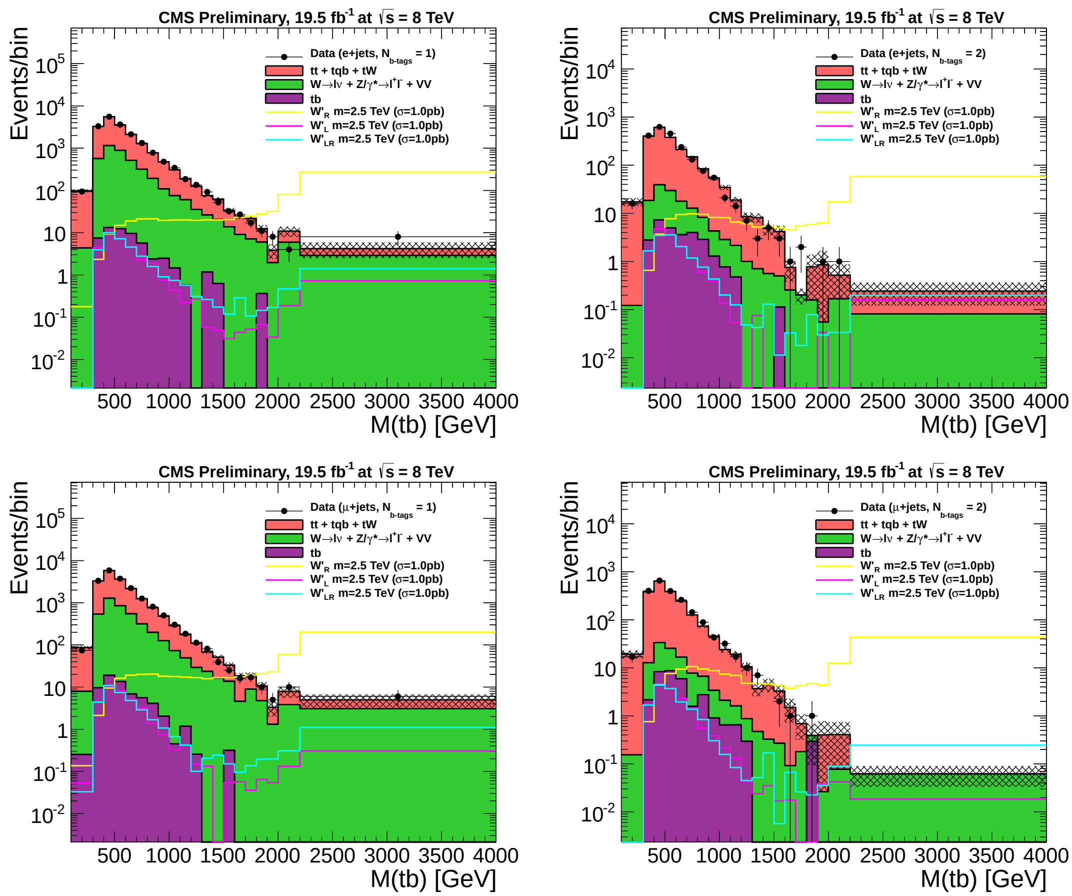

Figure 6.28: The templates used for the limit setting, including Left, Right, and Mixed W′ samples for M(W′)=2.5 TeV. The electron channel is on the top and the muon channel is on the bottom, with the 1 b-tag templates on the left and the 2 b-tag templates on the right. The uncertainty band is the statistical error only.

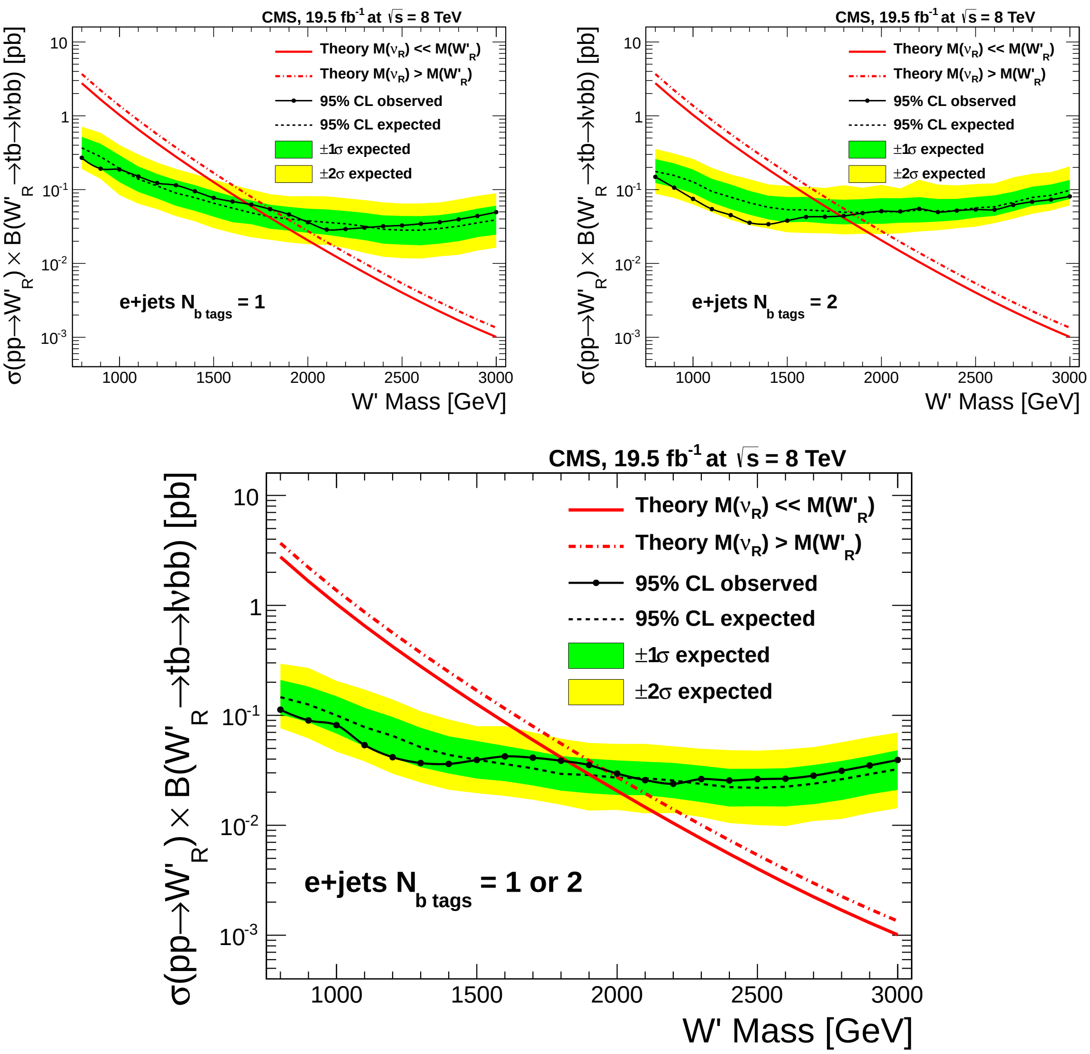

Figure 6.29: Expected and measured Bayesian 95% C.L. upper limits on the production cross-section of right-handed W′ bosons in the electron+jets channel, for the 1 b-tag sample (top left), 2 b-tags sample (top right), and combined 1 or 2 b-tags sample (bottom) for right-handed W′ bosons. W′ masses with a cross-section exceeding the observed limit are excluded.

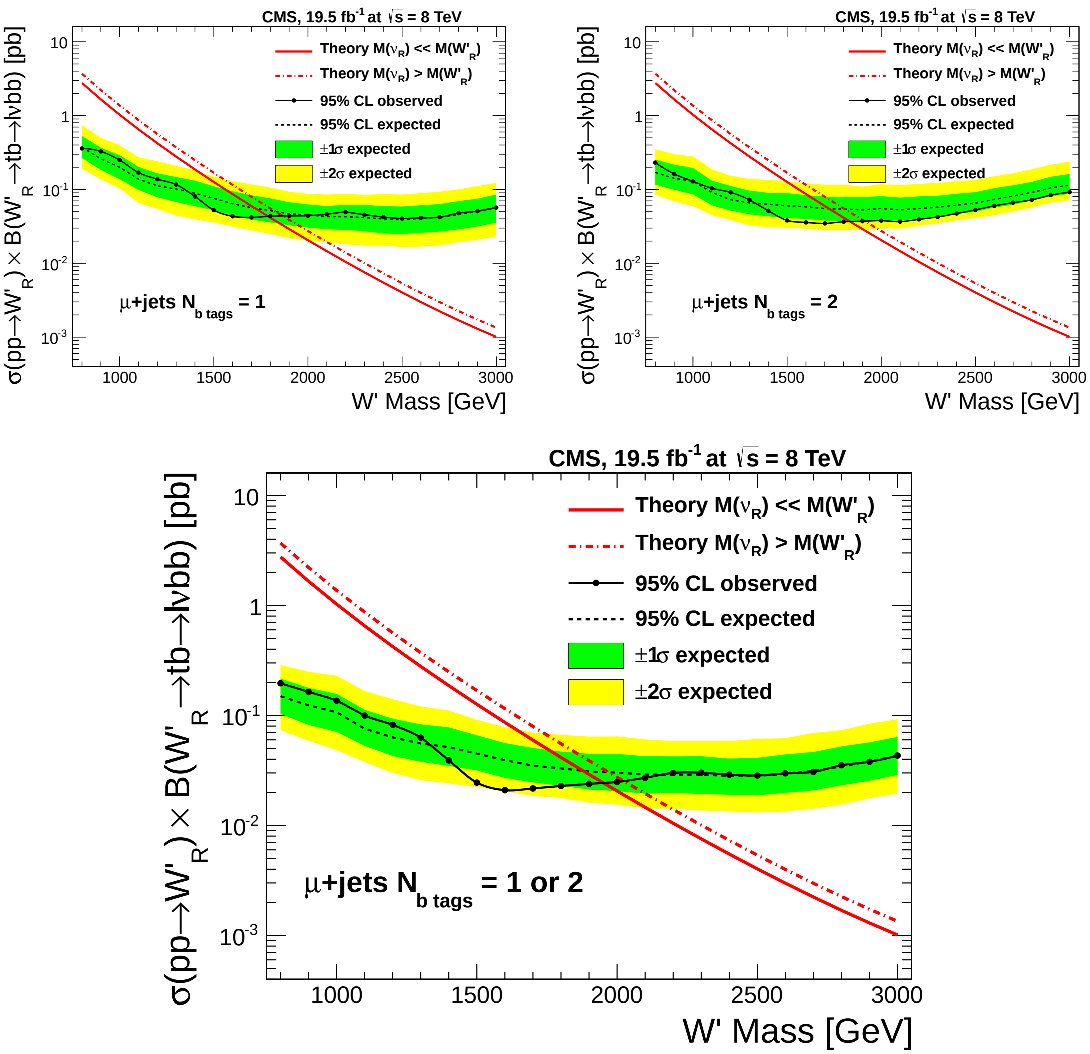

Figure 6.30: Expected and measured Bayesian 95% C.L. upper limits on the production cross-section of right-handed W′ bosons in the muon+jets channel, for the 1 b-tag sample (top left), 2 b-tags sample (top right), and combined 1 or 2 b-tags sample (bottom) for right-handed W′ bosons. W′ masses with a cross-section exceeding the observed limit are excluded.

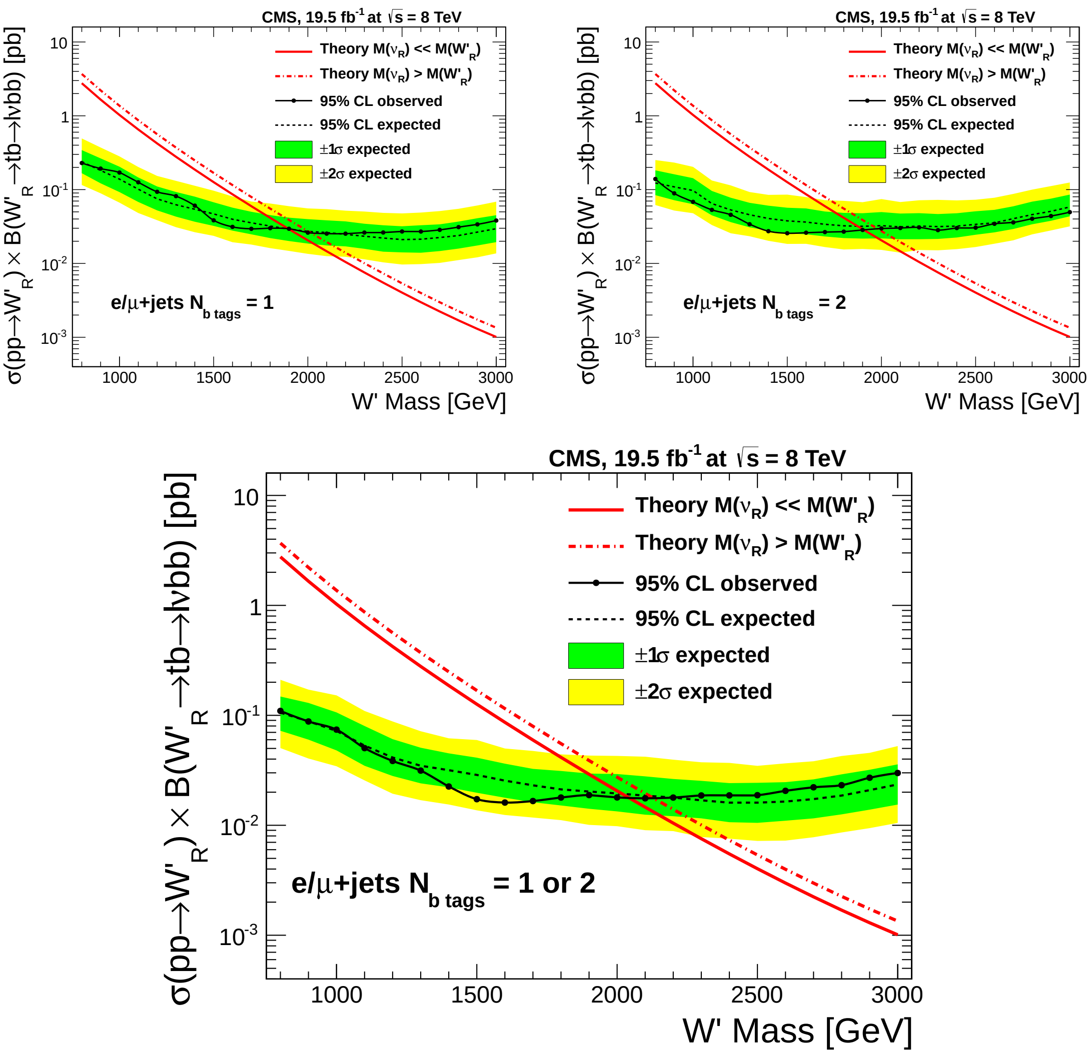

Figure 6.31: Expected and measured Bayesian 95% C.L. upper limits on the production cross-section of right-handed W′ bosons in the combined electron/muon+jets channel, for the 1 b-tag sample (top left), 2 b-tags sample (top right), and combined 1 or 2 b-tags sample (bottom) for right-handed W′ bosons. W′ masses with a cross-section exceeding the observed limit are excluded.

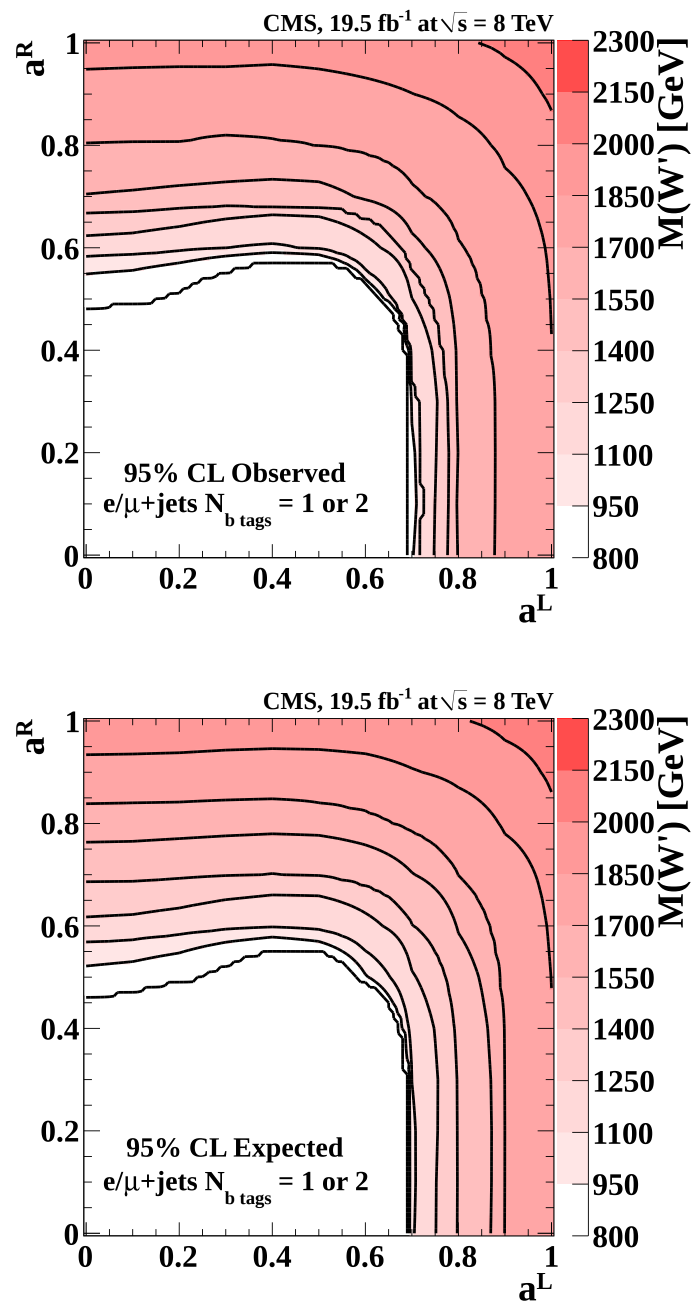

Figure 6.32: Contour plots of M(W′) in the $(a^{\mathrm{L}}, a^{\mathrm{R}})$ plane for which the 95% CL cross section limit equals the predicted cross section for the combined e, μ+jets sample. The left (right) panel represents the observed (expected) limits. The color axis represents the value of M(W′) in GeV. The solid black lines are isocontours of W′-boson mass, plotted in 150 GeV intervals and starting from 800 GeV.

Chapter 7

Conclusions and Outlook

The study of particle physics is a fascinating field of fundamental science that has developed over thousands years. In the last 100 years, the fundamental particles have been discovered and understood using the laws of relativity and quantum mechanics. The final piece of the standard model (SM) of particle physics, which describes accurately the results of every particle physics experiment performed so far, was put in place with the discovery of the Higgs boson at the LHC. This discovery was made possible by complicated particle detectors like the CMS experiment. The CMS experiment was able to efficiently collect data at unprecedented luminosities and was able to reconstruct the decay products of the Higgs boson, a monumental experimental achievement.

However, the SM does not explain naturally why the Higgs boson mass is relatively light compared the Planck scale $M_p = 10^{19}$ GeV, nor does it explain the light neutrino masses and the existence of dark matter. These shortcomings can be addressed by extending the SM to include new symmetries, particles, or even new dimensions of space. Many of these extensions contain a heavy copy of the SM W boson, referred to as a W$'$ boson. These hypothetical particles are searched for in many different decay modes. One important decay mode is W$'$ $\rightarrow$tb, which is a dominant decay mode in many extensions of the SM. A search for this decay was carried out with the CMS experiment, and no evidence for W$'$-boson production was found. Limits on the mass of the W$'$ boson were set, restricting the parameter space of several extensions of the SM.

In 2015 the LHC will begin a second data taking run with a center of mass energy of 13-14 TeV, thereby creating another opportunity to discover W′ bosons. The search strategy will need to be reconsidered to prevent any loss of sensitivity for high mass W′ bosons which could arise when the decay products of the top quark become merged. Furthermore, the search presented in this dissertation can be improved by combining it with the complementary search channel using hadronic decays of the top quark to achieve the best sensitivity. If a discovery takes place, it will signal a new era of particle physics. Theories beyond the SM which predict a W′ boson will reign supreme, and the mass and properties of the W′ boson will be studied to distinguish the between different models. Or perhaps no W′ boson will be found, and only more limits on its mass will be obtained. This scenario would demand many models of new physics to be as unnatural as the SM, and would require them to be critically re-examined.

In the case of no W′ boson discovery during the next LHC data taking run, there is a hope that at least some other form of physics beyond the SM will be discovered. One such possibility is Supersymmetry, which in its minimal form does not contain any W′ bosons. However, Supersymmetry does contain a charged higgs boson H^+ which can decay to a top and bottom quark, just like a W′ boson. The experience gained from the search for W′ bosons in the tb decay channel will prove very valuable for the search for $H^+ \rightarrow$ tb decays.

If anything has been learned from the history of particle physics, it is to never stop looking. Even when it seems like there is nothing more to be discovered, something new could always appear. Wherever there is an unexplored territory, every effort should be made to explore it. This is the way humankind has come to understand nature, and this is the way it will continue until there is nothing left to explore.

Bibliography

[1] A. A. Long, editor. *The Cambridge Companion to Early Greek Philosophy*. Cambridge University Press, 1999.

[2] W. Prout. On the relation between the specific gravities of bodies in their gaseous state and the weights of their atoms. *Annals of Philosophy*, 6:321, 1815.

[3] J. J. Thomson. Cathode Rays. *Philosophical Magazine*, 44:293, 1897.

[4] H. Becquerel. Sur les radiations émises par phosphorescence. *Comptes Rendus*, 122:420, 1896.

[5] M. Planck. Zur Theorie des Gesetzes der Energieverteilung im Normalspektrum. *Verhandlungen der Deutschen Physikalischen Gesellschaft*, 2:237, 1900.

[6] A. Einstein. Über einen die Erzeugung und Verwandlung des Lichtes betreffenden heuristischen Gesichtspunkt. *Annalen der Physik*, 17:132, 1905.

[7] H. Geiger and E. Marsden. On a Diffuse Reflection of the α-Particles". *Proceedings of the Royal Society, Series A*, 82:495, 1909.

[8] E. Rutherford. The Scattering of α and β Particles by Matter and the Structure of the Atom. *Philosophical Magazine, Series 6*, 21, 1911.

[9] N. Bohr. The spectra of helium and hydrogen. *Nature*, 92:231, 1913.

[10] P. A. M. Dirac. Quantised singularities in the quantum field. *Proceedings of the Royal Society of London A*, 133:60, 1931.

[11] C. D. Anderson. The positive electron. *Physical Review*, 43:491, 1933.

[12] E. Fermi. Versuch einer Theorie der β-Strahlen. I. *Zeitschrift für Physik*, 88:161, 1934.

[13] C. Anderson and S. Neddermeyer. Cloud Chamber Observations of Cosmic Rays at 4300 Meters Elevation and Near Sea-Level. *Physical Review*, 50:263, 1936.

[14] M. Conversi et. al. On the Disentegration of Negative Mesons. *Physical Review*, 71:209, 1947.

[15] C. F. Powell et. al. Processes Involving Charged Mesons. *Nature*, 159:694, 1947.

[16] G. D. Rochester and C.C. Butler. Evidence for the Existence of New Unstable Elementary Particles". *Nature*, 160, 1947.

[17] V. D. Hopper and S. Biswas. Evidence Concerning the Existence of the New Unstable Elementary Neutral Particle. *Physical Review*, 80:1099, 1950.

[18] G. L. Cowan et. al. Detection of the Free Neutrino: a Confirmation. *Science*, 124:103, 1956.

[19] Brookhaven National Laboratory. Our history: Accelerators. `http://www.bnl.gov/about/history/accelerators.php`. Accessed: 2014-01-15.

[20] M. Gell-Mann. A schematic model of baryons and mesons. *Physics Letters*, 8:214, 1964.

[21] V. E. Barnes et. al. Observation of a Hyperon with Strangeness Minus Three. *Physical Review Letters*, 12:204, 1964.

[22] M. Breidenbach et. al. Observed Behavior of Highly Inelastic Electron-Proton Scattering. *Physical Review Letters*, 23:935, 1969.

[23] G. Danby et. al. Observation of High-Energy Neutrino Reactions and the Existence of Two Kinds of Neutrinos. *Physical Review Letters*, 9:36, 1962.

[24] J. J. Aubert et. al. Experimental Observation of a Heavy Particle J. *Physical Review Letters*, 33:1404, 1974.

[25] J.-E. Augustin et. al. Discovery of a Narrow Resonance in e^+e^- Annihilation. *Physical Review Letters*, 33:1406, 1974.

[26] S. L. Glashow et. al. Weak interactions with lepton-hadron symmetry. *Physical Review D*, 2:1285, 1970.

[27] M. L. Perl et. al. Evidence for Anomalous Lepton Production in e^+e^- Annihilation. *Physical Review Letters*, 35:1489, 1975.

[28] DONUT Collaboration. Observation of tau neutrino interactions. *Physics Letters B*, 504:218, 2001.

[29] S. W. Herb et. al. Observation of a Dimuon Resonance at 9.5 GeV in 400-GeV Proton-Nucleus collisions. *Physical Review Letters*, 39:252, 1977.

[30] PLUTO Collaboration. Jet analysis of the $\Upsilon(9.46)$ decay into charged hadrons. *Physics Letters B*, 82:449, 1979.

[31] UA1 Collaboration. Experimental observation of isolated large transverse energy electrons with associated missing energy at $\sqrt{s} = 540$ GeV. *Physics Letters B*, 122:103, 1983.

[32] UA1 Collaboration. Experimental observation of lepton pairs of invariant mass around 95 GeV/c^2 at the CERN SPS collider. *Physics Letters B*, 126:398, 1983.

[33] CDF Collaboration. Observation of Top Quark Production in $\bar{p}p$ Collisions with the Collider Detector at Fermilab. *Physical Review Letters*, 74:2626, 1995.

[34] D0 Collaboration. Observation of the top quark. *Physical Review Letters*, 74:2632, 1995.

[35] CMS Collaboration. Observation of a new boson at a mass of 125 GeV with the CMS experiment at the LHC. *Physics Letters B*, 716:30, 2012.

[36] ATLAS Collaboration. Observation of a new particle in the search for the Standard Model Higgs boson with the ATLAS detector at the LHC. *Physics Letters B*, 716:1, 2012.

[37] Particle physics - Wikipedia. `http://en.wikipedia.org/wiki/Particle_physics`. Accessed: 2013-02-18.

[38] V. C. Rubin et. al. Rotational properties of 21 SC galaxies with a large range of luminosities and radii, from NGC 4605 ($R = 4$ kpc) to UGC 2885 ($R = 122$ kpc). *The Astrophysical Journal*, 238:471, 1980.

[39] R. Massey et. al. The dark matter of gravitational lensing. *Reports on Progress in Physics*, 73:086901, 2010.

[40] Planck Collaboration. Planck 2013 results. I. Overview of products and scientific results. `arXiv:astro-ph/1303.5062`, 2013.

[41] C. J. Copi et. al. Big-bang nucleosynthesis and the baryon density of the universe. *Science*, 267:192, 1995.

[42] R. Davis et. al. Search for Neutrinos from the Sun. *Physical Review Letters*, 20:1205, 1968.

[43] Super-Kamiokande Collaboration. Evidence for Oscillation of Atmospheric Neutrinos. *Physical Review Letters*, 81:1562, 1998.

[44] SNO Collaboration. Measurement of the Rate of $\nu_e + d \rightarrow p + p + e^-$ Interactions Produced by ^{8}B Solar Neutrinos at the Sudbury Neutrino Observatory. *Physical Review Letters*, 87:071301, 2001.

[45] J. Beringer et al. (Particle Data Group). Review of Particle Physics. *Physical Review D*, 86:010001, 2012.

[46] Planck Collaboration. Planck 2013 results. XVI. Cosmological parameters. `arXiv:astro-ph/1303.5076`, 2013.

[47] M. Trodden. Electroweak baryogenesis. *Reviews of Modern Physics*, 71:1463, 1999.

[48] A. Sakharov. Violation of CP invariance, C asymmetry, and baryon asymmetry of the universe. *Soviet Physics Uspekhi*, 34:392, 1991.

[49] H. Georgi and S. Glashow. Unity of All Elementary-Particle forces. *Physical Review Letters*, 32:438, 1974.

[50] A. Buras et. al. Aspects of the grand unification of strong, weak and electromagnetic interactions. *Nuclear Physics B*, 135:66, 1978.

[51] C. Quigg. *Flavor Physics for the Millennium: TASI 2000*, chapter The Electroweak Theory. World Scientific, 2000.

[52] M. Gaillard et. al. The standard model of particle physics. *Reviews of Modern Physics*, 71:S96, 1999.

[53] A. Djouadi. The anatomy of electroweak symmetry breaking: Tome I: The Higgs boson in the Standard Model. *Physics Reports*, 457:1, 2008.

[54] G. Altarelli. The Standard Electroweak Theory and Beyond. `arxiv:hep-ph/9811456`, 1998.

[55] A. Pinch. The Standard Model of Electroweak Interactions. `arxiv:hep-ph/0705.4264`, 2007.

[56] F. Halzen and A. Martin. *Quarks and Leptons*. Wiley, 1984.

[57] S. L. Glashow. Partial-symmetries of weak interactions. *Nuclear Physics*, 22:579, 1961.

[58] T. D. Lee and C. N. Yang. Question of Parity Conservation in Weak Interactions. *Physical Review*, 104:254, 1956.

[59] C. S. Wu et. al. Experimental Test of Parity Conservation in Beta Decay. *Physical Review*, 105:1413, 1957.

[60] H. Georgi. *Lie Algebras in PArticle Physics*. Westview Press, 1999.

[61] P. W. Higgs. Broken Symmetries and the Masses of Gauge Bosons. *Physical Review Letters*, 13:508, 1964.

[62] P. W. Higgs. Spontaneous Symmetry Breakdown without Massless Bosons. *Physical Review*, 145:1156, 1966.

[63] F. Englert and R. Brout. Broken Symmetry and the Mass of Gauge Vector Mesons. *Physical Review Letters*, 13:321, 1964.

[64] G. S. Guralnik et. al. Global Conservation Laws and Massless Particles. *Physical Review Letters*, 13:585, 1965.

[65] F. Hasert et. al. Observation of Neutrino-Like Interactions Without Muon or Electron in the Gargamelle Neutrino Experiment. *Physics Letters B*, 46:138, 1973.

[66] The ALEPH, DELPHI, L3, OPAL, SLD Collaborations, the LEP Electroweak Working Group, the SLD Electroweak, and Heavy Flavour Groups. Precision Electroweak Measurements on the Z Resonance. *Physics Reports*, 427:257, 2006.

[67] The ALEPH, DELPHI, L3, OPAL Collaborations, and the LEP Electroweak Working Group. Electroweak Measurements in Electron-Positron Collisions at W-Boson-Pair Energies at LEP. *Physics Reports*, 532:119, 2013.

[68] D. Buttazzo et. al. Investigating the near-criticality of the Higgs boson. `arxiv:hep-ph/1307.3536`, 2013.

[69] M. Schmaltz and D. Tucker-Smith. Little Higgs Theories. *Annual Review of Nuclear and Particle Science*, 55:229, 2005.

[70] S. Martin. A Supersymmetry Primer. `arxiv:hep-ph/9709356v6`, 2011.

[71] S. Dimopoulos and H. Georgi. Softly broken supersymmetry and SU(5). *Nuclear Physics B*, 193:150, 1981.

[72] CMS Collaboration. CMS Supersymmetry Physics Results. `https://twiki.cern.ch/twiki/bin/view/CMSPublic/PhysicsResultsSUS`. Accessed 01-28-2014.

[73] N. Arkani-Hamed et. al. The hierarchy problem and new dimensions at a millimeter. *Physics Letters B*, 429:263, 1998.

[74] L. Randall and R. Sundrum. Large Mass Hierarchy from a Small Extra Dimension. *Physical Review Letters*, 83:3370, 1999.

[75] A. Pomarol. Gauge bosons in a five-dimensional theory with localized gravity. *Physics Letters B*, 486:153, 2000.

[76] N. Arkani-Hamed et. al. Electroweak symmetry breaking from dimensional deconstruction. *Physics Letters B*, 513:232, 2001.

[77] T. Han et. al. Smoking-gun signatures of little Higgs models. *Journal of High Energy Physics*, 01:99, 2009.

[78] The LEP Collaborations: ALEPH Collaboration, DELPHI Collaboration, L3 Collaboration, OPAL Collaboration, the LEP Electroweak Working Group, the SLD Electroweak, and Heavy Flavour Groups. A Combination of Preliminary Electroweak Measurements and Constraints on the Standard Model. `arxiv:hep-ex/0312023`, 2004.

[79] N. Arkani-Hamed et. al. The Littlest Higgs. *Journal of High Energy Physics*, 07:034, 2002.

[80] M. Schmaltz. The simplest little Higgs. *Journal of High Energy Physics*, 08:056, 2004.

[81] J. C. Pati and A. Salam. Lepton number as the fourth "color". *Physical Review D*, 10:275, 1974.

[82] R. N. Mohapatra and J. C. Pati. “natural” left-right symmetry. *Physical Review D*, 11:2558, 1975.

[83] G. Senjanovic and R. N. Mohapatra. Exact left-right symmetry and spontaneous violation of parity. *Physical Review D*, 12:1502, 1975.

[84] G. Senjanovic. Spontaneous breakdown of parity in a class of gauge theories. *Nuclear Physics B*, 153:334, 1979.

[85] R. N. Mohapatra and G. Senjanovic. Neutrino Mass and Spontaneous Parity Nonconservation. *Physical Review Letters*, 44:912, 1980.

[86] A. Maiezza et. al. Left-Right Symmetry at LHC. `arxiv:hep-ph/1005.5160`, 2010.

[87] C. Csaki et. al. Big corrections from a little Higgs. *Physical Review D*, 67:115002, 2003.

[88] CMS Collaboration. Search for new physics in final states with a lepton and missing transverse energy in pp collisions at the LHC. *Physical Review D*, 87:072005, 2013.

[89] ATLAS Collaboration. ATLAS search for a heavy gauge boson decaying to a charged lepton and a neutrino in pp collisions at $\sqrt{s} = 7$ TeV. *The European Physical Journal C*, 72:2241, 2012.

[90] CMS Collaboration. Search for narrow resonances using the dijet mass spectrum in pp collisions at $\sqrt{s} = 8$ TeV. *Physical Review D*, 87:114015, 2013.

[91] ATLAS Collaboration. ATLAS search for new phenomena in dijet mass and angular distributions using pp collisions at $\sqrt{s} = 7$ TeV. *Journal of High Energy Physics*, 01, 2013.

[92] CMS Collaboration. Search for Heavy Neutrinos and W_R Bosons with Right-Handed Couplings in a Left-Right Symmetric Model in pp Collisions at $\sqrt{s} = 7$ TeV. *Physical Review Letters*, 109:261802, 2012.

[93] ATLAS Collaboration. Search for heavy neutrinos and right-handed W bosons in events with two leptons and jets in pp collisions at $\sqrt{s} = 7$ TeV with the ATLAS detector. *The European Physical Journal C*, 72:2056, 2012.

[94] L. Evans and P. Bryant. LHC Machine. *Journal of Instrumentation*, 3:S08001, 2008.

[95] S. Myers and E. Picasso. The design, construction and commissioning of the CERN Large Electron–Positron collider. *Contemporary Physics*, 31:387, 1990.

[96] M. Benedikt et. al. *LHC Design Report - The LHC Injector Chain*, volume 3. CERN, 2004.

[97] The CERN Accelerator Complex. `http://te-epc-lpc.web.cern.ch/te-epc-lpc/machines/pagesources/Cern-Accelerator-Complex.jpg`. Accessed: 2013-12-27.

[98] Document EDMS 973073. *Interim Summary Report on the Analysis of the 19 September 2008 Incident at LHC*. CERN, 2008.

[99] G. Arduini et. al. Electron cloud and scrubbing in the LHC. LHC Operation Meeting, Evian, December 2012.

[100] CMS Luminosity - Public Results. `https://twiki.cern.ch/twiki/bin/view/CMSPublic/LumiPublicResults`. Accessed: 2014-02-18.

[101] M. Kuhn. LHC Beam Operations Past, Present and Future. Moriond QCD, La Thuile, Italy, March 2013.

[102] CMS Collaboration. The CMS Experiment at the CERN LHC. *Journal of Instrumentation*, 3:S08004, 2008.

[103] CMS detector design. `http://cms.web.cern.ch/news/cms-detector-design`. Accessed: 2013-12-27.

[104] CMS Collaboration. Tracking and Primary Vertex Results in First 7 TeV Collisions. CMS-PAS-TRK-10-005, 2010.

[105] CMS Collaboration. Performance and operation of the CMS electromagnetic calorimeter. *Journal of Instrumentation*, 5:T03010, 2010.

[106] CMS 2013 Public Electron Performance Results. `https://twiki.cern.ch/twiki/bin/view/CMSPublic/EGMElectronsMoriond2013`. Accessed: 2013-12-31.

[107] CMS Collaboration. Status of the 8 TeV Jet Energy Corrections and Uncertainties based on 11 fb^{-1} of data in CMS. CMS-DP-2013-11, 2013.

[108] CMS Collaboration. Performance of Missing Transverse Momentum Reconstruction Algorithms in Proton–Proton Collisions at $\sqrt{s} = 8$ TeV with the CMS Detector. CMS-PAS-JME-12-002, 2013.

[109] CMS Muon Results. `https://twiki.cern.ch/twiki/bin/view/CMSPublic/PhysicsResultsMUO`. Accessed: 2014-01-01.

[110] CMS Collaboration. CMS TriDAS project : Technical Design Report, Volume 1: The Trigger Systems. CERN-LHCC-2000-038, 2000.

[111] CMS Collaboration. CMS TriDAS project : Technical Design Report, Volume 2: Data Acquisition and High-Level Trigger. CERN-LHCC-2002-026, 2002.

[112] J. Brooke. Performance of the CMS Level-1 Trigger. 36th International Conference on High Energy Physics, Melbourne, Australia, 2012.

[113] CMS Collaboration. The CMS high level trigger. *The European Physical Journal C*, 46:605, 2006.

[114] G. Bauer et. al. Recent experience and future evolution of the CMS High Level Trigger System. Real Time Conference (RT), 18th 2012 IEEE-NPSS, Berkeley, California, U.S.A.

[115] Z. Demiragli. High Level Trigger development with OpenHLT. Posters@LHCC, Geneva, Switzerland, 2013.

[116] CMS Collaboration. Inclusive Search for Supersymmetry Using Razor Variables in *pp* Collisions at $\sqrt{s} = 7$ TeV. *Physical Review Letters*, 111:081802, 2013.

[117] CMS Collaboration. Search for Supersymmetry at the LHC in Events with Jets and Missing Transverse Energy. *Physical Review Letters*, 107:221804, 2011.

[118] Trigger Approved Results. `https://twiki.cern.ch/twiki/bin/view/CMSPublic/L1TriggerDPGResults`. Accessed: 2014-01-08.

[119] CMS Collaboration. Observation of long-range, near-side angular correlations in proton-proton collisions at the LHC. *Journal of High Energy Physics*, 9:091, 2010.

[120] S. Beauceron. The CMS High Level Trigger. 36th International Conference on High Energy Physics, Melbourne, Australia, 2012.

[121] G. Bauer et. al. CMS DAQ Event Builder Based on Gigabit Ethernet. *IEEE Transactions on Nuclear Science*, 55:198, 2008.

[122] N.J. Boden et al. Myrinet - A Gigabit per Second Local Area Network. *IEEE-Micro*, 15:29, 1995.

[123] T. Appelquist et. al. Bounds on universal extra dimensions. *Physical Review D*, 64:035002, 2001.

[124] H. C. Cheng et. al. Standard model in the latticized bulk. *Physical Review D*, 64:065007, 2001.

[125] R. S. Chivukula et. al. Limits on noncommuting extended technicolor. *Physical Review D*, 53:5258, 1996.

[126] R. N. Mohapatra J. C. Pati. Left-right gauge symmetry and an 'isoconjugate' model of CP violation. *Physical Review D*, 11:566, 1975.

[127] CMS Collaboration. Search for leptonic decays of W$'$ bosons in pp collisions at $\sqrt{s} = 7$ TeV. *Journal of High Energy Physics*, 8:023, 2012.

[128] CMS Collaboration. Search for heavy resonances in the W/Z-tagged dijet mass spectrum in pp collisions at 7 TeV. *Physics Letters B*, 723:280, 2013.

[129] CMS Collaboration. Search for exotic resonances decaying into WZ/ZZ in pp collisions at $\sqrt{s} = 7$ TeV. *Journal of High Energy Physics*, 2, 2013.

[130] CMS Collaboration. Search for a W$'$ or Techni-ρ Decaying into WZ in pp Collisions at $\sqrt{s} = 7$ TeV. *Physical Review Letters*, 109:141801, 2012.

[131] ATLAS Collaboration. Search for resonant diboson production in the WW/WZ$\rightarrow$ $\ell\nu jj$ decay channels with the ATLAS detector at $\sqrt{s} = 7$ TeV. *Physical Review D*, 87:112006, 2013.

[132] ATLAS Collaboration. Search for resonant WZ production in the WZ$\rightarrow$ $\ell\nu\ell'\ell'$ channel in $\sqrt{s} = 7$ TeV pp collisions with the ATLAS detector. *Physical Review D*, 85:112012, 2012.

[133] M. Nemevsek et. al. Limits on the left-right symmetry scale and heavy neutrinos from early LHC data. *Physical Review D*, 83:115014, 2011.

[134] D. Muller and S. Nandi. Topflavor: a separate SU(2) for the third family. *Physics Letters B*, 383:345, 1996.

[135] E. Malkawi et. al. A model of strong flavor dynamics for the top quark. *Physics Letters B*, 385:304, 1996.

[136] CDF Collaboration. Search for the Production of Narrow tb Resonances in 1.9 fb^{-1} of ppbar Collisions at sqrt(s) = 1.96 TeV. *Physical Review Letters*, 103:041801, 2009.

[137] D0 Collaboration. Search for W$'$ Boson Resonances Decaying to a Top Quark and a Bottom Quark. *Physical Review Letters*, 100:211803, 2008.

[138] D0 Collaboration. Search for W$'$ resonances with left- and right-handed couplings to fermions. *Physics Letters B*, 699:145, 2011.

[139] CMS Collaboration. Search for a W′ boson decaying to a bottom quark and a top quark in *pp* collisions at $\sqrt{s} = 7$ TeV. *Physics Letters B*, 718:1229, 2013.

[140] ATLAS Collaboration. Search for tb resonances in proton-proton collisions at $\sqrt{s} = 7$ TeV with the ATLAS detector. *Physical Review Letters*, 109:081801, 2012.

[141] Y. Freund and R.E. Schapire. A Decision-Theoretic Generalization of On-Line Learning and an Application to Boosting. *Journal of Computer and System Sciences*, 55:119, 1997.

[142] E. E. Boos et. al. Interference between W' and W in single-top quark production processes. *Physics Letters B*, 655:245, 2007.

[143] E. E. Boos et. al. Method for simulating electroweak top-quark production events in the NLO approximation: SingleTop event generator. *Physics of Atomic Nuclei*, 69:1317, 2006.

[144] E. Boos et. al. CompHEP 4.4: Automatic computations from Lagrangians to events. *Nuclear Instruments and Methods in Physics Research Section A*, 534:250, 2004.

[145] Z. Sullivan. Fully differential W′ production and decay at next-to-leading order in QCD. *Physical Review D*, 66:075011, 2002.

[146] D. Duffty and Z. Sullivan. Model independent reach for W-prime bosons at the LHC. *Physical Review D*, 86:075018, 2012.

[147] J. Pumplin et. al. New generation of parton distributions with uncertainties from global QCD analysis. *Journal of High Energy Physics*, 07:012, 2002.

[148] J. Alwall et. al. MadGraph 5: Going beyond. *Journal of High Energy Physics*, 06:128, 2011.

[149] M. Czakon et. al. The total top quark pair production cross-section at hadron colliders through O(α_s^4). *Physical Review Letters*, 110:252004, 2013.

[150] S. Frixione et. al. Matching NLO QCD computations with Parton Shower simulations: the POWHEG method. *Journal of High Energy Physics*, 11:070, 2007.

[151] N. Kidonakis. NNLL threshold resummation for top-pair and single-top production. `arxiv:hep-ph/1210.7813`, 2012.

[152] T. Sjöstrand et. al. PYTHIA 6.4 Physics and Manual. *Journal of High Energy Physics*, 05:026, 2006.

[153] CMS Collaboration. Measurement of the underlying event activity at the LHC with $\sqrt{s} = 7$ tev and comparison with $\sqrt{s} = 0.9$ TeV. *Journal of High Energy Physics*, 09:109, 2011.

[154] GEANT Collaboration. GEANT4—a simulation toolkit. *Nuclear Instruments and Methods in Physics Research Section A*, 506:250, 2003.

[155] CMS Collaboration. Particle–Flow Event Reconstruction in CMS and Performance for Jets, Taus, and $\mathrm{E}_{\mathrm{T}}^{\mathrm{miss}}$. CMS Physics Analysis Summary CMS-PAS-PFT-09-001, CERN, 2009.

[156] CMS Collaboration. Commissioning of the Particle-flow Event Reconstruction with the first LHC collisions recorded in the CMS detector. CMS Physics Analysis Summary CMS-PAS-PFT-10-001, CERN, 2010.

[157] W. Adam et. al. Reconstruction of Electrons with the Gaussian-Sum Filter in the CMS Tracker at the LHC. *Journal of Physics G: Nuclear and Particle Physics.*

[158] CMS Collaboration. Search for neutral Higgs bosons decaying to tau pairs in pp collisions at $\sqrt{s} = 7$ TeV. *Physics Letters B*, 713(2):68, 2012.

[159] M. Cacciari et. al. The Anti-k(t) jet clustering algorithm. *Journal of High Energy Physics*, 04:063, 2008.

[160] CMS Collaboration. Determination of jet energy calibration and transverse momentum resolution in cms. *Journal of Instrumentation*, 6:P11002, 2011.

[161] CMS Collaboration. Identification of b-quark jets with the CMS experiment. *Journal of Instrumentation*, 8:P04013, 2013.

[162] CMS Collaboration. Measurement of the $t\bar{t}$ production cross section in pp collisions at 7 TeV in lepton + jets events using b-quark jet identification. *Physical Review D*, 84:092004, 2011.

[163] J. Alwall et. al. MadGraph/MadEvent v4: The New Web Generation. *Journal of High Energy Physics*, 09:028, 2007.

[164] CMS Collaboration. Measurement of differential top-quark pair production cross sections in the lepton+jets channel in pp collisions at 8 TeV. CMS Physics Analysis Summary CMS-PAS-TOP-12-027, CERN, 2013.

[165] CMS Collaboration. Measurement of the differential ttbar cross section in the dilepton channel at 8 TeV. CMS Physics Analysis Summary CMS-PAS-TOP-12-028, CERN, 2013.

[166] J. Alwall et.al. Comparative study of various algorithms for the merging of parton showers and matrix elements in hadronic collisions. *The European Physical Journal C*, 53:473, 2008.

[167] T. Müller et. al. theta - a framework for template-based modeling and inference. `http://www-ekp.physik.uni-karlsruhe.de/~ott/theta/testing/html/theta__auto__intro.html`, 2010.

Curriculum Vitae

David M. Sperka

Contact Information

Permanent Address:	Current Address:	dsperka@bu.edu
2825 S 114 St	253 Cambridge St. Apt. #3	dsperka@cern.ch
West Allis, WI 53227 U.S.A.	Allston, MA 02134 U.S.A.	Phone: +1 (414) 704-1174

Education

- 05/2009, B.S. University of Wisconsin Madison

  Physics, Mathematics, Astronomy-Physics

  Senior Thesis: "The Search for $B_{s(d)} \to \mu^+\mu^-$ With 3.7 fb^{-1} of $p\bar{p}$ Collisions"

  Supervisor: Prof. Matt Herndon

- 05/2014, Ph.D. Boston University

  Experimental High Energy Physics

  Thesis: "Search for a heavy resonance decaying to a top quark and a bottom quark with the CMS experiment"

  Supervisor: Prof. Tulika Bose

Research Activities

Search for new physics in the tb final state Played an integral role in the analysis of the e+jets channel, as well the statistical combination with the μ+jets channel and the development of a multivariate analysis using 5.0 fb^{-1} of pp collisions at $\sqrt{s} = 7$ TeV. Led the full analysis effort of both channels using 19.5 fb^{-1} at $\sqrt{s} = 8$ TeV, including event selection, sensitivity optimization, uncertainty estimation and statistical interpretation. Helped initiate the effort to extend the search to cover a wider range of new physics models, specifically a search for a charged Higgs boson decaying to tb.

B2G Trigger Contact Served as trigger contact person for the CMS Beyond Two Generations (B2G) Physics Analysis Group, which focuses on new physics searches with top quarks in the final state, since 2012. Responsible for developing the trigger strategy for the $\sqrt{s} = 13$ TeV LHC run. Reviewed the treatment of the trigger by all analyses within the group, and collaborated with other authors to develop strategies for measuring the trigger efficiencies of challenging boosted signal topologies (e.g. $\mathrm{Z}' \to \mathrm{t\bar{t}} \to e + \mathrm{jets}$)

Tracker Muon Triggers Implemented a complementary muon reconstruction algorithm ("Tracker Muon") in the CMS High Level Trigger (HLT) within the first few months of data taking in 2010. This algorithm is more efficient for low momentum muons than the standard muon reconstruction. This type of trigger is now widely used in many Higgs, Top, and Exotica analyses within CMS.

Muon Trigger Efficiency Measured the efficiency of the CMS muon trigger at large transverse momentum using the first LHC data. The measurement was used in the search for $\mathrm{W}' \to \mu\nu$ using 36 pb^{-1} at $\sqrt{s} = 7$ TeV. The method used jet triggered data to extend the kinematic range, and was complementary to other techniques helping to determine the systematic uncertainty.

HLT CPU Performance Was responsible during the first LHC run (2010-2012) for the monitoring of the CPU performance of the CMS HLT. Included optimizing CPU intensive algorithms as well as extrapolating the necessary CPU capacity from lower to higher instantaneous luminosities.

HLT On Call Expert Served as a 24/7 on-call expert for the CMS HLT from 2011-2012. Included monitoring the data quality of the CMS detector, as well as designing special data taking configurations.

Selected Publications And Conference Notes

1. The CDF Collaboration. "The Search for $B_{s(d)} \to \mu^+\mu^-$ With 3.7 fb^{-1} of $p\bar{p}$ Collisions", CDF Public Note 9892

2. The CMS Collaboration. "Search for a W$'$ boson decaying to a muon and a neutrino in pp collisions at $\sqrt{s} = 7$ TeV", Phys. Lett. B **701** 160 (2011), `arXiv:1103.0030`

3. The CDF Collaboration, "The Search for $B_{s(d)} \to \mu^+\mu^-$ With 7 fb^{-1} of $p\bar{p}$ Collisions", Phys. Rev. Lett. **107** 191801 (2011), `arXiv:1107.2304`

4. The CMS Collaboration. "Performance of CMS muon reconstruction in pp collisions at $\sqrt{s} = 7$ TeV", JINST **7** (2012) P10002. `arXiv:1206.4071`

5. The CMS Collaboration. "Search for a W$'$ boson decaying to a bottom quark and a top quark in pp collisions at $\sqrt{s} = 7$ TeV", Phys. Lett. B **718** (2013) 122, `arXiv:1208.0956`

6. The CMS Collaboration. "Search for W$'$ to tb decays in the lepton + jets final state in pp collisions at $\sqrt{s} = 8$ TeV", To be published in JHEP, `arXiv:1402.2176`

Talks and Posters

- 02/2013, “Search for tb resonances with the CMS experiment”, La Thuile 2013
- 03/2013, “The search for tb resonances with the CMS experiment”, LHCC Student Poster Session
- 11/2013, “Search for W′ bosons that decay to top+bottom”, USLUO 2013

Teaching

- Fall 2010, Physics 241 “Physics for Life Science Majors”, Discussion and Lab sections
- Spring 2011, Physics 211 “Physics for Engineers”, Discussion and Lab sections

Outreach

- 02/2007, “The Wonders of Physics”, Lecture and Demonstrations, University of Wisconsin
- 05/2010, “Particles and Collisions”, Interactive Lecture, LERNet Physics Day at Boston University

Awards

- 04/2008, Dr. Maritza Irene Stapanian Crabtree Undergraduate Scholarship
- 09/2009, Boston University Dean’s Fellowship
- 04/2011, Outstanding Performance by a First Year B.U. Physics Graduate Student
- 12/2011, CMS Students and Post-Docs Achievement Award